Kinematics and star formation histories of brightest cluster galaxies

SA Nkosi

orcid.org/0000-0003-0549-468X

Dissertation accepted in partial fulfilment of the requirements for the degree *Master of Science in Astrophysical Sciences* at the North-West University

Supervisor: Prof SI Loubser

Graduation May 2023

27201732

Acknowledgements

First and foremost, the very most important acknowledgment goes to my MSc supervisor, Prof. Ilani Loubser, for her tremendous guidance and amazing support over the past three years. She was very patient with me and all my questions and inspired me throughout our discussions. I would also like to thank her for taking time to read the many drafts I wrote, this truly made me improve as an academic writer. I also feel very fortunate to have benefited from her vast wealth of experience and knowledge.

My appreciation also goes to people in the Centre for Space Research (CSR) as a whole for making the department an enjoyable and a friendly place for both daily life and academic research. In particular, the staff for administrative support and handling our finances. I also thank the people I've shared my office space with over the years for making it an amazing environment to work.

And to all the friends I've made along the way here at the NWU. Thank you for sharing this journey with me and creating with me memories that I will forever cherish. And for that, Baraka Allahu Fik'.

I gratefully acknowledge the National Astrophysics and Space Science Program (NASSP) for financially supporting my MSc study for the first two years. I also wish to thank the CSR for supporting my final-year studies.

Abstract

Brightest cluster galaxies (BCGs) are the most massive and luminous galaxies in the Universe. In this work we study BCGs at intermediate redshifts ($0.3 < z < 0.8$) to provide more observational insights on the BCG formation and evolution over a 3.4 billion years period, by analysing their stellar kinematic properties and stellar populations with respect to redshift. Studying BCG properties with redshift is important in order to understand their formation and evolutionary histories, as the details are not yet clear. In this work, we study Brightest cluster galaxies Evolution with AdvACT, MeerKAT and SALT (BEAMS) BCGs that are observed with the Southern African Large Telescope (SALT) using the RSS longslit spectrograph. We identify the BCGs from the long-slit data from visual inspection using finder charts and Dark Energy Survey (DES) imaging. We stack the BCG sample with respect to redshift in order to improve the signal-to-noise (S/N) of our sample to derive their kinematics and stellar population parameters. We use the full-spectrum fitting software, pPXF to derive the kinematics of the sample. We also derive their stellar populations with FIREFLY. We investigate the age-redshift relation of the BEAMS BCGs in order to study their evolution. The age-redshift relation of these BCGs is also compared to a sample of 16 Luminous Red Galaxies (LRGs). In this comparison we find that BCGs tend to have much older ages. If we assume that BCGs are passively evolving systems, their ages can, potentially, be used to constrain the expansion of the Universe. If the luminosity–weighted Single Stellar Population (SSP) equivalent ages represents the ages of the galaxies, these estimated ages can be used to calculate the Hubble parameter $H(z)$ and we can also use the BCG ages to constrain cosmological parameters.

Keywords: galaxies: clusters: general – galaxies: elliptical and lenticular; cD – galaxies: kinematics and dynamics. galaxies: stellar content.

"In the Name of Allah, the Most Beneficent, the Most Merciful. All the praises and thanks be to Allah, the Lord of the 'Alamin (mankind, jinns and all that exists). The Most Beneficent, the Most Merciful. The Only Owner of the Day of Recompense. You (Alone) we worship, and You (Alone) we ask for help. Guide us to the Straight Way... The Way of those on whom You have bestowed Your Grace, not of those who earned Your Anger, nor of those who went astray."

— *Surah Al-Fatiha*, The Holy Qur'an 1:1-7.

Contents

List of Figures ix

List of Tables x

1 Introduction 1

1.1 Galaxy Formation . . . 1

1.2 Galaxy Clusters . . . 3

1.2.1 Cluster Properties . . . 4

1.2.2 Member galaxies . . . 6

1.3 The Sunyaev - Zel'dovich Clusters . . . 7

1.4 Brightest Cluster Galaxies . . . 8

1.4.1 BCG formation theories . . . 9

1.4.1.1 Theory 1 - Cooling Flows . . . 9

1.4.1.2 Theory 2 - Galactic cannibalism . . . 10

1.4.1.3 Theory 3 - Galaxy merging . . . 11

1.5 Star Formation in BCGs . . . 11

1.5.1 Star formation in BCGs at high redshift . . . 12

1.5.2 Star formation at low to moderate redshifts . . . 12

1.6 Measuring Stellar Populations . . . 14

1.6.1 IMF . . . 15

1.6.2 Stellar libraries . . . 17

1.7 Stellar Kinematics . . . 19
1.7.1 Velocity profiles . . . 20
1.7.2 Measuring Stellar Kinematics From Galaxy Spectra . . . 21
1.8 Outline of this work . . . 23

2 Data acquisition and reduction **24**
2.1 The cluster sample . . . 24
2.2 SALT Observations . . . 27
2.2.1 Telescope . . . 27
2.2.2 Observations . . . 28
2.3 Data reduction . . . 29
2.3.1 RSSMOSPipeline . . . 29
2.4 Finding the BCG slit . . . 30

3 Stacking and stellar kinematics **36**
3.1 pPXF . . . 37
3.1.1 The workings of pPXF . . . 38
3.2 Fitting individual BCGs . . . 41
3.3 Stacking . . . 42
3.3.1 Specstack . . . 43
3.4 Fitting stacked BCGs . . . 46
3.4.1 Results . . . 46
3.4.1.1 $0.3 < z < 0.4$ . . . 46
3.4.1.2 $0.4 \leq z < 0.5$ . . . 48
3.4.1.3 $0.5 \leq z < 0.6$ . . . 49
3.4.1.4 $0.6 \leq z < 0.7$ . . . 50
3.4.1.5 $0.7 \leq z < 0.8$ . . . 52

4 Stellar populations and star formation histories **53**

4.1 FIREFLY 54

4.1.1 How FIREFLY operates 55

4.1.2 Input and Output of FIREFLY 56

4.2 Results 57

4.2.1 Stellar Populations of the BEAMS BCGs 57

4.2.2 Weighted stellar Ages and Metallicities 69

4.3 Discussion 71

4.3.1 Age-Metallicity relation 71

4.3.2 Age-Redshift relation 72

4.3.3 Age-Dating 72

5 Summary and future work **75**

A BEAMS BCGs **79**

A.1 DES images 79

B Stacking Groups **100**

B.1 BCG stacking groups 100

List of Figures

1.1 The Cosmic Microwave Background 2

1.2 The Fornax Galaxy Cluster. 4

1.3 Galaxy cluster Abell S1063. 5

1.4 The relativity fraction of galaxy morphologies in regular clusters. 6

1.5 Visual representation of SZ cluster finding 8

1.6 Image of the UGC 2369 galaxies 11

1.7 Multicolour Image of the Phoenix BCG 13

1.8 The ingredients of galaxy SED modelling 15

1.9 Different types of IMF slopes 17

1.10 A galactic spectrum and a K0 stellar template shifted to the radial velocity of the galaxy. 19

1.11 A mock emission line profile. 21

2.1 The AdvACT cluster sample. 25

2.2 Redshift distribution of the cluster sample 26

2.3 The Southern African Large Telescope. 27

2.4 The Robert Stobie Spectrograph. 28

2.5 DES cluster image and SALT finder chart of ACT-CL J0014.0+0227 31

2.6 DES cluster image and SALT finder chart of ACT-CL J0257.7-2209. 31

2.7 DES cluster image and SALT finder chart of ACT-CL J0559.7-5249 32

2.8 DES cluster image and SALT finder chart of ACT-CL J2325.1-4111 33

3.1 Stellar and gas kinematics fit with pPXF. 37

3.2 Montage showing the change of the velocity distribution with different Gauss-Hermite parameters. 41

3.3 Example fits from pPXF for a single BCG. 42

3.4 Examples of stacked spectra from *specstack* 45

3.5 pPXF fits of group $0.3 \leq z < 0.4$. 47

3.6 pPXF fits of group $0.4 \leq z < 0.5$. 48

3.7 pPXF fits of group $0.5 \leq z < 0.6$. 49

3.7 (continued) The green symbols and pink line at the bottom are the fit residuals. The grey solid lines represent the masked regions of the "SALT chip gaps". 50

3.8 pPXF fits of group $0.6 \leq z < 0.7$. 51

3.9 pPXF fits of group $0.7 \leq z < 0.8$. 52

4.1 An example of a FIREFLY produced fit. 54

4.2 Age vs. metallicity plots for $0.3 < z < 0.4$. 59

4.3 Age vs. metallicity plots for $0.4 \leq z < 0.5$ 61

4.4 Age vs. metallicity plots for $0.5 \leq z < 0.6$ 63

4.5 Age vs. metallicity plots for $0.6 \leq z < 0.7$ 65

4.6 Measured ages of the individual groups for MILES model using the Kroupa IMF 66

4.7 Measured ages of the individual groups for the STELIB model using the Kroupa IMF 66

4.8 Measured ages of the individual groups for the MaStar model using the Kroupa IMF 67

4.9 Measured ages of the individual groups for the MILES model using the Salpeter IMF 67

4.10 Measured ages of the individual groups for the STELIB model using the Salpeter IMF 68

4.11 Measured ages of the individual groups for the MaStar model using the Salpeter IMF 68

4.12 Mean weighted ages for all models for the Kroupa IMF 69

4.13 Mean weighted ages for all models for the Salpeter IMF. 70

4.14 Mean weighted metallicities for all models for the Kroupa IMF 70

4.15 Mean weighted metallicities for all models for the Salpeter IMF. 71

4.16 BEAMS BCGs, 2SLAQ LRGs and MegaZ-LRG Ages 73

List of Tables

2.1 BEAMS BCG data 35

3.1 Stacking z ranges 43

3.2 Recovered velocity dispersions for $0.3 < z < 0.4$ 46

3.3 Recovered velocity dispersions for $0.4 \leq z < 0.5$ 48

3.4 Recovered velocity dispersions for $0.5 \leq z < 0.6$ 49

3.5 Recovered velocity dispersions for $0.6 \leq z < 0.7$ 50

3.6 Recovered velocity dispersions for $0.7 \leq z < 0.8$ 52

4.1 FIREFLY results for $0.3 \leq z < 0.4$. 58

4.2 FIREFLY results for $0.4 \leq z < 0.5$. 60

4.3 FIREFLY results for $0.5 \leq z < 0.6$. 62

4.4 FIREFLY results for $0.6 \leq z < 0.7$. 64

4.5 Mean weighted properties of the BEAMS BCGs at different *redshift* intervals 69

Table of abbreviations

Å	Angstrom
ΛCDM	Lambda Cold Dark Matter
AdvACT	Advanced Atacama Cosmology Telescope
ACTPol	Atacama Cosmology Telescope Polarization Experiment
AGN	Active Galactic Nuclei
BCG	Brightest Cluster Galaxy
BEAMS	Brightest cluster galaxies Evolution with AdvACT, MeerKAT and SALT
CALIFA	Calar Alto Legacy Integral Field Area Survey
CCD	Charged Coupled Device
CDM	Cold Dark Matter
CF	Cooling flow
CMB	Cosmic Microwave Background
DES	Dark Energy Survey
DM	Dark matter
EAGLE	Evolution and Assembly of Galaxies and their Environments
ESO	European Southern Observatory
FIREFLY	Fitting Iteratively for Likelihood Analysis
FWHM	Full-Width Half-Maximum
H	Hydrogen
He	Helium
GIPSY	Groningen Image Processing System
gE	giant Elliptical
HST	Hubble Space Telescope
ICM	Intracluster Medium
IFU	Integral Field Unit
IMF	Initial Mass Function
INT	Isaac Newton Telescope
IR	Infrared
LOSVD	Line-Of-Sight Velocity Distribution
LRGs	Luminous Red Galaxies
$M_\odot$	Solar Mass
M/L	Mass-to-light ratio

MaNGA	Mapping Nearby Galaxies at APO
MaStar	MaNGA Stellar Library
MILES	Medium-resolution INT Library of Empirical Spectra
Mpc	Megaparsec
NASA	National Aeronautics and Space Administration
pPXF	Penalised PiXel Fitting
RSS	Robert Stobie Spectograph
S/N	Signal-to-Noise ratio
SALT	Southern African Large Telescope
SAMI	Sydney-AAO Multi-object Integral-field spectrograph
SAURON	Spectrographic Areal Unit for Research on Optical Nebulae
SB	Surface Brightness
SDSS	Sloan Digital Sky Survey
SF	Star Formation
SFH	Star Formation History
SFR	Star Formation Rate
SPS	Stellar Population Synthesis
SSP	Simple Stellar Population
SPT	South Pole Telescope
STECKMAP	Stellar Content and Kinematics via Maximum likelihood A Posteriori
SZ	Sunyaev-Zel'dovich
RSS	Robert Stobie Spectograph
TES	Transition Edge Sensor
UV	Ultraviolet
VENGA	VIRUS-P Exploration of Nearby Galaxies
VLT	Very Large Telescope
VST	VLT survey telescope
z	Redshift

Chapter 1

Introduction

> "When you focus on the past, that's your ego. "I did [this] in the past. I won [that] in the past." And When I focus on the future, that's my pride. "I'm going to dominate". That's your pride talking. I try to focus on the moment. In the present. And that's humility."
>
> Giannis Antetokounmpo

In this dissertation, we perform an observational study of brightest cluster galaxies at intermediate redshifts ($0.3 < z < 0.8$). We are particularly interested in the kinematics and star formation histories of these galaxies over this 3.4 Gyr time period. Here, we set the stage by first summarising the current understanding of the processes which shape galaxy formation and evolution, thereafter we narrow our focus to take a look at brightest cluster galaxies and then we provide some background for subsequent Chapters. We end the Chapter with a summary of the open questions this dissertation attempts to answer.

1.1 Galaxy Formation

Some $\sim$ 14 Gyr ago, the Universe as we know it was created out of a hot, dense singularity in an event known as the Big Bang. After the Big Bang, the temperature became so high that all matter in the Universe was ionized. After some time the universe cooled so that electrons could recombine into atoms. Once recombination was complete, the photons stopped scattering and propagated freely through space. It was only about $\sim$ 400 000 years after the events of the Big Bang, when we were able to get information (in the form of radiation) from the Universe, as these were the first photons that were not absorbed

by atoms (Rodríguez Del Pino, 2015). This first radiation, first observed by Penzias & Wilson (1965) can be seen in the Cosmic Microwave Background (CMB), a relic of the sudden explosion of the Universe from its initial state and is regarded as one of the greatest successes of the Big Bang model. From the CMB data, it can be observed that after the Big Bang, the Universe, for a time, was remarkably homogeneous (see Figure 1.1). However, small temperature fluctuations corresponding to regions of different densities led to the formation of the first structures in the Universe. These fluctuations in the primordial and permeating radiation field would become the seeds of the densest regions of cosmic web.

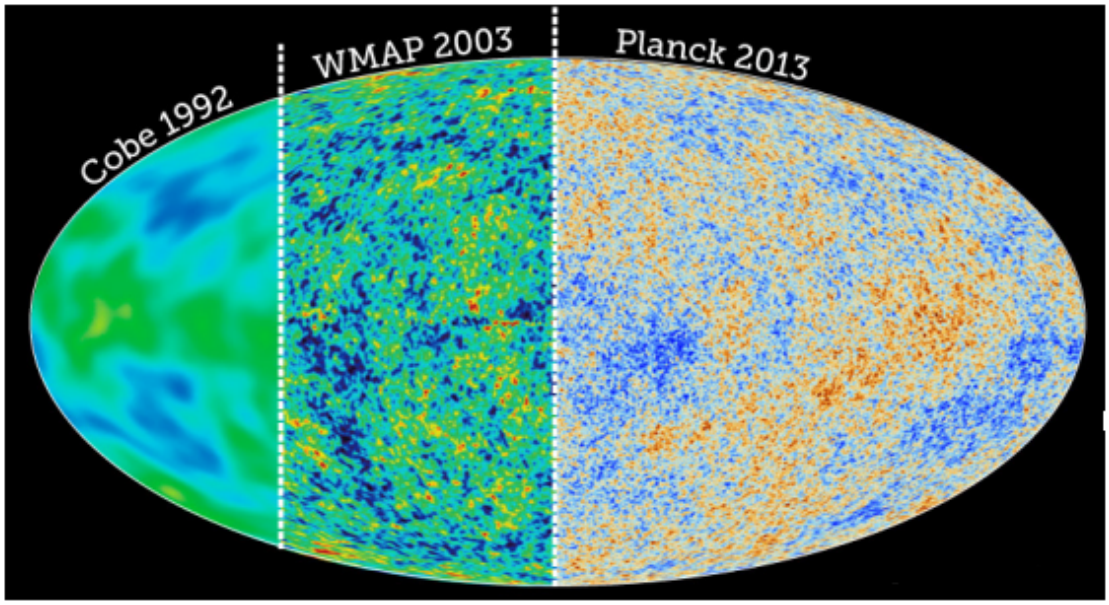


Figure 1.1: The Cosmic Microwave Background (CMB) is the cooled remnant of the first light that could ever travel freely throughout the Universe. Featured on this map are the temperature fluctuations observed in the CMB using the COBE, WMAP and Planck data. Figure taken from Vázquez et al. (2018).

Around this time, the growth of structure of the Universe was dominated by dark matter, which is an invisible component of the Universe that only interacts gravitationally and therefore does not emit any electromagnetic radiation. The existence of this component was first introduced by Zwicky (1933), and has been used by Rubin et al. (1980) to explain the rotation curves of Spiral galaxies, moreover it has also been used to explain many other astrophysical observations. The current model of the Universe assumes a non-relativistic, Cold Dark Matter (CDM), to explain the observed large-scale structure of the Universe (Peebles, 1982; Rodríguez Del Pino, 2015).

The structural growth of the Universe then proceeded hierarchically: Dark matter haloes built around these seeds via gravitational instability and gas fell into these overdensities by radiating away some of its energy. The first stars in the universe formed from the primordial gas due to the gravitational collapse of the gas clouds at the centres of the haloes (Prichard, 2018). And eventually the first galaxies were then formed from the stars and gas assembled by the haloes (Rodríguez Del Pino, 2015).

However, the hierarchical formation scenario discussed above is not the only model of galaxy formation that has been proposed. A competing scenario suggests that galaxies are formed through the gravitational collapse of primordial gas clouds (Eggen et al., 1962). In spite of all the evidence supporting the hierarchical formation scenario, there are still some unanswered questions. One of these questions comes from the the old ages that are found in massive Elliptical galaxies. These galaxies are known to be some of the oldest galaxies in the Universe, dominating clusters at $z = 0$, whereas spiral galaxies are younger (and are usually still undergoing star formation) and typically found in less dense environments. Studies of the passive red galaxies that dominate the Local Cluster have shown that most of their stars formed at $z > 2$ (Bower et al., 1992; Aragón-Salamanca et al., 1993), indicating that the cluster population evolved passively over the last ~ 8 Gyr (Zhao, 2016). These results agree with the Monolithic formation model over the current hierarchical formation scenario and predicts that clusters will continue to grow through galactic accretion. In this formation scenario, stellar disks are the first component of the galaxy that formed, and the elliptical and bulging spiral galaxies were later formed by the merger of the pre-existing galactic disks (e.g. Kauffmann et al., 1993).

Although there is progress still to be done in polishing the details of the hierarchical galaxy formation picture, it seems to be an excellent framework to study galaxy evolution in a ΛCDM Universe [1].

1.2 Galaxy Clusters

Galaxy clusters are the extremely high-mass end of the dark matter halo mass distribution, and are amongst the most massive gravitationally bound objects that have been observed (Abell, 1958; Bahcall, 1999). Galaxy clusters consist of anywhere from hundreds to thousands of galaxies compared to galaxy groups which have roughly 10 - 50 galaxies. Clusters are made up of a dark matter halo which contains a superheated plasma atmosphere called the intracluster medium (ICM), and galaxies. They have typical masses of about 10^{14} - 10^{15} $M_\odot$. The typical mass of a galaxy cluster is comprised of $\sim$ 83-89% dark matter, $\sim$ 10 - 15% ICM, and $\sim$ 1-2% member galaxies (Lin et al., 2003; Sanderson et al., 2003; Vikhlinin et al., 2006).

In the study of galaxy clusters the two biggest and most-used catalogues were compiled by Abell (1958) and Zwicky et al. (1961). Both Abell (1958) and Zwicky et al. (1961) proposed different criteria for the inclusion of clusters in their respective catalogues, i.e. how clusters are defined and how their members are distinguished from the field, such that proprieties, like the distributions of member galaxies, total size of the cluster or total population, depends on these definitions. Figure 1.2 shows the Fornax cluster, an example of a "rich galaxy cluster".

[1] ΛCDM refers to a Universe dominated by dark energy (Λ) and CDM

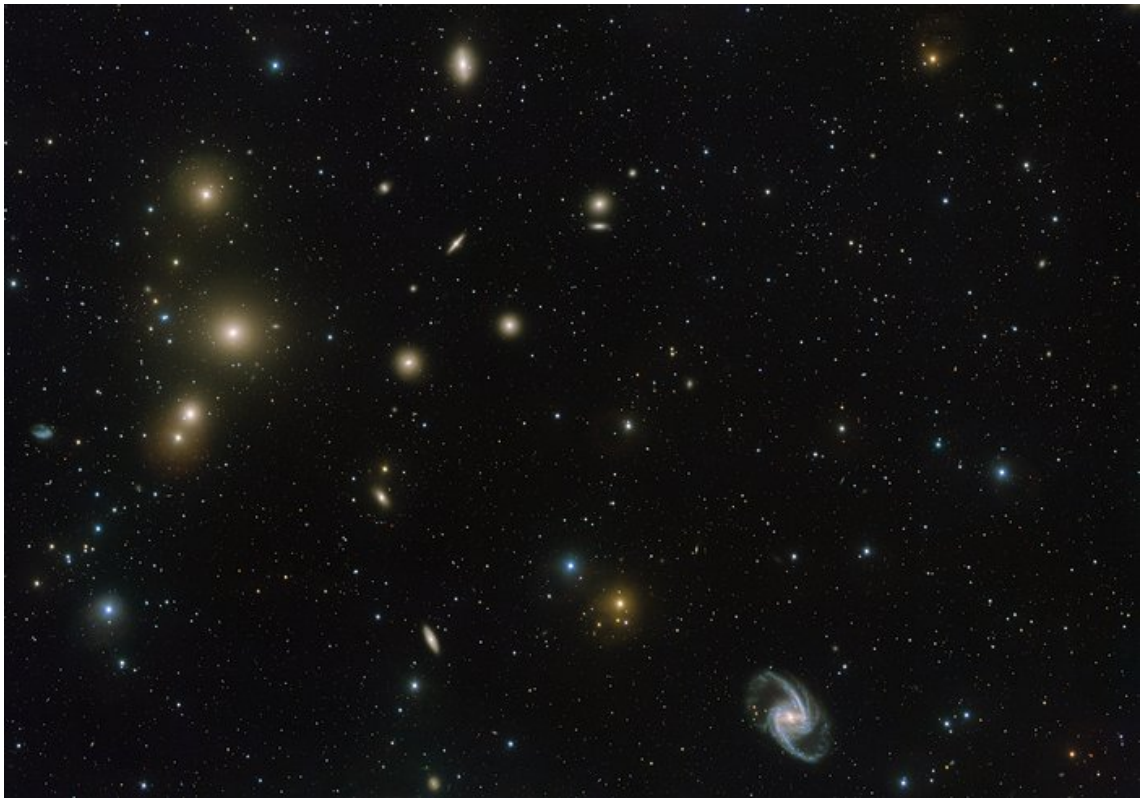


Figure 1.2: Image of the Fornax cluster as observed with the VLT survey telescope (VST). The Fornax galaxy cluster is one of the closest of such groupings beyond our Local Group of galaxies. This VST image shows the central part of the cluster lensing. Image taken from ESO. Acknowledgement: Aniello Grado & Luca Limatola.

1.2.1 Cluster Properties

Richness and compactness

A cluster's richness is a statistical measure of the number of galaxies within the said cluster (Sarazin & Boller, 1989). Zwicky et al. (1961) defined it as galaxies located in the isopleth that is twice the field density as members of the cluster. Zwicky et al.'s definition leads to a richness that depends on the redshift of the cluster. Moreover, Abell (1958) defined the richness of a cluster in a distance-independent way; members of the cluster were galaxies with apparent magnitudes between m_3 and $m_3 + 2$, where m_3 is the apparent magnitude of the third brightest member. In this count, only galaxies that are within the so-called "Abell radius" [2] are considered members of the cluster; this parameter describes the compactness of the cluster. According to Abell's criterion, a cluster must have a richness of at least ~ 50[3] members. Moreover, Abell described rich clusters as those that have a richness of more than 50 members between m_3 and $m_3 + 2$, whereas poor clusters are those have richness in the range from 30 to 50 members.

[2]The Abell radius is defined as 1.5 h^{-1}Mpc. In astrophysics, $h = H_0/100$ and H_o is the Hubble constant.

[3]There is not a rigorous criterion, due to presence of foreground galaxies which could make errors in the identification.



Figure 1.3: The galaxy cluster Abell S1063, a regular cluster. A central concentration of galaxies and a symmetric shape can be noted. Image taken from NASA.

Morphology and dynamical state

Clusters are divided into morphology classes, that can be represented as a one-dimensional sequence, ranging from regular to irregular clusters (Abell, 1965). Regular clusters are clusters that have a population greater than 10^3 in the interval of the 6 brightest magnitudes (Wilson, 2012). These clusters have a a high central concentration of galaxies and show spherical symmetry. They are mostly made up of Elliptical and S0 galaxies (Wilson, 2012). On the other hand, irregular clusters vary from poor to relatively rich with little or no symmetry and no marked concentrations. Irregular clusters contain all types of galaxies, with Spiral galaxies being the most common type among the brighter galaxies (Wilson, 2012). This suggests that regular clusters are, in some sense, dynamically relaxed systems, while irregular clusters are dynamically less-evolved and have preserved roughly their distribution of formation (Leveque, 2017). An example of a regular galaxy cluster is shown in Figure 1.3.

1.2.2 Member galaxies

The relative number of galaxies of a specific morphological type in a cluster are determined by the cluster's dynamical state. S0 and Elliptical galaxies are the most common type in regular clusters, unlike what is observed in irregular clusters or in the field (Leveque, 2017). In regular clusters, as can be seen in Fig. 1.4, the relative number of a morphological type depends on the cluster radius or density. De-projecting in three dimension, the observable position of galaxies within the cluster shown in Figure 1.4, the number of Spirals decreases from 80% in the field to 60% in the outskirts of cluster until to 0% in the center, whereas a relative opposite increase of S0 and Elliptical galaxies is observed (Dressler, 1980) . This is known as the morphology-radius relation in clusters.

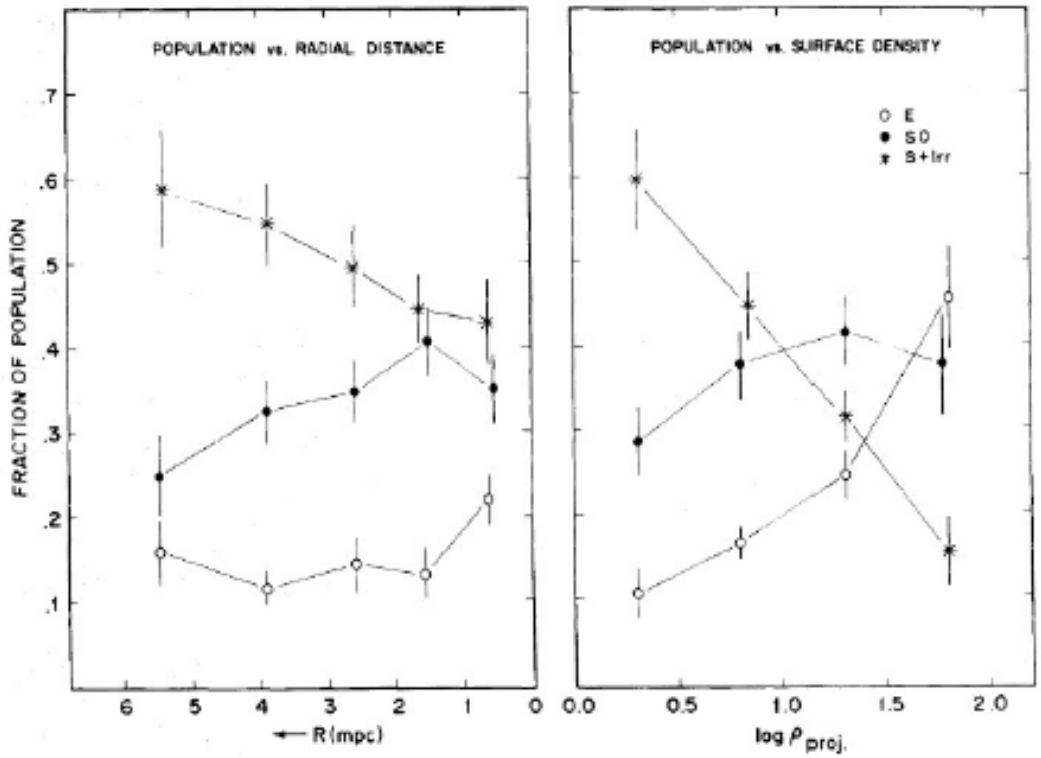


Figure 1.4: The relativity fraction of galaxy morphologies in regular clusters as a function of radial distance from the cluster centroid (**left panel**) and as a function of local surface density (**right panel**). Image taken from Dressler (1980).

A systematic variation of the star formation rates (SFR) and galaxy stellar populations with the environment is observed alongside the morphology-density relation. Galaxies found in denser environments, are on average, found to have older stellar populations and a reduced star formation (SF) activity compared to the field galaxies (Leveque, 2017). However, the SFR does not vary with the environment so simply; it seems to have the highest values in the environments of poor clusters compared to the low density regions such as the field or in high density regions such as rich clusters.

Associated with the shown anti-correlation between the fraction of S0 and Spiral galaxies

in the cluster outskirts, a non-negligible number of 'anemic' Spirals is observed in clusters; this type of galaxy presents a less pronounced interarm contrast, less amount of gas, low SF activity and redder colour than normal Spirals with similar bulge-to-disk ratio (Leveque, 2017). By contrast, the center of regular clusters is usually dominated by a single very luminous galaxy (see Fig. 1.3), or by a pair of very bright galaxies (Morgan & Lesh, 1965). The single luminous galaxy is called the "cD" galaxy. cD galaxies are similar to Elliptical or Lenticular galaxies, but they have an extended halo of low surface brightness (SB). It is believed that cD galaxies are produced by mergers of massive galaxies, most likely in the core of subclusters or groups (Rood, 1965; Leveque, 2017).

1.3 The Sunyaev - Zel'dovich Clusters

The Sunyaev - Zel'dovich (SZ) effect (Sunyaev & Zeldovich, 1970, 1972) is the spectral distortion of the CMB through inverse Compton scattering by high-energy electrons in galaxy clusters, in which the low-energy CMB photons receive an average energy boost during collision with the high-energy cluster electrons. The SZ effect allows the construction of cluster samples that are independent of redshift that are effectively mass limited. Typically, the SZ effect is split into two components: a thermal SZ effect where the CMB photons interact with electrons that have high energies due to their temperature and a kinetic SZ effect, a second-order effect where the CMB photons interact with electrons that have high energies due to their bulk motion. In this section, we only discuss the thermal SZ effect, this part of the SZ effect dominates over the kinetic SZ effect in galaxy clusters.

The thermal SZ effect arises as CMB photons are scattered upwards in energy by their encounters with energetic electrons in a process known as the inverse Compton scattering (Sunyaev & Zeldovich, 1970). This causes a change in the observed spectral flux density of the CMB that is dependent on the energy of the CMB photons being observed (Sunyaev & Zeldovich, 1970, 1972). To illustrate, at frequencies greater than $\sim$ 217 GHz the spectral flux density in the direction of a galaxy cluster will increase, whereas at lower frequencies it will decrease. This occurs because the total number of photons is conserved and thus the number of relatively low energy photons is depleted as these are scattered towards higher energies (Henden, 2019). Figure 1.5 shows an illustration of how the SZ signal can be used to identify galaxy clusters in maps of the CMB.

The thermal SZ Compton parameter (Sunyaev & Zeldovich, 1972) in a given direction, $\hat{n}$, can be expressed as

$$y(\hat{n}) = \int \frac{k_B T_e}{m_e c^2} n_e \sigma_T \mathrm{d}l, \tag{1.3.1}$$

where k_B is the Boltzmann constant, m_e is the electron mass, c is the speed of light, σ_T is the Thomson cross section, dl the distance along the line of sight. And n_e and T_e are the

electron number density and temperature of the scattering medium. Since the product of the density and temperature is proportional to pressure, the Compton y parameter is effectively a measure of the integrated electron pressure of a hot gas along the line of sight (Henden, 2019). An important result is that the Compton y parameter is independent of the redshift and depends only on the properties of the scattering medium. In this case it is the intracluster medium. This enables the detection of high redshift clusters that are indistinguishable at optical and X-ray wavelengths (Henden, 2019).

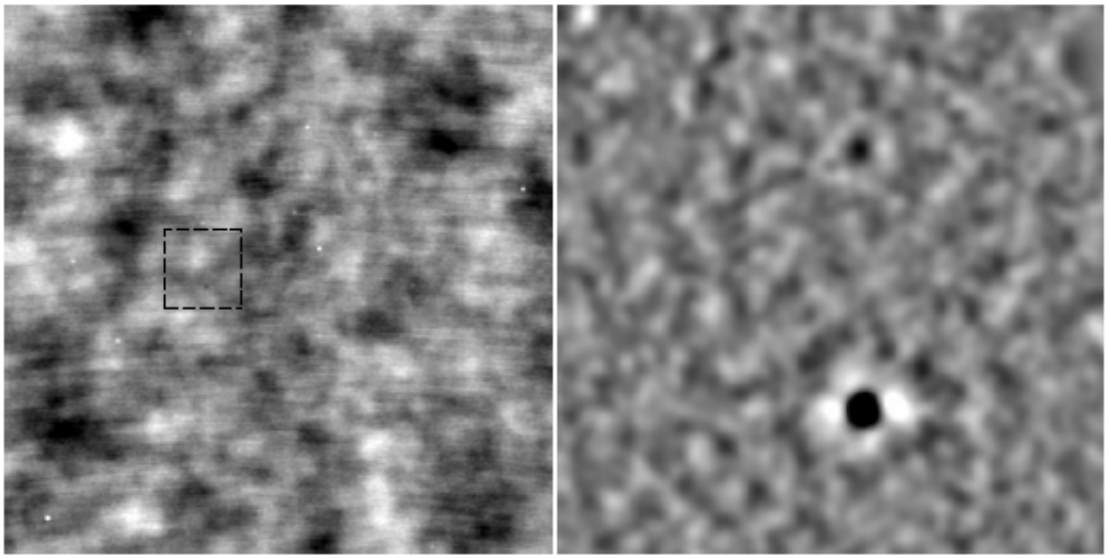


Figure 1.5: **Left Panel:** A 6°-by-6° cut-out of the 150 GHz map of the CMB from the South Pole Telescope (SPT)-SZ data (Bleem et al., 2015) over the temperature range $\pm 3 \times 10^{-4}$ K is shown. The primary CMB anisotropies on degree scales are clearly visible. The white spots are emissive point sources, usually radio or infrared galaxies. At this frequency the SZ signal is negative, and so the cluster appears as 'shadows' against the CMB. **Right Panel:** a zoom in on the 1°-by-1° area near one such cluster as indicated by the dashed square on the left. A spatial filter has been applied to enhance the signal-to-noise ratio (S/N) on cluster scales and the map is in units of S/N over the range $-5 < \mathrm{S/N} < 5$. The cluster appearing as a strong SZ decrement in the bottom of the right panel has been optically confirmed at $z = 1.132$. Figure adapted from Henden (2019).

1.4 Brightest Cluster Galaxies

Brightest Cluster Galaxies (BCGs) are defined as the brightest or first ranked galaxy in a cluster and are the most massive galaxies in our Universe (Lauer et al., 2014). These galaxies exist in extreme merger environments which allows them to grow to be some of the most massive ($\sim 10^{13} \mathrm{M}_{\odot}$) galaxies in the Universe. A typical BCG is located near the centre of its parent cluster and is well-aligned with the cluster galaxy distribution suggesting that it lies at the bottom of the cluster's gravitational potential well (Von Der Linden et al., 2007; Loubser et al., 2020). They appear to have a distinct luminosity

function, with respect to other cluster Ellipticals, or bright field galaxies. Their properties generally correlate with those of their parent cluster; such as between the BCG stellar mass and cluster mass (Lidman et al., 2012; Stott et al., 2012), and they exhibit small velocity offsets relative to their host clusters. These observations, as well as others, indicate that the evolution of BCGs is intrinsically linked to that of their parent cluster and distinct from those of other galaxies. The origin and evolution of BCGs is closely related to that of their host cluster, and therefore they can provide direct information on the formation and history of large-scale structures in the Universe (Conroy et al., 2007).

1.4.1 BCG formation theories

The uniqueness of the properties of BCGs indicates that these supergiants have rather unusual formation histories compared to ordinary Elliptical galaxies. A number of theories have been proposed to explain the formation of BCGs. One of the earliest scenarios was the cooling flow model, which suggests that the BCG forms as a result of condensation of the ICM flowing into the center of the cluster, leading to intense episodes of star formation (Cowie & Binney, 1977; Fabian, 1994). Another early prediction was that BCGs form from galactic cannibalism, as a result of dynamical friction (White, 1976; Ostriker & Hausman, 1977). In this section, the three main theories proposed over the last few decades to explain the properties of BCG are discussed.

1.4.1.1 Theory 1 - Cooling Flows

In this theory, the formation of BCGs is caused by the presence of cooling flows (CFs) found in galaxy clusters (Cowie & Binney, 1977; Fabian, 1994; Loubser, 2009). In the local Universe cooling-flow clusters are a common occurrence and in centre of these systems we often find BCGs (Edwards et al., 2007). If the central cluster is dense enough, the gas within the cluster can condense to form stars at the bottom of the potential well. The radiative cooling time of the gas within the cluster is short enough for the gas to cool and settle at the centre of the cluster, suggesting that cD envelopes may arise from this gradual deposition of cold gas (Loubser, 2009).

Several observations supported this idea. McNamara et al. (1996) studied the Abell 1795 galaxy cluster and found ultraviolet- and blue-light excesses in its central galaxy. This is an indication of active star formation in the core of the cluster. In another study by Salome & Combes (2003), they directly detected molecular gas in some of the central galaxies in clusters. Further observational evidence in support of the CF theory is examples of BCGs in cool-core clusters that showed signs of recent SF activity, i.e. blue cores and UV-excess (e.g. Crawford et al., 1999; McNamara et al., 2006). Groenewald & Loubser (2014) and Loubser et al. (2016) found some presence of young stellar populations on their respective studies of cool-core clusters.

On the other hand, many observations over the years have cast doubt over this theory. According to the cooling-flow scenario, a very large number of new stars should be created in the cluster cores, but there is no observational evidence for this population (McNamara & O'Connell, 1989). Moreover, McNamara & O'Connell (1992) showed that the observed star formation can account for only a few percent of the material that is cooling and accreting on to the central galaxy. The cooling-flow theory also predicts colour gradients such that the halo around BCGs should become redder with increasing radius. However, such gradients have not been found (Andreon et al., 1992). Recently, observations have demonstrated that the X-ray gas does not cool enough (Kaastra et al., 2001; Peterson et al., 2001; Tamura et al., 2001; Jordán et al., 2004). Since central cluster galaxies are more likely to host radio-loud Active Galactic Nuclei (AGN) (Von Der Linden et al., 2007), feedback from AGN may counteract the radiative cooling in cluster cores, making the BCG formation from cooling flows unlikely. However the flows play an important role in regulating the rate at which gas cools at the centres of groups and clusters (Loubser, 2009).

1.4.1.2 Theory 2 - Galactic cannibalism

Another BCG formation and evolution theory is known as "galactic cannibalism". This theory is currently the most widely *accepted* formation theory for BCGs, this theory was first proposed by Ostriker & Tremaine (1975) and further developed by Ostriker & Hausman (1977). The process called galactic cannibalism is the process through which a central galaxy is formed through the mergers/capturing of less massive objects. This result was first confirmed by Dubinski (1998) who found that by using a N–body simulation of galaxy clusters, that mergers would naturally produce a central galaxy resembling the surface brightness profile and velocity dispersion of a BCG (Viljoen, 2012).

However, the galactic cannibalism scenario fails when worked out in detail. This is based on the fact that on average clusters of galaxies have very high velocity dispersions, which makes frequent galaxy mergers very unlikely to take place. Many studies such as those of Merritt (1985) and Tremaine (1990), have argued that the dominance of BCGs seen in observations cannot be achieved via cannibalism of other cluster members alone. A disadvantage of this theory is that the luminosity expected from the matter accreted through mergers, does not match the luminosities of the BCGs given in the literature. This is due to the fact that the duration of the dynamical friction timescales are generally too long (Viljoen, 2012). The failure of this model suggests that BCGs must have an earlier origin. A possible alternative scenario is galaxy merging during cluster collapse in a hierarchical formation model.

1.4.1.3 Theory 3 - Galaxy merging

This theory was first proposed by Merritt (1983) it is also known as the primordial origin theory. This theory suggests that BCGs originated early on in the history of the Universe through rapid galaxy mergers that took place during the cluster collapse (Merritt, 1984, 1985). Thereafter; frequent mergers of galaxy clusters are constrained by the high relative velocities between clusters. Merritt (1983) argued that all galaxies had large haloes early in the life of the cluster. These haloes were then removed by the mean cluster tidal field during the initial collapse and returned to the cluster potential, except for the central member, which was unaffected due to its specific position relative to the cluster potential (Loubser, 2009). Figure 1.6 shows an example of two galaxies merging.

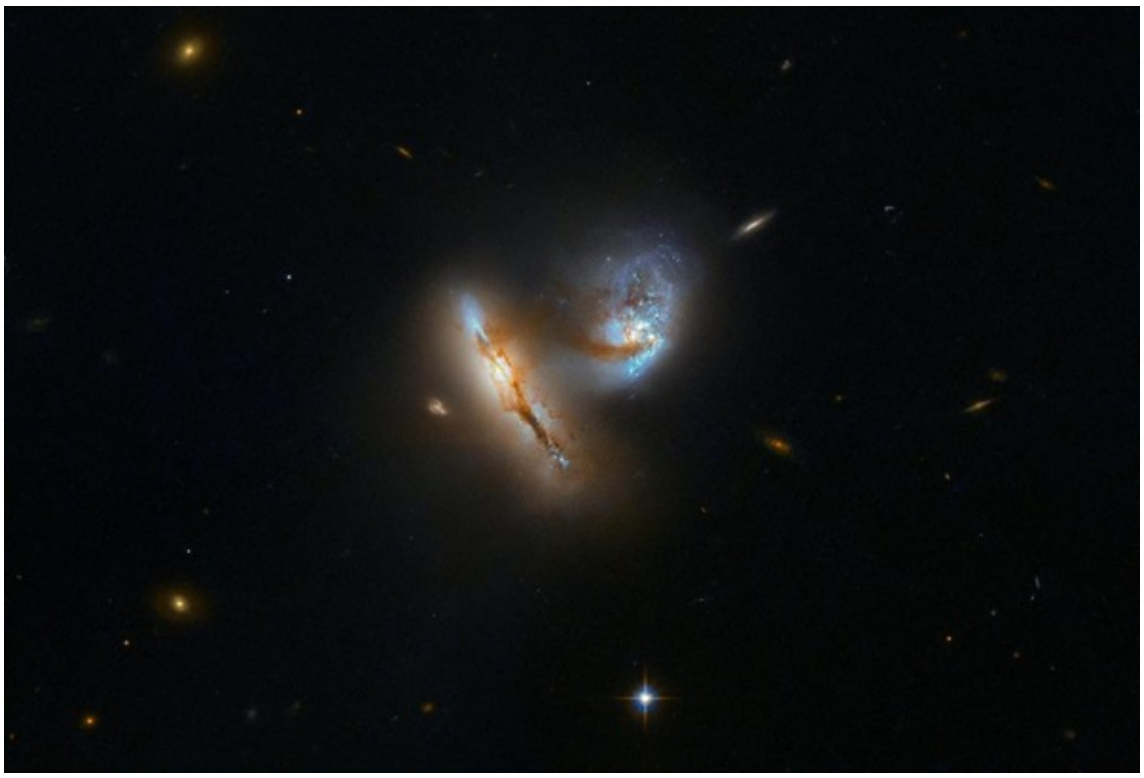


Figure 1.6: A true colour optical image of the UGC 2369 galaxies as observed with the Hubble Space Telescope (HST). This image shows a pair of interacting galaxies, UGC 2369N (**right**) and UGC 2369S (**left**), that are in the process of merging. Image courtesy of ESA/Hubble/NASA.

1.5 Star Formation in BCGs

BCGs exhibit merger-driven mass growth at far greater rates than those found in field galaxies owing to their positions in galaxy-rich cluster environments (Von Der Linden et al., 2007). As a result, these galaxies can be many times more massive than other galaxies in the cluster environment, and extensive merger histories can result in BCGs having flatter central surface brightness profiles than other cluster Ellipticals (Lauer et al.,

2007; Bernardi et al., 2007; Lauer et al., 2014). However, this merger history produces very little star formation, since both the BCG and the satellite galaxies that merge with it are ram-pressure stripped by moving through the ICM (Ruszkowski & Springel, 2009). However, the star formation that does occur in BCGs is typically either a product of initial proto-BCG and proto-cluster formation or mergers at high-redshift, or due to ICM cooling and feedback in low- to intermediate redshift clusters (Webb et al., 2017).

1.5.1 Star formation in BCGs at high redshift

Observations of proto-clusters have recently revealed clues about the initial stages of BCG formation. Images obtained with the HST show galaxies in the centers of forming clusters which are the site of sprawling bursts of star formation ignited when infalling progenitor galaxies merge or initial cooling flows spark massive starbursts (Webb et al., 2015a). This initial mass growth is believed to peak before a redshift of $z = 1$, after which in situ star formation quickly becomes a negligible component driving BCG mass growth (Webb et al., 2015b).

While initial predictions indicated that BCGs formed most of their stellar mass during this initial period of robust star formation, some semi-analytical models predict that BCGs double or triple in stellar mass between $z = 1.0$ and the present day (De Lucia & Blaizot, 2007; Tonini et al., 2012). This mass growth is believed to be merger driven (Ruszkowski & Springel, 2009; Liu et al., 2009). Satellite galaxies falling into the potential well of the dark matter halo are essentially swallowed up by the BCG. In simulations, by late times this often takes the form of gas-poor satellites accreting onto a main progenitor without fueling star formation, although above $z \sim 0.6$, galaxy mergers in young clusters may drive elevated rates of star formation (McDonald et al., 2016).

1.5.2 Star formation at low to moderate redshifts

BCG star formation is unusual in the sense that the old stellar populations and overall Elliptical morphologies of BCGs suggests that star formation is not fueled by a molecular gas-rich ISM. Crawford et al. (1999); Edwards et al. (2007) found that a majority of BCGs (between $\sim$ 70 - 80% depending on the sample selection) are quiescent red galaxies. However, starbursts in low- to moderate redshift BCGs span several orders of magnitude. The SFR in the most extreme recorded BCG starburst, found in the Phoenix Cluster, is $\sim$ 500 - 2000 $M_\odot$ yr^{-1} (Mittal et al., 2016).

The observations of Spatially resolved "active" BCGs at $z \lesssim 0.6$ demonstrate that the majority of optical line and UV emission in these galaxies is situated in extended knot-and-filament structures (see Figure 1.7, for example). Star forming nebulae in BCGs can extend tens of kpc from the BCG center. Therefore, while some of the emission is due to AGN activity, the majority is most likely due to recent star formation (Conselice et al.,

2001; O'Dea et al., 2004; McDonald & Veilleux, 2009; McDonald et al., 2014; Tremblay et al., 2012, 2015). A handful of BCGs harbor type II quasars, with sizable optical fluxes, while most active BCGs do not have bright AGN (Kirk et al., 2015).

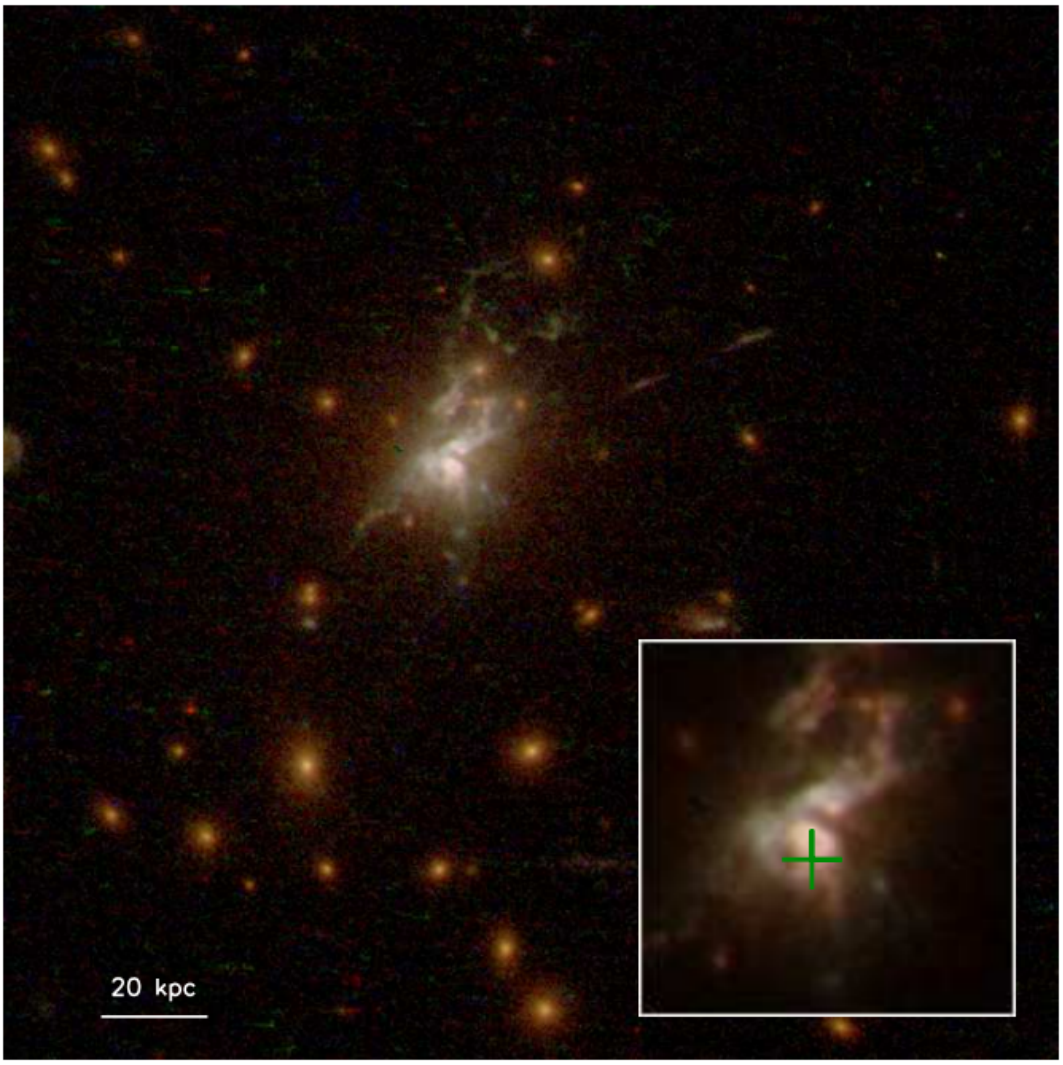


Figure 1.7: A combined color image of SPT-CL J2344–4243 also known as the Phoenix Cluster BCG initially detected with the South Pole Telescope (SPT). Blue knots and filaments are regions of enhanced star formation, and extend tens of kpc from the center of the BCG. The inset in the lower right details the complex structure of the starburst in the center of the BCG, along with the position of an X-ray point source (green cross). Image taken from McDonald et al. (2013).

Multiple lines of evidence suggest that BCG star formation is fueled by radiatively cooled ICM gas. BCGs found at the bottom of the gravitational potential well of clusters with cool ICM cores exhibit star formation with an incidence of $\sim 70\%$ (Edwards et al., 2007; Donahue et al., 2010). Furthermore, the entropy of the ICM in a clusters core is a reliable indicator of whether the BCG will exhibit star formation or not; clusters with core entropies ≤ 30 keV cm^2 host active BCGs, while clusters with higher core entropies overwhelmingly do not (Hoffer et al., 2012; Loubser et al., 2016, 2021).

1.6 Measuring Stellar Populations

The concept of stellar populations was first introduced by Baade (1944). The concept of stellar population synthesis (SPS) was originated by Faber (1972) and it is still the technique that is in use today, and has been called the "evolutionary population synthesis" by Maraston (1998). The aim of a stellar population analysis is to define the distribution of ages and metallicities of a given population and then connect that information to different formation and evolution scenarios (Worthey, 1994).

The simple stellar population (SSP), which describes the evolution of a single stellar population's spectral energy distribution (SED) at a single metallicity and abundance pattern, acts as the starting point for all stellar population models (Conroy, 2013).

The stars within a collection of stars may have more or less the same age, or may have ages that differ by billions of years, this may have been caused by several star formation episodes. The simplest form of stellar populations is the SSP, which, according to Salaris & Cassisi (2005), consists of stars that have formed at the same time in a burst of star formation. SSPs have a number of natural counterparts, such as open and globular clusters, some Dwarf galaxies as well as some Elliptical galaxies.

Moreover, Elliptical galaxies can sometimes have different star formation epochs, this can be due to cooling flows of mergers, the host cluster and other factors. This can lead to a stellar system that is better described by a composite stellar population (CSP), which may consist of at least two different formation epochs.

We turn our focus on how an SSP is built. An SSP is dependent on three ingredients: isochrones (which are influenced by the stellar evolution theory), the initial mass function (IMF) and spectral libraries, as shown on Figure 1.8. Conroy (2013) described the output of an SSP mathematically as (their Equation 1):

$$f_{\rm SSP}(t, Z, \lambda) \;=\; \int_{M_{\rm low}}^{M_{\rm high}} f_{\rm star}(T_{\rm eff}(M), \log g(M) | t, Z, \lambda) \Phi(M) dM \tag{1.6.1}$$

Here, $f(t, Z, \lambda)$ is the flux at time t, for a star or an SSP of metallicity Z, at wavelength λ and M is the initial (zero-age main sequence) stellar mass. The integration is over all masses of the star, usually between $M_{\rm low} = 0.08 M_{\odot}$ (the hydrogen burning limit) and 100 $M_{\odot}$. $\Phi(M)$ is the initial mass function, which describes the distribution of stellar masses in an SSP, i.e. the proportion of massive stars to low-mass stars (Conroy, 2013). The properties of each individual star (its effective temperature, $T_{\rm eff}$, and surface gravity, $\log g$) are determined by the use of an empirical isochrone. An isochrone places each star in a single-age population on the Hertzsprung-Russell diagram, and tracks their evolution in Luminosity- $T_{\rm eff} - \log g$ space as the population ages (Conroy, 2013).

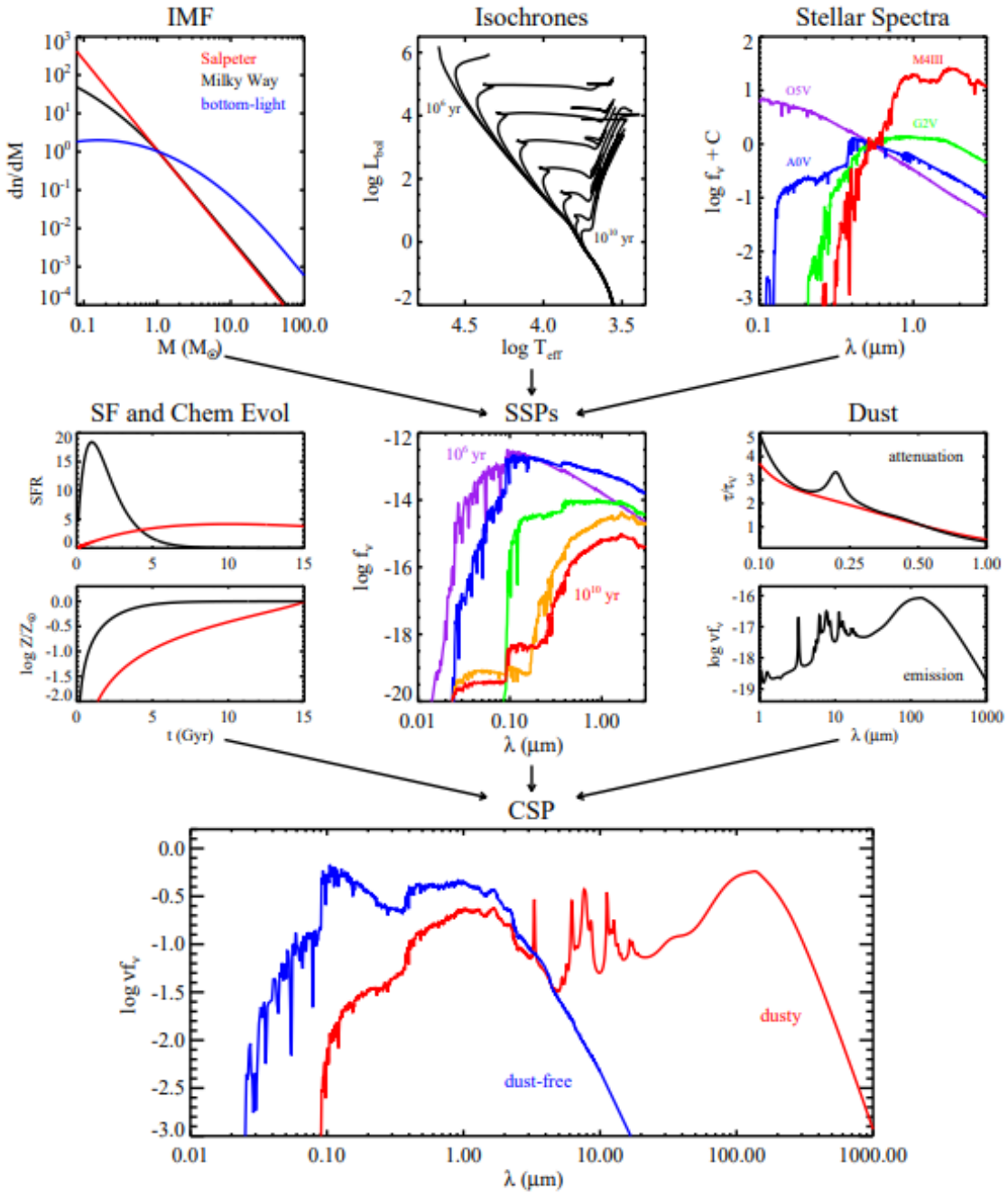


Figure 1.8: A graphical example of the various ingredients of galaxy SED modelling. Figure taken from Conroy (2013).

1.6.1 IMF

The IMF connects a variety of astrophysical phenomena including star formation, stellar feedback, the relative number of stellar remnants, and heavy element production, and is a critical ingredient in modeling the integrated light from distant galaxies (Conroy et al., 2017). The IMF is a topic that has been researched for more than 60 years (e.g. Salpeter, 1955) but is still a topic of controversy among astrophysicists (Bastian et al., 2010; Mo et al., 2010; Conroy, 2013). A great number of authors have investigated the

universality of the IMF for different types of galaxies (see, e.g. Myers et al., 2011; Dib, 2014; Ferreras et al., 2016). They found that most observations agree with the "universal IMF", however, several authors also note that there are indications of a "non-standard IMF" in extragalactic and some local environments, which needs to be investigated (Bastian et al., 2010).

It is important to include the study of the IMF whenever a study about stellar populations is conducted, as it is one of the important building blocks of SSPs. The IMF was first introduced by Salpeter (1955) as a power law and had the mathematical form:

$$\Phi(\log(m)) \;=\; \frac{dN}{d\log(m)} \;\propto\; m^{-\Gamma} \tag{1.6.2}$$

Where Φ represents the IMF, N is the number of stars with masses in the range $m+dm$, m is the mass and Γ is the slope of the IMF. Other authors such as Bastian et al. (2010) also discuss the IMF within the context of a mass spectrum, where the distribution function is in linear mass units, using the equation:

$$\chi(m) \;=\; \frac{dN}{d\log(m)} \;\propto\; m^{-\alpha} \tag{1.6.3}$$

Where χ represents the IMF and α is the slope of the IMF.

It is also important note that α and Γ cannot be used interchangeably because they are connected through Equation 1.6.4. Some authors use the linear mass equation (with α), while others prefer the logarithmic function (with Γ).

$$\alpha \;=\; \Gamma \;+\; 1 \tag{1.6.4}$$

The properties of the IMF with regards to SPS are summarised by Conroy (2013) as: The overall normalisation of the mass-to-light is determined by the IMF. For a passively evolving stellar population, the IMF also determines the rate of luminosity evolution. Moreover, for SSPs, the IMF has a small effect on the shape of the SED, but only for IMFs that are close to the Salpeter IMF. This is because in SSPs, the integrated light is mostly dominated by stars of the same mass, called the turnoff mass. However for CSPs, the IMF does affect the SED because of the range of turnoff masses contributing to the integrated light.

The main features of the stellar IMF are the peak seen at a mass of a few tenths of solar masses and a power-law tail toward higher masses (Larson, 2006). Since the introduction of the Salpeter IMF, there have been several other IMF functions and slopes that have been proposed. In Figure 1.9 a few examples of them are given.

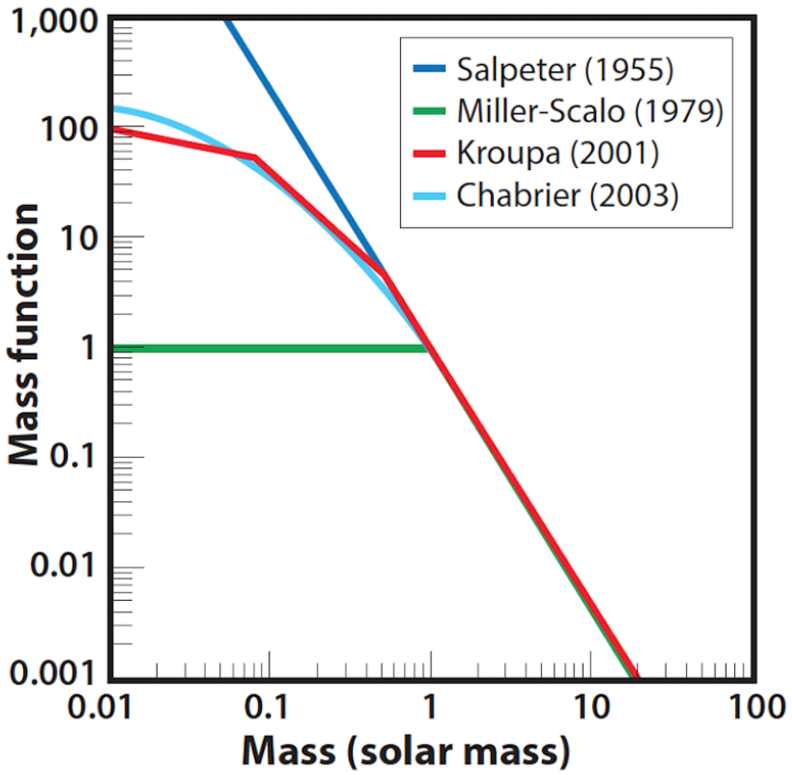


Figure 1.9: Plot of various IMFs. The dark blue line represents the Salpeter unimodal IMF (Salpeter, 1955). The green line represents a bimodal IMF introduced by Scalo (1986). The red line represents the Kroupa IMF (Kroupa, 2001), and the light blue line shows the Chabrier IMF for individual stars (Chabrier, 2003). Image taken from https://astronomy.com/sitefiles/resources/image.aspx?item=%7B292FC98F-E73A-4FE5-A846-621F48E388BE%7D.

1.6.2 Stellar libraries

A stellar library is a collection of spectra of individual stars. Stellar libraries can be empirical, theoretical or a combination of both. Here we present the stellar libraries that will be used in this work for studying the stellar populations of our BCG sample. The libraries mentioned here work with computational software such as FIREFLY (Wilkinson et al., 2017), more description on the fitting routine FIREFLY will be given in Chapter 4 of this work.

The MaStar library

The MaNGA Stellar Library (MaStar) is a large, well-calibrated, high-quality empirical library covering the wavelength range 3622–10354 Å (Yan et al., 2019; Maraston et al., 2020). The library is comprised of $>$ 10000 stellar spectra, the spectra were obtained with the same instrument as used by MaNGA at the Apache Point Observatory (Maraston et al., 2020). In comparison with previous stellar libraries MaStar has the widest wavelength

coverage and largest sample of empirical stellar spectra.

The MILES library

The Medium-resolution INT Library of Empirical Spectra (MILES) is a stellar library that was introduced by Sánchez-Blázquez et al. (2006), consisting of 985 synthetic stellar spectra. The spectra were observed by the 2.5m Isaac Newton Telescope (INT) in the wavelength range of 3525 - 7500 Å at 2.3 Å (FWHM) spectral resolution. The library covers most evolutionary stages based upon what can be expected to exist in our Galaxy at all metallicities down to [Fe/H] $\sim$ -2.0 (Maraston & Strömbäck, 2011). Sánchez-Blázquez et al. (2006) noted the spectral resolution, spectral type coverage, flux calibration accuracy and number of stars used in the library represents a substantial improvement over previous libraries used in population synthesis models.

The STELIB library

STELIB is a spectroscopic stellar library that was introduced by Le Borgne et al. (2003), consisting of an homogeneous library of 249 stellar spectra in the wavelength range 3200 - 9500 Å, with a spectral resolution of $\lesssim$ 3 Å. The data were obtained during two runs, one at the 1m Jacobus Kaptein Telescope (JKT), Roque de los Muchachos Observatory, La Palma, Canary Islands, Spain, and a second one at the 2.3m telescope of the Australian National University at Siding Spring Observatory (SSO), Australia, (Le Borgne et al., 2003). This library includes stars of various spectral types and luminosity classes, spanning a relatively wide range in metallicity ranging from well below solar ([Fe/H] from -2 to -1) to above solar ([Fe/H] $>$ 0)(Le Borgne et al., 2003).

The ELODIE library

First introduced by Prugniel & Soubiran (2001) the ELODIE library is an empirical stellar library that was originally a collection of 908 high-resolution stellar spectra. The spectra was observed with the ELODIE spectrograph of the 1.93m telescope at the Haute-Provence Observatory in the wavelength range 4100 - 6800 Å. However, the latest version, ELODIE v3.1 (Prugniel et al., 2007), contains about twice as many spectra as the original library and a slightly increased wavelength range (Maraston & Strömbäck, 2011). The new version of the library is a collection of 1959 spectra in the wavelength range of 3900 - 6800 Å. Maraston & Strömbäck (2011) lists the spectral resolution of the library as 0.55 Å.

The MARCS library

The MARCS library contains high-resolution theoretical spectra and covers a large spectral range from 1300 Å to 20 μm (Gustafsson et al., 2008). The MARCS model atmospheres

(Gustafsson et al., 1975, 2003, 2008) have been continuously improved since the mid-1970s. These stellar atmospheres have effective temperatures ranging between 2500 - 8000 K (at solar metallicity), surface gravities between -1.0 and 5.5 and metallicities between -5.0 and +1.0 (Gustafsson et al., 2008; Beifiori et al., 2011).

1.7 Stellar Kinematics

The first measurements of stellar kinematics of galaxies were attempted by Slipher (1913), using stellar absorption line spectroscopy he showed that galaxies, on average, all recess from us with large radial velocities. This work was extended on by Hubble (1929) and discovered the expansion of the Universe. Over the next few decades, using absorption lines was mainly limited to probing distances to successively more distant galaxies. Studies of velocity dispersion did not begin until the 1950s, and it was not until the 1970s that stellar absorption lines became a practical tool for studying the internal kinematics of galaxies. Several methods have since been developed that use the spectra of individual stars as templates for comparing the spectra of galaxies (Simkin, 1974; Sargent et al., 1977). In this way, kinematic properties such as the velocity dispersion and stellar radial velocity can be derived, see Figure 1.10. Initially it was only the brightest objects such as Elliptical galaxies and the bulges of Spiral that were observed (Illingworth, 1977).

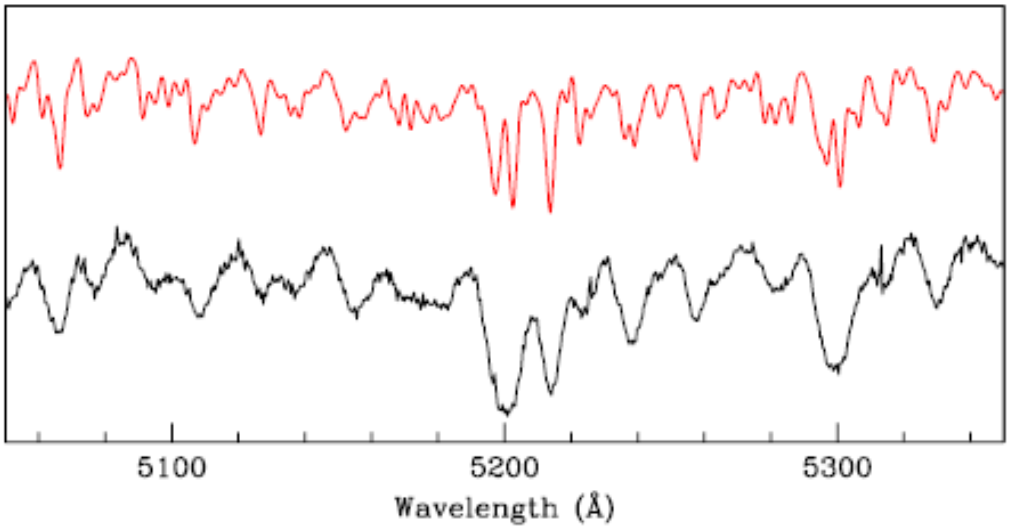


Figure 1.10: An example of a galaxy spectrum (black line) and a K0 stellar template (red line) shifted to the radial velocity of the galaxy. The main difference between the two spectra is the width on the absorption lines. This difference is a measure of the velocity dispersion. Image taken from Gerssen (2000)

Most of the currently available results are derived from using longslit spectroscopy and as a result only provide one-dimensional information. Over last few years, the integral

field spectroscopy (IFS) technique has been utilised by many surveys such as: SAURON (Spectroscopic Areal Unit for Research on Optical Nebulae; Bacon et al., 2001; de Zeeuw et al., 2002; Emsellem et al., 2004), ATLAS^{3D} (Cappellari et al., 2011), SAMI (Sydney-Australian-Astronomical-Observatory Multi-object Integral-Field Spectrograph; Croom et al., 2012), CALIFA (Calar Alto Legacy Integral Field Array survey; Sánchez et al., 2012), VENGA (Visible Integral-field Replicable Unit Spectrograph – Prototype Exploration of Nearby Galaxies; Blanc et al., 2013) and MaNGA (Mapping Nearby Galaxies at Apache Point Observatory; Bundy et al., 2014). These surveys are dedicated to obtaining two-dimensional kinematics for large enough samples of galaxies to enable statistical studies of galaxy populations as a whole (Gerssen, 2000; Cannarozzo, 2021), the availability of such two-dimensional kinematic information avoids many of the uncertainties that can arise when using only one-dimensional information.

1.7.1 Velocity profiles

The amount by which the template spectrum must be broadened to fit the galactic spectrum is known as the line-of-sight velocity distribution (LOSVD) and can be approximated by a Gaussian function. The basic idea is that the observed galactic spectrum can be approximated by a stellar spectrum convolved with the velocity distribution of the stars along the line-of-sight (Gerssen, 2000),

$$\text{Galaxy} = \text{Template} \otimes \text{LOSVD},$$

A line profiles are measured in the wavelength space or the frequency space, but our understanding of the Doppler effect allows us to transform this to a velocity space. In Figure 1.11 we show an example emission line profile. The integrated LOSVD is equal to the total amplitude and provides a measure of the random distribution of velocities of the individual stars that broaden the spectral lines (absorption lines) relative to those of an individual star. The mean of the LOSVD is the measurement of the typical line-of-sight velocity of the stars. Whereas, the width of the LOSVD, often referred to as the velocity dispersion, provides a measurement to the dispersion of the velocities of individual stars in a galaxy about their mean value. By measuring these emission line profiles across the entire galaxy, we can gain an important understanding about the kinematics of stars within the galaxy.

The early studies on stellar velocity dispersion by Minkowski (1962) used out of focus spectra of template stars to estimate the amount of broadening. The introduction of supercomputers and the availability of fast Fourier transform algorithms has made it possible to perform deconvolution numerically. Today, deconvolution techniques are more sophisticated (Gerssen, 2000), but the analysis of absorption line data remains unchanged.

The methods developed to calculate velocity profiles can be mainly classified as either parametric or non-parametric. Parametric methods have the advantage of having robust

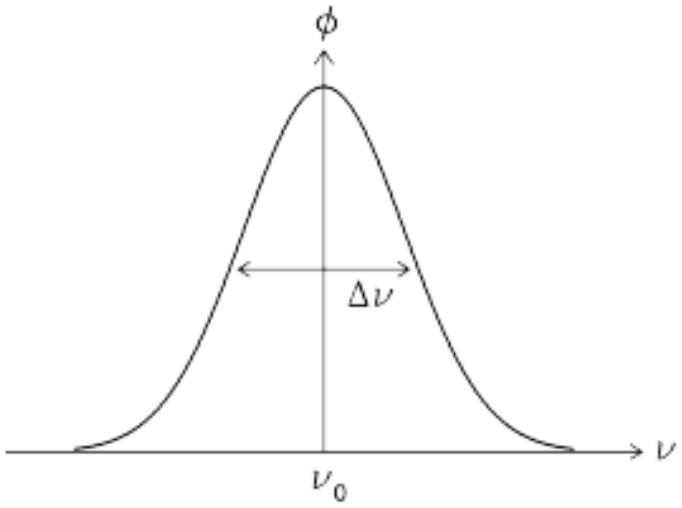


Figure 1.11: A mock emission line profile that measures the luminosity of light (ϕ) as a function of frequency (ν). Image taken from Varidel (2021).

and well-defined errors (Gerssen, 2000). Moreover, parametric methods assume a specific shape for the velocity profile, usually a Gaussian. Starting with the work of Gerhard (1993) and Van Der Marel & Franx (1993) several methods have been developed to extract high-order Gaussian moments from the observed spectra, such as the kurtosis. On the other hand, the non-parametric methods place no restriction on the shape of the velocity profile (Rix & White, 1992). A drawback of these methods is that their error analysis is generally difficult to understand. Kuijken & Merrifield (1993) introduced an unresolved Gaussian Decomposition algorithm, which is a non-parametric method that has complete freedom of the velocity profile shape and also provides a good handle on the uncertainties associated with the derived shape (Gerssen, 2000).

1.7.2 Measuring Stellar Kinematics From Galaxy Spectra

A line profile (introduced in Section 1.7.1) can be approximated as a Gaussian profile $\mathcal{L}$ with the line strength γ, average rotational velocity (V) and the velocity dispersion (σ) as free parameters (Van Der Marel & Franx, 1993). The profile is then given as:

$$\mathcal{L}(v) \;=\; \gamma \frac{\alpha(w)}{\sigma} \tag{1.7.1}$$

where $w \;=\; (v - V)/\alpha$. And the standard Gaussian is given by:

$$\alpha(x) \;=\; \frac{1}{\sqrt{2\pi}} e^{-(1/2)x^2} \tag{1.7.2}$$

To determine the deviations from the Gaussian line profile, Van Der Marel & Franx (1993)

generalised the parameters as a sum of orthogonal functions, namely the Hermite polynomials. These polynomials can be expressed as (Gerhard, 1993):

$$H_n(x) \;=\; (-1)^n e^{x^2}\;\frac{d^n}{dx^n}\;e^{-x^2} \tag{1.7.3}$$

and have orthogonality relation given as:

$$\int_{-\infty}^{\infty} H_j(x)H_k(x)\alpha^2(x)dx \;=\; \frac{\delta_{jk}}{2\sqrt{\pi}}$$

where δ_{jk} is the Kronecker-delta function.

$$\delta_{jk} \;=\; \begin{cases} 0 & \text{if} \quad j \neq k \\ 1 & \text{if} \quad j = k \end{cases}$$

The first few Hermite polynomials are given as:

$$\begin{aligned} H_0(x) \;=\; 1,\; H_1(x) \;=\; 2x,\; H_2(x) \;=\; 4x^2 - 2, \\ H_3(x) \;=\; 8x^3 - 12x,\; H_4(x) \;=\; 16x^4 - 48x^2 + 12. \end{aligned} \tag{1.7.4}$$

The LOSVD of a given galaxy can be described by a Gaussian function. However, since the LOSVD is typically not symmetric and it is better reproduced by a non-symmetric function. The solution to this is provided by a Gaussian and a set of Hermite polynomials (introduced above), commonly referred to as a Gauss-Hermite series (Van Der Marel & Franx, 1993; Gerhard, 1993). This series can be expressed as:

$$\mathcal{L}(v) \;=\; \left[\frac{e^{-(1/2)x^2}}{\sigma\sqrt{2\pi}}\right]\left\{1 \;+\; \sum_{m=3}^{N} h_m H_m(x)\right\} \tag{1.7.5}$$

where $x \;=\; (v - V)/\sigma$, h_m are the Gauss-Hermite moments and H_m are the Hermite polynomials. This function allows us to perform a $N \;+\; 1$ parameter fit to the LOSVD to simultaneously determine the values of V, σ, γ, and the Gauss-Hermite moments for the galaxy. In most cases, and as is on this dissertation only the h_3 and h_4 Gauss-Hermite moments are added. The h_3 term models the deviation of the Gaussian from a symmetric form and is called the skewness, the h_4 models the pointedness of the Gaussians peak and is called the kurtosis.

In order to determine V, σ, h_3 and h_4 of a galaxy, one simply needs to fit the line profiles of the absorption line spectra of the galaxy. The spectrum of the galaxy can be obtained by performing an optical spectroscopic study on the galaxy. Conventionally, all the absorption lines of the entire spectrum can be fitted simultaneously with computer software such as the Groningen Image Processing System (GIPSY, Van der Hulst et al.,

1992), the Penalised Pixel Fitting Method (pPXF, Cappellari & Emsellem, 2004) and the Stellar Content and Kinematics via Maximum likelihood A Posteriori (STECKMAP, Ocvirk et al., 2006). In this study we adopt the method of Cappellari & Emsellem (2004), this procedure is discussed in great detail in Chapter 3 of this work.

1.8 Outline of this work

This dissertation focuses on BCGs at intermediate redshifts ($0.3 < z < 0.8$) to provide more observational insights on the BCG formation and evolution over a 3.4 billion years period. We are particularly interested in the kinematics and star formation histories of these galaxies over this 3.4 Gyr time period. BCGs have been modelled dynamically and imaged extensively. However, their formation mechanisms are still unknown. Studying BCG properties with redshift is important in order to understand their formation and evolutionary histories, as the details are not yet clear (from the different theories). The relative age of galaxies at different redshifts can be used to infer the Hubble parameter and put constraints on cosmological models. If we assume that BCGs are passively evolving systems, their ages can, potentially, be used to constrain the expansion of the Universe (see Carson & Nichol, 2010; Ratsimbazafy et al., 2017, and references therein).

The general structure of this dissertation will be as follows:

- Chapter 2 will describe the cluster sample that is used throughout this dissertation along with the parent cluster catalogue from which the BCGs were obtained. It also gives a detailed description on how the BCGs are selected. It will also look at the data reduction including the methods and software used to accomplish it.
- Chapter 3 presents the data analysis and explores how the pPXF spectral fitting code (Cappellari & Emsellem, 2004; Cappellari, 2017) can be used to derive stellar kinematics for the BCG population. It will also look at the issues encountered and what could be done to improve the quality and reliability of the results. This chapter will also describe concept of stacking, and the specific applications to our observed spectra through the use of the computational program *specstack* (Thomas, 2019).
- Chapter 4 presents the analysis of the BCG stellar populations using full-spectrum fitting. The results of this analysis including the stellar ages and metallicities were calculated with the spectral fitting code FIREFLY (Wilkinson et al., 2017; Goddard et al., 2017; Comparat et al., 2017). We will also discuss the results of our analysis and we also show how the BCG ages we determine at different redshifts can be applied for further studies (i.e constraining cosmological models).
- Chapter 5 presents the summary of this work along with prospects for future work.
- Appendix A contains the DES imaging referred to in Chapter 2. Appendix B contains the tables referred to in Chapter 3.

Chapter 2

Data acquisition and reduction

> "Those who believe, and whose hearts find satisfaction in the remembrance of Allah. For without doubt in the remembrance of Allah do hearts find satisfaction."
>
> *Surah Ar-Ra'd*, Qur'an 13:28

The scientific analysis and results chapters found in this dissertation are, to a certain extent, based on the cluster sample that is introduced in this chapter. In Section 2.1 we start off by describing the composition of the cluster sample which is taken from the Advanced Atacama Cosmology SZ cluster survey. We then move on to Section 2.2, where we give a detailed description of the observations[1] performed on the cluster sample using the Southern African Large Telescope. Section 2.3 discusses the data reduction process, under this Section we cover the initial data reduction process and also the use of the RSSMOSPipeline for latter reduction stages. In Section 2.4 we give a detailed description of the BCG selection process. We also discuss some of the challenges we encountered during this process. We end the chapter by providing a Table containing all the cluster candidates that are used for analysis in this study.

2.1 The cluster sample

The Advanced Atacama Cosmology Telescope (AdvACT) SZ cluster survey, is a sample of > 4000 optically confirmed clusters with cluster masses derived from the Atacama Cosmology Telescope Polarization experiment (ACTPol) and redshifts allocated by matching with different optical catalogues (see Hilton et al., 2018, 2021, for more details). The obser-

[1] Matt Hilton served as the investigator of the observations.

vations were made on a 6-m telescope, located at the Llano de Chajnantor Observatory in the Atacama Desert in the north of Chile. This telescope is equipped with three detector arrays containing dichroic, dual polarization horn-coupled Transition Edge Sensor (TES) bolometers, observing at 98, 150, and 220 GHz, with 27 and 39 GHz channels added in the 2020 season (Henderson et al., 2016; Hilton et al., 2021). The AdvACT cluster survey uses data from only the 98 and 150 GHz channels, which have approximate beam Full Width Half Maximum (FWHM) of $2.20'$ and $1.40'$, respectively (Hilton et al., 2021). The SZ cluster survey covers an area of roughly 13 168 deg^2, covering most of the Southern extragalatic sky (see Figure 2.1). A detailed discussion of the full cluster candidate detection, confirmation and redshift assignments of AdvACT will not be given here (see Hilton et al., 2018, 2021, for more detail).

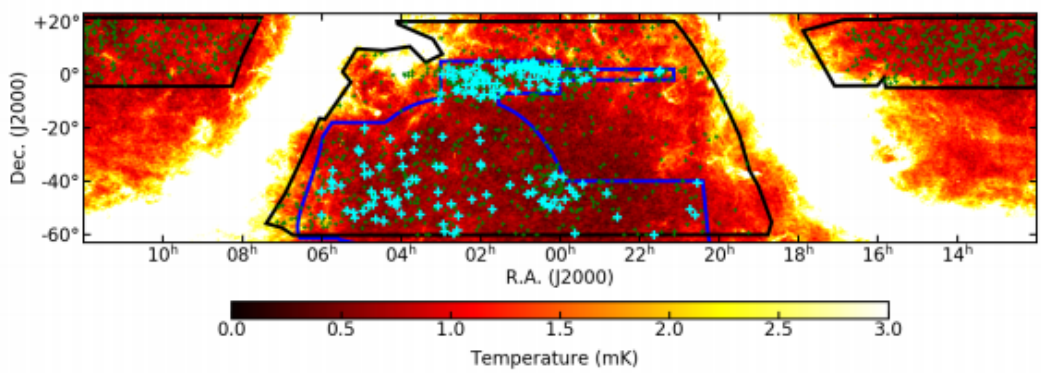


Figure 2.1: The preliminary AdvACT cluster sample plotted on the Planck 353 GHz map, which highlights dust emission. The black outline gives the footprint of the AdvACT cluster search ($\approx$ 14 000 deg^2). The green crosses mark all objects detected with S/N $>$ 4 by ACT ($>$ 1500 clusters), while the cyan crosses mark the clusters that meet the criteria for the SALT target pool (S/N $> 5\sigma$; $0.3 < z < 0.8$; and within the Dark Energy Survey (DES; Perez et al., 2018) footprint, which is marked in blue). Image taken from https://astro.ukzn.ac.za/~beams/wiki/pmwiki.php?n=Resources.Proposals.

The data used in this study utilises a large sample of *Brightest cluster galaxies Evolution with AdvACT, MeerKAT and SALT* (BEAMS)[2] optically selected clusters, that have a well-defined selection function that is relatively independent of cluster mass across a wide range of redshifts. The wide sky distribution of the BEAMS clusters makes it a sample that is well suited for follow-up studies with the Southern African Large Telescope (SALT). SZ cluster surveys can detect clusters at any redshift, and to optimise our study for SALT a number of cuts were made to the cluster sample detected by AdvACT. The following selection criteria was used to select a sample of clusters to be observed on SALT:

1. A S/N $> 5\sigma$ cut was made in the AdvACT SZ detection significance. This ensures that the cluster sample is clean, and robust to any future changes in the AdvACT cluster catalog (which may cause lower S/N clusters to drop out of the sample);

[2]More information on BEAMS can be found here - https://acru.ukzn.ac.za/~beams/

2. restricted the redshift range to $0.3 < z < 0.8$. This is required to ensure that the [OIII] 5007 Å line remains within the wavelength coverage of the Robert Stobie Spectrograph (RSS);

3. the clusters are required to be within the footprint of the DES (shown as the blue outline in Figure 2.1). This ensures excellent *griz* photometry and imaging for all targets.

Following these cuts, we arrive at a pool of 186 clusters that we may draw from (marked with the cyan crosses on Figure 2.1); the number of targets that meet these criteria in the pool will increase as the AdvACT survey becomes deeper. For this study a total of 150 BCGs were targeted for SALT observations as part of the BEAMS program. Figure 2.2 shows the redshift distribution of our cluster sample, the sample is comprised of both the spectroscopic and photometric redshifts. Clusters that are found to have a spectroscopic redshift represent about 85% of all clusters used in our sample, whereas the other 15% of the sample is made up of clusters that have a photometric redshift.

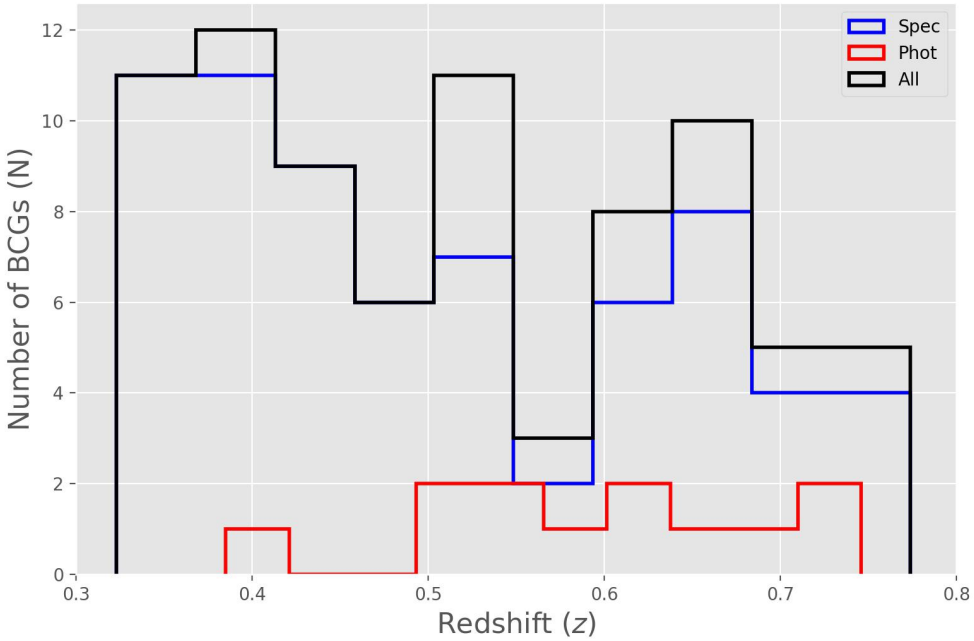


Figure 2.2: The redshift distribution of all the clusters that will be used in our analysis. The **"blue step"** represents clusters that have a spectroscopic redshift. And the **"red step"** represents clusters found to have a photometric redshift. The spectroscopic clusters have a z range between 0.323 to 0.774, and a mean value of 0.509, whereas the photometric clusters have a z range between 0.385 to 0.746 with a mean value of 0.589. The **"black step"** represents the overall z of our sample varies from 0.323 to 0.774 with an average value of $z = 0.521$.

2.2 SALT Observations

2.2.1 Telescope

The Southern African Large Telescope (SALT, shown here in Figure 2.3) is a 10-m class telescope located at the South African Astronomical Observatory (SAAO), in Sutherland, South Africa (Buckley et al., 2006; Böttcher et al., 2017). The telescope is primarily designed for optical and infrared spectroscopy and one of its main instruments is the Robert Stobie Spectrograph (RSS, shown here in Figure 2.4), located at the telescope's prime focus. The RSS is capable of performing spectroscopy in various modes, including long-slit, multi-object slit (MOS), polarimetry, and Fabry-Pérot. The telescope is sensitive to wavelengths ranging from ~ 3200 Å to ≥ 9000 Å (see Böttcher et al., 2017, and references therein).



Figure 2.3: The Southern African Large Telescope (SALT) located in Sutherland, South Africa. Image taken from https://www.saao.ac.za/explore/our-telescopes/salt/.

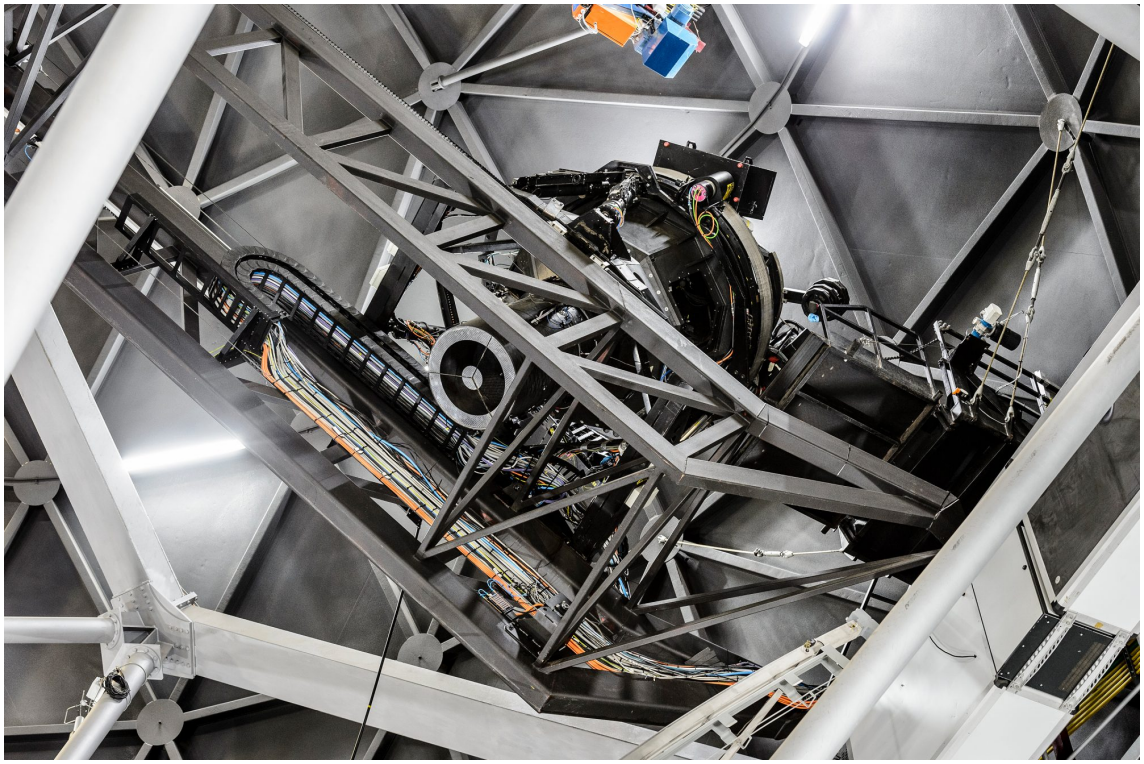


Figure 2.4: The RSS is the primary instrument on SALT. Image taken from https://origins.wisc.edu/chapter-1-the-universe/.

2.2.2 Observations

Our observations were conducted in the framework of a large science SALT program that is executing a spectroscopic survey of BCGs in massive clusters (2019-1-LSP-001, PI: M. Hilton), to obtain medium resolution spectra of approximately 150 BCGs. This program aims to quantify the mode, strength, and evolution of AGN feedback processes and star formation activity in the centres of clusters. These observations began in May 2019. Due to the redshift range of our cluster sample ($0.3 < z < 0.8$), the observation of the 150 clusters required the use of the RSS longslit spectroscopy with spectral resolution ≈ 3 Å (equivalent to ≈ 100 km.s^{-1} in the rest-frame, needed for measuring stellar velocity dispersion/stellar population studies) and rest-frame wavelength coverage between 3800 - 5100 Å. This meant that we had to use the PG1300 grating in combination with a $1.25''$ slit for BCGs that have $z < 0.65$. And for BCGs that have $z > 0.65$ (the highest z bin), we used the PG0900 grating to ensure that we covered the needed wavelength range. In both cases the typical rest-frame wavelength resolution is similar to that used in Gemini studies of BCG spectra by Loubser et al. (2016).

2.3 Data reduction

The data analyzed in this study can be obtained from the BEAMS project website[3] with permission from the PI: Matt Hilton. The initial data reduction was carried out by the PI using PySALT[4] (Crawford et al., 2010), a suite of PyRAF tools designed for the reduction and analysis of data from the RSS instrument mounted on SALT. The PySALT package mainly performs tasks such as preparing image headers, applying CCD amplifier gain and cross-talk corrections, and bias subtraction (see Hilton et al., 2018, for a more detailed discussion for the initial data processing steps). Following the initial data processing with PySALT, we then passed the data products onto the RSSMOSPipeline[5] for further reduction and the extraction of one dimensional spectra. The RSSMOSPipeline is discussed in great detail in the following Section.

2.3.1 RSSMOSPipeline

The RSSMOSPipeline is a fully automated pipeline designed for processing astronomical spectra. It was created to perform various tasks such as flat-field correction, wavelength calibration, and extraction of one-dimensional spectra (Hilton et al., 2018). The pipeline was originally written to process MOS spectra, but it has since been adapted to also reduce long-slit spectra. In long-slit mode, the pipeline searches for traces of objects and creates "pseudo slits" around them (Hilton et al., 2018) before processing the data in the same way as it does for MOS mode data. The pipeline can be used in two different ways: you can either use it to process data for a single object or multiple objects.

1. Single object reduction:

1. Download and unpack the archive containing your SALT data. This pipeline will operate on the contents of the "product" directory.

2. Run the code, e.g., "rss_mos_reducer product reducedDir maskName", here maskName is the combination of the OBJECT_MASKID from the corresponding FITS header keywords. So, for example if your data for an object named J0014.9-0057 were taken with a mask called PL0125N001 and is within the "product" directory, you would then run the pipeline with:
"rss_mos_reducer product reduced J0014.9-0057_PL0125N001"

3. The processed data from the mask will be found under the "reduced" folder.

[3] https://astro.ukzn.ac.za/~beams/
[4] https://github.com/saltastro/pysalt
[5] https://github.com/mattyowl/RSSMOSPipeline

2. Multiple object reduction:

1. Step 1 is the same as above.
2. To process the data for multiple objects, you run the code:
   "rss_mos_reducer product reduced all"
   this asks the pipeline to process data for all the masks it can find (in this case, under the product directory).
3. The processed data from each mask will be found in its own subdirectory under the "reduced" folder in the above example.

In both these processes, when the pipeline has finished processing these masks, the processed data at various stages of the data reduction are found under the "reducedData" directory. In this study we utilised the multiple object reduction process, this is due to the data (longslit data) having multiple objects in the slit. The pipeline uses two methods to extract the spectra:

i. Individual 1D spectra are extracted from each science frame and then stacked*. This might be desirable if object traces shift from frame-to-frame. These are placed under "reducedDir/OBJECT_MASKID/1DSpec_extractAndStack/"

ii. The 2D spectra are stacked and then a 1D spectrum is extracted. These are placed under the "reducedDir/OBJECT_MASKID/1DSpec_2DSpec_stackAndExtract/". This directory also has the stacked 2D spectra.

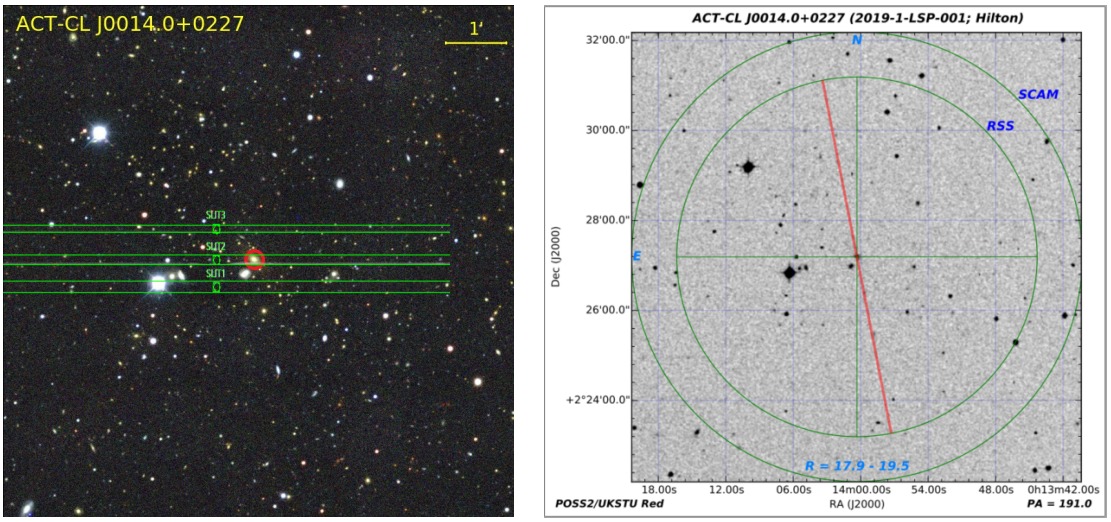
* Please note that the "stacked spectra" produced by the pipeline is not the same as the one that will be discussed in Section 3.2.1, where we stack spectra of the different BCGs.

2.4 Finding the BCG slit

The long-slit was positioned to observe more than one galaxy, and we needed to identify which of the extracted 1D spectra contained the BCG. The identification of the BCG was made via a visual inspection of the DES[6] imaging with the aid of finder charts and region files. In Figure 2.5 given as an example, the long-slit data contains spectra for three galaxies. The BCG is located at the center of the finders chart where the green vertical and horizontal lines meet, overlaying the region file on the DES imaging allowed us to approximate the slit that had the BCG. The BCG (marked with the red circle) given in this example corresponds to the 1D spectra marked "slit 2". In Figure 2.6, the long-slit data contains spectra for six objects. In this case the BCG was found to correspond with the spectrum marked "slit 5". The selection of the BCGs was primarily based on their

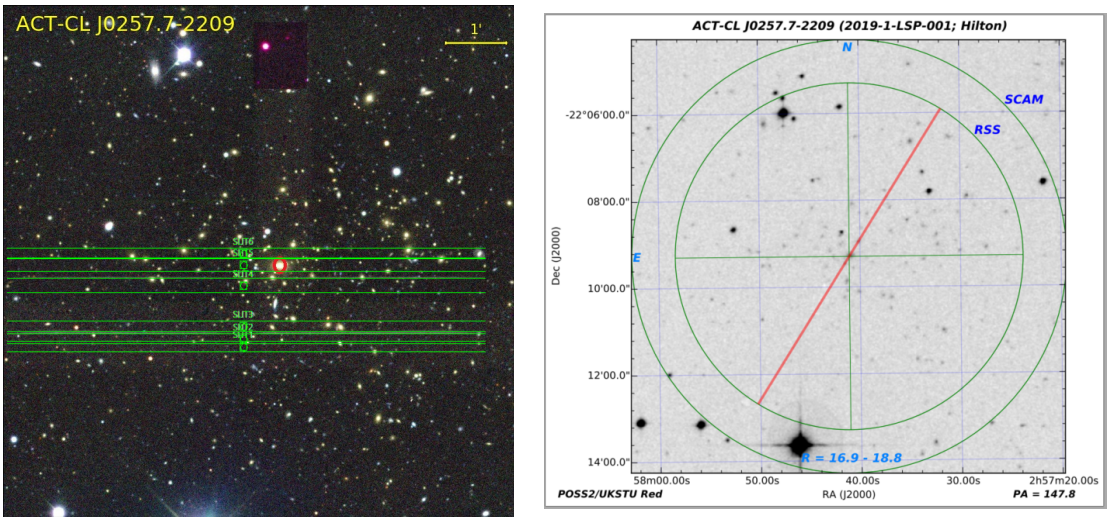
[6]The complete list of DES imaging used in this study can be found in Appendix A.

morphology and central location in the cluster. As such, the BCG need not necessarily be photometrically the brightest galaxy as has been conventionally done (e.g. Lauer et al., 2014).



(a) (b)

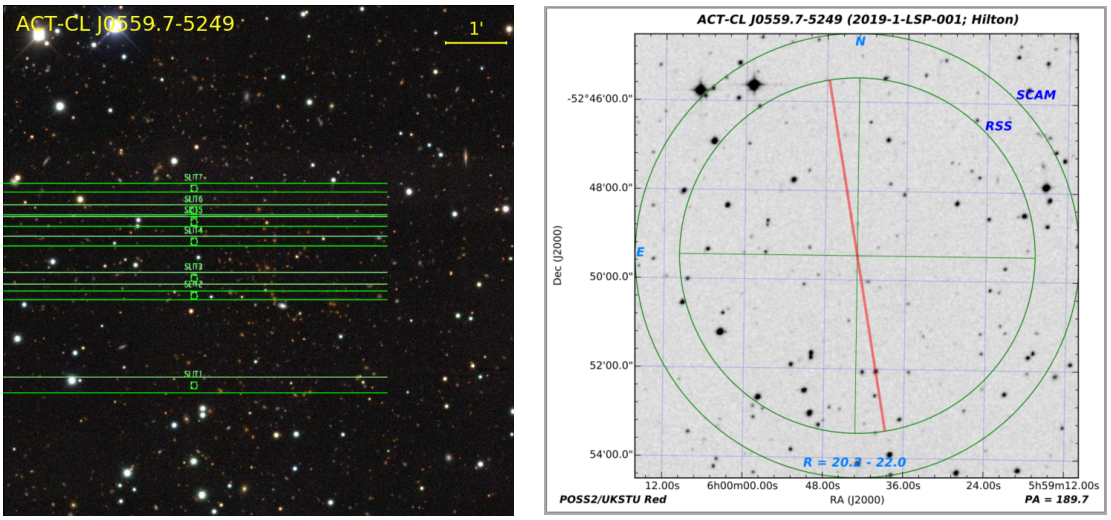
Figure 2.5: (a) DES cluster image of ACT-CL J0014.0+0227 ($z = 0.337$). The BCG is circled in red. (b) SALT finder chart of J0014.0+0227, used in the identification process of the BCG. The green slit lines (in (a) not shown to scale) is the region file of J0014.0+0227, used in the identification process of the slit in which the BCG is located. The BCG is found in SLIT 2.



(a) (b)

Figure 2.6: (a) DES cluster image of ACT-CL J0257.7-2209 ($z = 0.499$). The BCG is circled in red. (b) SALT finder chart of J0257.7-2209, used in the identification process of the BCG. The green slit lines (in (a) not shown to scale) is the region file of ACT-CL J0257.7-2209, used in the identification process of the slit in which the BCG is located. The BCG is located in SLIT 5.

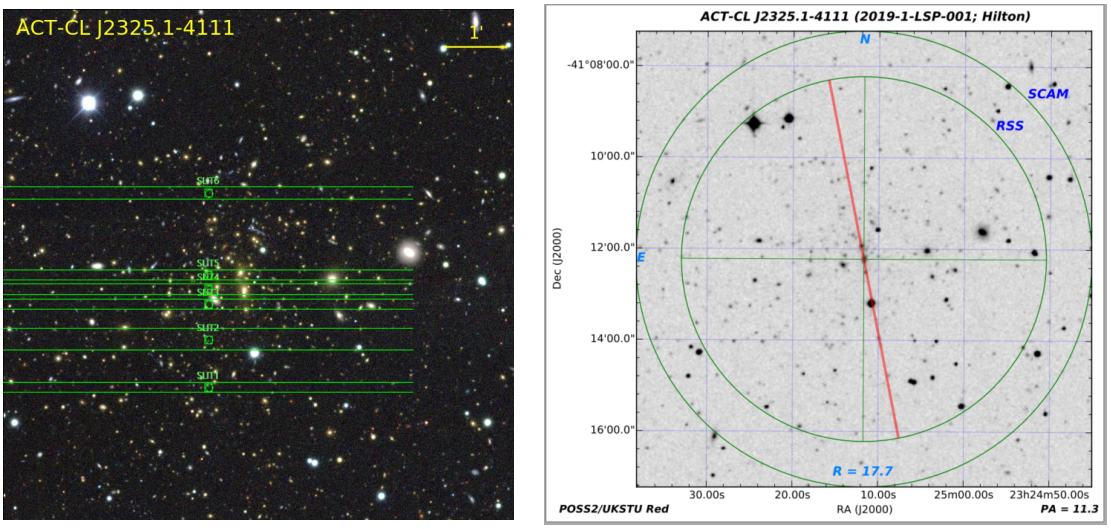
This process of identification was performed for all clusters in this study. For most of our clusters, the selection of the BCG slit was obvious, but when the galaxy choice (slit number) was uncertain, the candidate that was best aligned with the center of the finder chart in the DES imaging was selected. However, there were cases where the finder chart and DES imaging did not correlate (this was mostly due to the finder charts having fainter objects), such an occurrence can be seen on Figure 2.7. In these cases, the "slit" with the BCG was approximated based on the overlaid region file on the DES imaging alone. In total we found 10 ($\sim 12\%$ of the total sample) such cases, these clusters are marked in red in Table 2.1. These galaxies are also included as part of the analysis undertaken in this dissertation.



(a) (b)

Figure 2.7: This is an example where the BCG is not clearly visible on the finder chart. (a) DES cluster image of ACT-CL J0559.7-5249 ($z = 0.611$). (b) SALT finder chart of J0559.7-5249, used in the identification process of the BCG. The green slit lines (in (a) not shown to scale) is the region file of ACT-CL J0559.7-5249, used in the identification process of the slit in which the BCG is located. The BCG is in this case was approximated to be located in SLIT 2.

Green et al. (2017) noted that, although it is a time consuming process, visual identification is probably still the most reliable method of identifying BCGs in clusters, as it helps minimise issues with projection. Another advantage of visually identifying BCGs is that it helps to potentially identify merging central galaxies, such possible event can be observed from Figure 2.8. In Figure 2.8a, we can see what appears to be a merging event, between two member galaxies of the cluster. The list of clusters and the location of BCGs, their redshifts and redshift type used in this study are summarised in Table 2.1.



(a) (b)

Figure 2.8: (a) DES cluster image of ACT-CL J2325.1-4111 ($z = 0.362$). (b) SALT finder chart of J2325.1-4111, used in the identification process of the BCG. The green slit lines (in (a) not shown to scale) is the region file of ACT-CL J2325.1-4111, used in the identification process of the slit in which the BCG is located. The BCG is located in SLIT 4.

$0.3 < z < 0.4$						
Name	R.A. (deg)	Decl. (deg)	z Source	z	z Type	Position
(1)	(2)	(3)	(4)	(5)	(6)	(7)
ACT–CL J0257.7-2209	44.43276418075	-22.160359963	SPTECS	0.323	Spec	SLIT 5
ACT–CL J0405.9-4915	61.493307	-49.25582133	SALT	0.325	Spec	SLIT 3
ACT-CL J0014.0+0227	3.502633772	2.452013035	SDSS	0.335	Spec	SLIT 2
ACT-CL J0127.2+0020	21.81862977	0.3473381999	S16	0.337	Spec	SLIT 1
ACT–CL J2031.8-4037	307.9706837	-40.6186504	SPTSZ	0.344	Spec	SLIT 3
ACT–CL J0040.8-4408	10.20584859	-44.13367336	SPTSZ	0.349	Spec	SLIT 4
ACT–CL J2325.1-4111	351.2944561	-41.19841058	SPTSZ	0.355	Spec	SLIT 5
ACT-CL J0044.4+0150	11.11632092	1.835349671	SDSS	0.358	Spec	SLIT 4
ACT-CL J0008.1+0201	2.046719373	2.020848324	SDSS	0.364	Spec	SLIT 2
ACT-CL J0219.9+0130	34.98013351	1.501869584	SALT	0.364	Spec	SLIT 4
ACT-CL J0028.3+0317	7.084700771	3.284592172	SDSS	0.365	Spec	SLIT 1
ACT–CL J0154.5-0039	28.63188107	-65.0787357	SDSS	0.369	Spec	SLIT 1
ACT-CL J0024.6+0001	6.154076742	0.02912374497	SDSS	0.373	Spec	SLIT 1
ACT–CL J0239.8-0134	39.95910019	-1.569957603	S16	0.377	Spec	SLIT 2
ACT-CL J0034.5+0225	8.631972037	2.41857106	SALT	0.382	Spec	SLIT 4
ACT–CL J0135.8-2044	23.97342003	-20.73904798	RMDESY3	0.385	Phot	SLIT 3
ACT-CL J2307.6+0130	346.919224	1.516555892	SDSS	0.386	Spec	SLIT 4
ACT–CL J0024.0-0444	6.024763221	-4.741720347	SALT	0.386	Spec	SLIT 2
ACT-CL J2128.4+0136	322.1073726	1.606152007	S16	0.392	Spec	SLIT 2
ACT–CL J0416.1-2404	64.04181493	24.07454196	SPTECS	0.395	Spec	SLIT 2
ACT–CL J0159.8-0849	29.95917689	-8.830646336	SDSS	0.396	Spec	SLIT 1
$0.4 \leq z < 0.5$						
ACT–CL J0013.2–4906	3.323826863	-49.1117207	SPTSZ	0.402	Spec	SLIT 1
ACT-CL J0256.6+0006	44.13320347	0.104227181	S16	0.407	Spec	SLIT 3
ACT–CL J0411.2–4819	62.80684134	-48.32252503	SPTSZ	0.418	Spec	SLIT 2

ACT–CL J0159.0–3413	29.75117444	-34.22436094	SPTECS	0.420	Spec	SLIT 2
ACT–CL J0438.3–5419	69.5750404	-54.32055217	S16	0.434	Spec	SLIT 1
ACT–CL J0358.9–2955	59.72696185	-29.93020283	SPTECS	0.434	Spec	SLIT 2
ACT–CL J0154.4–0321	28.61830018	-3.358369973	SDSS	0.441	Spec	SLIT 2
ACT–CL J2233.3–5338	338.3294013	-53.64644674	SPTSZ	0.443	Spec	SLIT 2
ACT–CL J0125.7–0634	21.42888265	-6.568795869	SDSS	0.450	Spec	SLIT 2
ACT–CL J0140.0–0554	25.00682015	-5.915780905	SALT	0.450	Spec	SLIT 4
ACT–CL J2116.1–0226	319.0266337	-2.444540183	SDSS	0.458	Spec	SLIT 3
ACT–CL J0008.5–0519	2.136488145	-5.324074043	SALT	0.461	Spec	SLIT 2
ACT–CL J0019.0–4051	4.965897215	-40.86497574	SALT	0.469	Spec	SLIT 1
ACT–CL J0029.1–3708	7.291688583	-37.13642071	SALT	0.473	Spec	SLIT 1
ACT-CL J2332.8+0109	353.2163469	1.166042632	SDSS	0.483	Spec	SLIT 1
ACT–CL J0025.8–0419	6.473018574	-4.323882853	SDSS	0.492	Spec	SLIT 2
$0.5 \leq z < 0.6$						
ACT–CL J0005.7–3751	1.440075832	-37.85932487	SALT	0.503	Spec	SLIT 1
ACT–CL J0249.0–0818	42.26665137	-8.312314415	RMDESY3	0.507	Phot	SLIT 1
ACT-CL J0007.3+0341	1.840763786	3.685904014	SDSS	0.508	Spec	SLIT 1
ACT–CL J0014.9–4036	4.75931622	40.60421583	RMDESY3	0.514	Phot	SLIT 2
ACT–CL J2248.7–4431	342.1929364	-44.53040076	SPTSZ	0.519	Spec	SLIT 3
ACT-CL J0108.0+0251	17.01099649	2.857117067	RMDESY3	0.532	Phot	SLIT 1
ACT–CL J0014.9–0057	3.726310569	-0.950387441	S16	0.534	Spec	SLIT 1
ACT–CL J2035.1–5251	308.7834192	-52.85285109	SPTSZ	0.534	Spec	SLIT 2
ACT–CL J0132.2–0940	23.0608236	-9.681740655	RMDESY3	0.538	Phot	SLIT 4
ACT–CL J0025.9–4133	6.495792727	-41.55493369	SALT	0.539	Spec	SLIT 2
ACT–CL J0006.9–0041	1.728695689	-0.6882677287	SDSS	0.541	Spec	SLIT 1
ACT–CL J2335.1–4544	353.7818597	-45.74167253	SPTSZ	0.548	Spec	SLIT 1
ACT–CL J0031.4–0144	7.87185389	-1.737484056	SDSS	0.552	Spec	SLIT 3
ACT–CL J0137.4–0827	24.35531649	-8.459752465	SDSS	0.565	Spec	SLIT 1
ACT–CL J0046.4–3912	11.60215182	-39.20113631	RMDESY3	0.592	Phot	SLIT 1
$0.6 \leq z < 0.7$						
ACT-CL J0240.0+0115	40.01341585	1.264729555	SDSS	0.601	Spec	SLIT 3
ACT-CL J0020.5+0239	5.149592789	2.654379605	SDSS	0.604	Spec	SLIT 1
ACT–CL J0446.7–3703	71.69625157	-37.06559394	RMDESY3	0.605	Phot	SLIT 2
ACT–CL J0502.9–2902	75.73231299	-29.03983108	RMDESY3	0.610	Phot	SLIT 2
ACT–CL J0559.7–5249	89.93337941	-52.82435631	S16	0.611	Spec	SLIT 2
ACT–CL J0352.9–5648	58.240247	-56.80302889	SPTSZ	0.614	Spec	SLIT 3
ACT-CL J0030.8+0102	7.70482863	1.035445135	SDSS	0.622	Spec	SLIT 1
ACT-CL J0008.8+0117	2.224788372	1.283422211	SDSS	0.625	Spec	SLIT 2
ACT–CL J0106.1–0618	16.5403171	-6.31656202	RMDESY3	0.648	Phot	SLIT 2
ACT-CL J0058.0+0031	14.52261915	0.5171037687	SALT	0.649	Spec	SLIT 1
ACT-CL J0026.2+0120	6.566833228	1.337233948	SDSS	0.650	Spec	SLIT 1
ACT–CL J0248.9–0328	42.24175685	-3.475044624	SDSS	0.664	Spec	SLIT 1
ACT–CL J0021.5–4902	5.390749708	-49.0388432	SALT	0.668	Spec	SLIT 3
ACT–CL J0022.7–4832	5.691128947	-48.53857925	SALT	0.668	Spec	SLIT 2
ACT–CL J0521.1–5104	80.28983579	-51.07356893	SPTSZ	0.678	Spec	SLIT 3
ACT–CL J0142.1–5032	25.5472056	-50.5454761	SPTSZ	0.679	Spec	SLIT 1
ACT–CL J0218.2–0041	34.56509704	-0.6937429636	S16	0.681	Spec	SLIT 1
ACT–CL J0359.3–5218	59.8417752	-52.31260879	RMDESY3	0.681	Phot	SLIT 3
ACT–CL J0012.4–3346	3.112340948	-33.78132606	SALT	0.688	Spec	SLIT 2
ACT-CL J0213.3+0605	33.33740402	-6.099964634	SALT	0.698	Spec	SLIT 2
$0.7 \leq z < 0.8$						
ACT–CL J0203.2–0123	30.81525453	-1.398541107	SDSS	0.711	Spec	SLIT 2
ACT–CL J0014.7–4952	3.69484403	-49.8754753	SPTSZ	0.715	Spec	SLIT 2

ACT-CL J0238.1+0306	39.53318905	3.104090322	RMDESY3	0.715	Phot	SLIT 3
ACT-CL J0119.9+0055	9.99840253	0.9250359155	S16	0.736	Spec	SLIT 2
ACT–CL J2340.2–4619	355.0619857	-46.33232818	RMDESY3	0.746	Phot	SLIT 2
ACT–CL J0008.6–3808	2.174990482	-38.14982901	SALT	0.753	Spec	SLIT 5
ACT-CL J0102.5+0341	15.64830511	3.683575684	SDSS	0.765	Spec	SLIT 4
ACT–CL J0027.6–4742	6.910401503	-47.70904531	SALT	0.774	Spec	SLIT 1

Table 2.1: BEAMS galaxy clusters used in this study. *Col. 1*: cluster name given by field name and J2000 coordinates of cluster center; *col. 2*: Right ascension (R.A.) (J2000) of the cluster; *col. 3*: Declination (Decl.) (J2000) of the cluster; *col. 4*: The z Source column indicates the source of the redshift: SDSS = spectroscopic redshift from the Sloan Digital Sky Survey; SPTECS = spectroscopic redshift from the SPT Polarization Extended Cluster Survey (Bleem et al., 2015); SPTSZ = spectroscopic redshift from the SPT SZ survey (Bocquet et al., 2019); SALT = spectroscopic redshift from the Southern African Large Telescope (Hilton et al., 2018, 2021); S16 = spectroscopic redshift from Sifon et al. (2016); RMDESY3 = photometric redshift from the redMaPPer-detected clusters in the DES Year 3 footprint (Rykoff et al., 2016). *Col. 5*: spectroscopic or photometric redshift of the BCG. *Col. 6*: BCG redshift type indicates whether the redshift is spectroscopic ("spec") or photometric ("phot"). *Col. 7*: slit number indicates the position of the BCG in the long-slit data.

Chapter 3

Stacking and stellar kinematics

> "By which Allah guides those who pursue His pleasure to the ways of peace and brings them out from darkness into the light, by His permission, and guides them to a straight path."
>
> *Surah Al-Ma'idah, Qur'an 5:16*

If we are to gain insight into the mechanisms that govern galaxy formation, it is important that we first investigate the bulk motion of the stars and gas in galaxies. The motion of stars in a galaxy can allow us to gain knowledge of the potential of the gravitational wells of galaxies and therefore help us understand how these massive structures form and evolve in these potentials (Cappellari, 2017). Stellar kinematics also enable us to probe the dynamical state of the luminous baryons trapped within these potentials by providing measures of angular momentum and dynamical temperature (the ratio of kinetic energy in random motion vs. ordered rotation). The kinematics properties of BCGs can give us insight into their formation and evolutionary histories.

In this study stellar kinematic analysis was performed using the spectral fitting code pPXF (Cappellari & Emsellem, 2004; Cappellari, 2017). In this chapter we discuss how to retrieve, through the used software, stellar kinematics, starting from galaxy spectra. We also discuss how we stack the data in order to derive stellar kinematics properties of our spectra. Moreover, in Section 3.1, we introduce the aforementioned software and we look at how it recovers the LOSVD of a galaxy. In Section 3.2, we look at the first measurements we made to recover stellar kinematics from the galaxy spectra. Section 3.3 describes the basic concept of stacking, and the specific application to our observed spectra. Under this Section we also introduce the stacking program, *specstack* (Thomas, 2019). We end the chapter by looking at the improvements "stacking" has on the spectra when measuring stellar kinematics, this is discussed in Section 3.4.

3.1 pPXF

The Penalized Pixel-Fitting (pPXF)[1] method derives the stellar or gas kinematics and stellar populations from absorption-line spectra of galaxies, using a maximum penalized likelihood method. The original approach was first introduced by Cappellari & Emsellem (2004) and was later improved upon by Cappellari (2017) and further improvements were made by Cappellari (2022), with the addition of photometry and linear constraints. Due to the high robustness of the algorithm in inferring stellar and gas kinematics, pPXF has been used to estimate velocity dispersions for our observed BCGs. Specifically, the penalisation of the non-well-fitted pixels minimises the mismatch with the used templates. We fit our BEAMS spectra using the Vazdekis et al. (2010) stellar templates, which are derived from the MILES stellar library (Sánchez-Blázquez et al., 2006), with metallicity ([Z/H]) ranging from -1.71 to +0.22, and ages between 0.63 Gyr to 16 Gyr. The library has a spectral resolution of 2.51 Å FWHM, which covers the wavelength range 3540 - 7409 Å. It also has 985 stellar templates and thus has extensive coverage of the different stellar spectral types in the given wavelength range. We use the MILES stellar library because it is believed to be the best existing flux calibrated library up-to-date. An example of a representative pPXF produced fit is given on Figure 3.1.

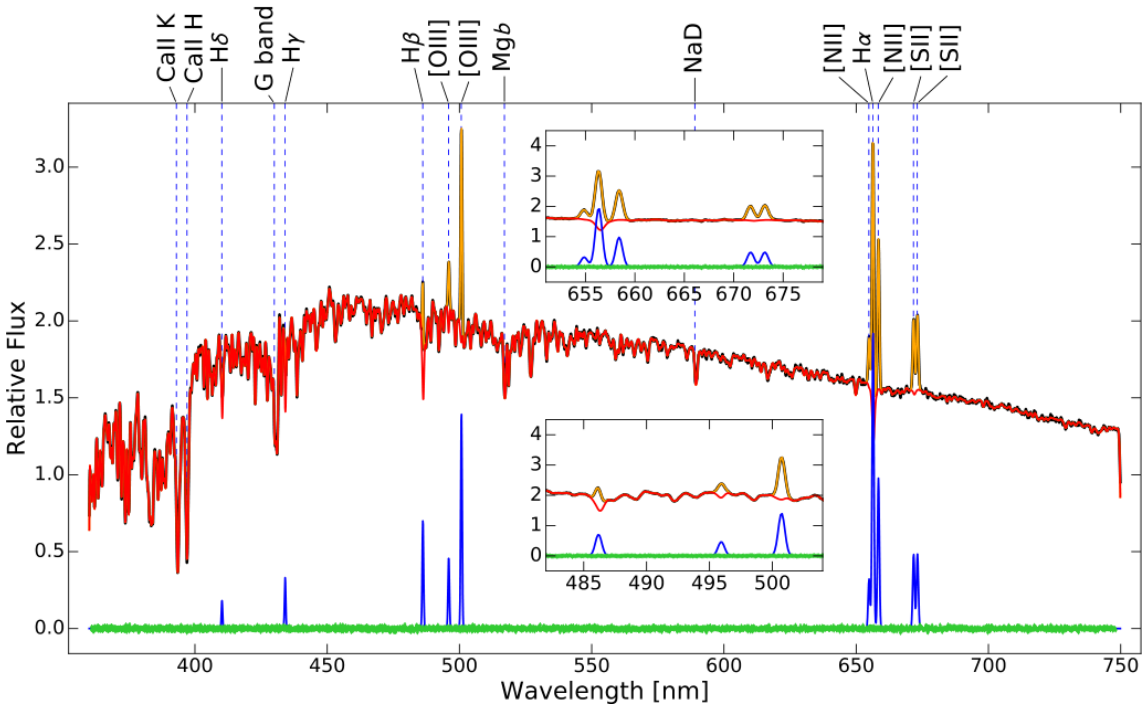


Figure 3.1: An example fit from pPXF. The black line (mostly hidden by the fit) is the relative flux of the observed spectrum. The red line is the pPXF fit for the stellar component, while the orange line is a fit to the gas emission lines. The green symbols and pink line at the bottom are the fit residuals, while the blue lines is the gas-only best-fitting spectrum. The main absorption and emission features are indicated at the top of the plot. Image taken from Cappellari (2017).

[1]This software is publicly available at : http://www-astro.physics.ox.ac.uk/~mxc/software/.

3.1.1 The workings of pPXF

As mentioned, the algorithm is mainly used as a way to recover stellar kinematics, more especially, the velocity (V), the standard deviation (σ), as well as high-order Gaussian moments such as the skewness (h_3), which is the LOSVD's departure from symmetry and the kurtosis (h_4), which measures the LOSVD's symmetric departure from the Gaussian distribution (Gerhard, 1993; Van Der Marel & Franx, 1993) from the LOSVD using a Gauss-Hermite expansion of the absorption-line profile, given in Equation 1.7.5 as:

$$\mathcal{L}(v) \;=\; \left[\frac{e^{-(1/2)x^2}}{\sigma\sqrt{2\pi}}\right]\left\{1 \;+\; \sum_{m=3}^{M} h_m H_m(x)\right\}$$

$\mathcal{L}(v)$, is the LOSVD, and the individual terms in Equation 3.1.1 are given in more detail under Equation 1.7.5. The pPXF algorithm starts by using an "initial guess" input values of the velocity (V) and the velocity dispersion (σ) to convolve template spectra in order to fit the object spectra, while keeping the Gauss-Hermite (h_3, h_4, ..., etc.) parameters constant (Cappellari & Emsellem, 2004). The algorithm then determines the best fitting LOSVD parameters by modelling the galaxy spectrum according to the following equation (Cappellari & Emsellem, 2004):

$$G_{\mathrm{mod}}(x) \;=\; \sum_{n=1}^{N} w_n [B * T_n](x) \;+\; \sum_{i=0}^{I} b_i \mathcal{P}_i(x), \;\; w_n \geq 0 \tag{3.1.1}$$

where w_n and b_i are the weights to be fitted, $B(x) = \mathcal{L}(cx)$ is the spectral broadening function of the LOSVD, $\mathcal{L}$, with c, being the speed of light. And $*$ indicates convolution and T_n is the library of n stellar templates. According to Cappellari & Emsellem (2004), $\mathcal{P}_i$, represent the set of Legendre polynomials of order i that adjust the stellar templates to best fit the spectrum.

These weights, w_k and b_i, are then calculated by minimizing the χ^2 function, which is given as:

$$\chi^2 \;=\; \sum_{l=1}^{L} r_l^2 \tag{3.1.2}$$

where r_l is the residual, and is defined as

$$r_l \;=\; \frac{G_{\mathrm{mod}}(x_l) \;-\; G_{x_l}}{\Delta G(x_l)} \tag{3.1.3}$$

where $G(x_l)$ is the observed Galaxy spectrum. The fitting consists of a nonlinear least-squares optimization of the parameters, V, σ, h_3, ..., h_M. The algorithm then uses a

penalty function, derived from the deviation of the object line profile from a Gaussian, which is added to the χ^2 of the fit. Therefore, a penalized χ^2 is calculated as (Cappellari & Emsellem, 2004):

$$\chi_p^2 \;=\; \chi^2\Big(1+\lambda^2\mathcal{D}^2\Big) \tag{3.1.4}$$

where $\mathcal{D}^2$ is the penalty function, which according to Cappellari & Emsellem (2004) can be approximated by

$$\mathcal{D}^2 \;\approx\; \sum_{m=1}^{M} h_m^2 \tag{3.1.5}$$

and λ, represents a *bias* parameter chosen by the user. The fitting procedure is repeated until the variance is minimized and the fit converges. This pPXF procedure predisposes the solution with just a singular Gaussian solution when the S/N is low, while it is able to recover the higher-order moments of the absorption line spectrum when the S/N is high. For a more thorough discussion of the algorithm the reader is referred to Cappellari & Emsellem (2004).

Improvements were made by Cappellari (2017) to the spectral fitting code, pPXF, include but are not limited to, a better use of stellar templates, their improvements also provide more accurate velocities regardless of σ. More so, according to Cappellari (2017) these improvements are important for galaxy redshift determinations, or when measuring the LOSVD of individual stars. Recent versions of the spectral fitting code takes into account the instrumental Gaussian dispersion, $\sigma_{\rm inst}$, and template Gaussian dispersion, $\sigma_{\rm temp}$, of the observation to more accurate fit the velocity dispersion from the spectrum. This is essential for cases when there is a large difference between $\sigma_{\rm temp}$ and $\sigma_{\rm temp}$ (Cappellari, 2017).

On their 2022 paper, Cappellari made the following improvements to the pPXF algorithm, they introduced a well sampled variable-σ convolution. This improvement was made to avoid under sampling issues. They also included linear constraints on the template weights. These were used for example to constrain the sum of weights (i.e. the luminosity) of different template groups to constitute a certain fraction of the total light, i.e. to perform kinematic bulge/disks decompositions or to study stellar population of different kinematic components (see Cappellari, 2022, and references therein).

Cappellari (2022) also included photometric measurements with full-spectrum fitting, they achieved this by acknowledging that: (i) the photometric fluxes do not depend on the LOSVD ($\mathcal{L}_n(v)$) like the spectroscopic ones and (ii) the photometry of an individual galaxy is generally unable to constrain both the calibration inaccuracies and the template weights. This implies that one cannot include polynomials as done for the spectroscopy (Cappellari, 2022).

To be able to achieve photometric measurements, Cappellari (2022) defined a function that describes an individual template spectrum, $T_n(\lambda)$, convolved * with the LOSVD, which is allowed to be different for each template as:

$$g_n(\lambda) \;=\; T_n(\lambda) * \mathcal{L}_n(v)$$

With this notation, the model of the galaxy spectrum then becomes:

$$G^{\rm spec}_{\rm mod}(\lambda) \;=\; \sum_{n=1}^{N} w_n \left[g_n(\lambda) A_n(\lambda) \sum_{k=1}^{K} a_k \mathcal{P}_k(\lambda) \right] \;+\; \sum_{i=0}^{I} b_i \mathcal{P}_i(\lambda) + \sum_{j=1}^{J} c_j \mathcal{S}_j(\lambda) \qquad (3.1.6)$$

where $\mathcal{P}_i$ and $\mathcal{P}_k$ are the additive and multiplicative polynomials respectively and the $\mathcal{S}_j$ are the optional spectra of the sky. This model is nearly the same as that given in Cappellari (2017, eq. 11), except for the fact that here each template spectrum can have a different attenuation function A_k. Moreover, both the attenuation and multiplicative polynomials can be used at the same time, rather than being alternatives (Cappellari, 2022). This is especially useful when including photometry in the fit, which removes the degeneracy between the attenuation curve and the multiplicative polynomials

The model for the photometric measurements, in linear units, not magnitudes, is given by Cappellari (2022) as:

$$G^{\rm phot}_{\rm mod}(\lambda_q) \;=\; \sum_{n=1}^{N} w_n \; \langle g_n(\lambda) A_n(\lambda) \rangle_q, \qquad (3.1.7)$$

where $\langle \bullet \rangle_q$ represents the mean flux in the q-th photometric band with effective wavelength λ_q. Unlike the spectroscopic model of equation 3.1.6, the photometric model of equation 3.1.7 does not include polynomials or the sky spectrum.

When one has a good estimate of the galaxy redshift, or when performing a grid search for the best-fitting redshift, the redshift of the spectrum changes a little (Cappellari, 2022). This makes the quantities $\langle g_n(\lambda) \rangle_q$ essentially independent of $\mathcal{L}_n(v)$ during a fit. And so Equation 3.1.7 can be rewritten as:

$$G^{\rm phot}_{\rm mod}(\lambda_q) \;=\; \sum_{n=1}^{N} w_n \; \langle g_n(\lambda) A_n(\lambda) \rangle_q, \qquad (3.1.8)$$

The $\langle g_n(\lambda) \rangle_q$, can be computed for all templates before the fit. This approach ensures that the computation time when adding photometry to a fit insignificant compared to the fitting of the spectrum alone (Cappellari, 2022). For a detailed and thorough discussion on these changes the reader is referred to Cappellari (2022).

3.2 Fitting individual BCGs

In order to find the stellar kinematic properties for our BCGs, we first attempted to measure the kinematic properties for individual BCGs. The advantage of using the pPXF method to get stellar kinematic measurements is that it can correlate more than one absorption feature of the spectrum when calculating the velocity dispersion. Furthermore, the Gauss-Hermitian polynomials reduce degeneracy when fitting the LOSVD due to their orthogonality (Gerhard, 1993; Van Der Marel & Franx, 1993). On Figure 3.2 we show a grid of different values used for h_3 and h_4 (with constant values for V and σ), to better visualize the effect the Hermitian terms have on the Gaussian, the Figure illustrates the Gaussians' shape as it changes with the different values for h_3 and h_4, respectively.

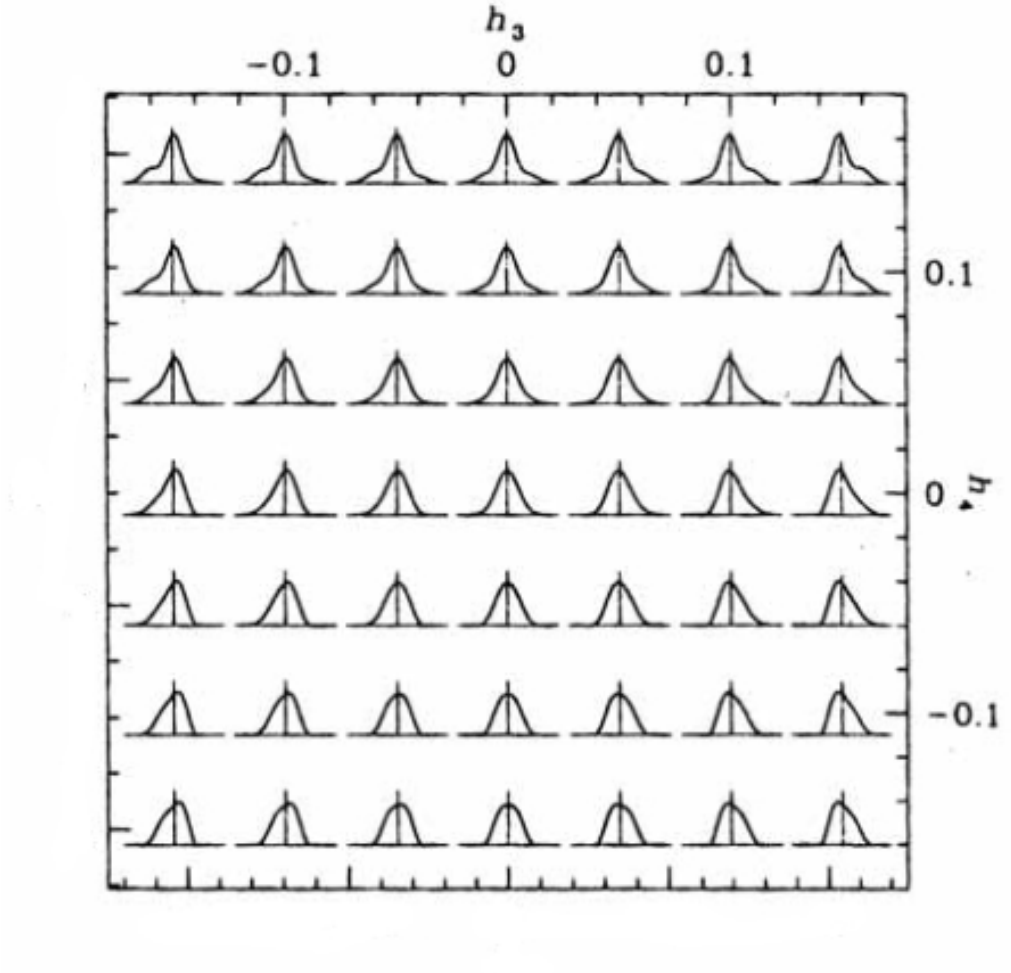
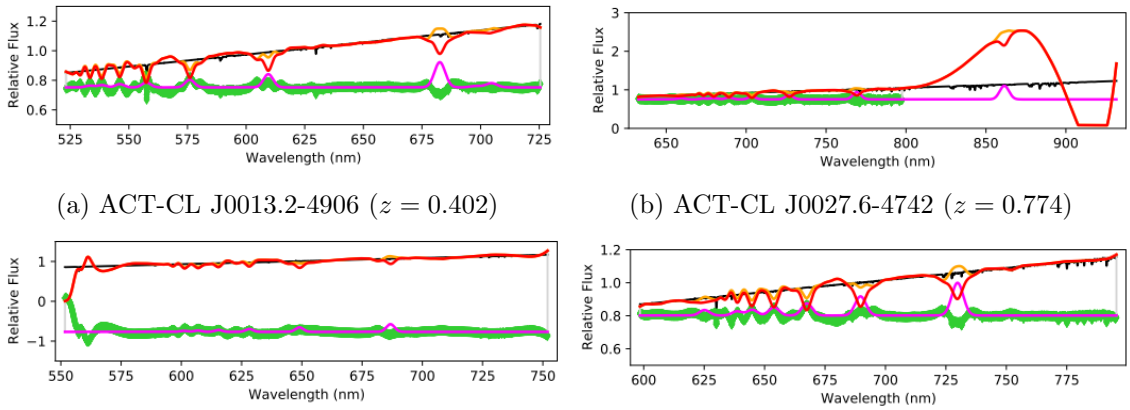


Figure 3.2: A montage showing how a velocity distribution typically changes depending on its shape parameters h_3 and h_4 (and constant V and σ). The central distribution is a pure Gaussian when $h_3 = 0$ and $h_4 = 0$. Image taken from Binney & Merrifield (2000).

In order to find the stellar kinematic components, we first attempted to fit model spectra to the spectra of individual BCGs using the modified pPXF[2] routine. The routine reads

[2] https://drive.google.com/file/d/1i71UpBISXvR_p1hX1z8tWZXfeJ5QOcPv/view?usp=sharing

both the 1D (for the data) and 2D (to get "HEADER" information) FITS files to make measurements. On Figure 3.3 we show examples at different redshifts of the best fit pPXF outputs in our SALT sample. From the fits shown in the Figure, we can visually see that pPXF struggles to fit the model spectra to single BCG spectra, this is due to low S/N and this leads to completely unreliable measurements of the kinematic components. We used χ^2 statistics to determine the best fitting template.



(a) ACT-CL J0013.2-4906 ($z = 0.402$)

(b) ACT-CL J0027.6-4742 ($z = 0.774$)

(c) ACT-CL J0046.4-3912 ($z = 0.592$)

(d) CT-CL J0359.3-5218 ($z = 0.681$)

Figure 3.3: Example of fits from pPXF for individual BCG spectra. The black line is the relative flux of the observed spectrum. The red line is the pPXF fit for the stellar component, while the orange line is a fit to the gas emission lines. The green symbols and pink line at the bottom are the fit residuals, while the blue lines is the gas only best-fitting spectrum.

3.3 Stacking

Stacking is a cutting-edge technique in the field of astronomy that combines multiple observations of celestial objects to increase the signal-to-noise ratio (S/N) of the data. This method is particularly useful for analyzing large samples of clusters or for faint and small clusters (e.g., distant and/or low mass) (Gifford et al., 2017). The traditional method of obtaining high-quality data for these objects can be prohibitively expensive, which is why stacking has become a popular alternative for astronomers. By stacking multiple observations, astronomers can effectively boost the S/N of their data, providing a clearer picture of the objects being studying. Stacking also has the advantage of homogenizing the projected shape, reducing the bias from spherically fit profiles to non-spherical systems (Gifford et al., 2017). However, stacking can also lead to the introduction of new systematic biases. For example, in their study Biesiadzinski et al. (2012) showed how stacking SZ signals can result in significant systematic distortion if the optical cluster sampling is not characterized properly (Gifford et al., 2017). In order to improve the S/N of the BEAMS BCGs sample we will also stack the spectra. We will achieve this by stacking spectra of BCGs that are of similar redshifts. In the following Section we discuss *specstack* the program used to stack the spectra of our BCG sample and how we achieved the stacking.

3.3.1 Specstack

Specstack[3] is a program that stacks spectra of galaxies into a single averaged spectrum (Thomas, 2019). The program reads individual spectrum files and processes each of them separately. To achieve this; the program de-redshifts the wavelength grid to $z = 0$, and normalizes the flux to the region given by the user using the "normlimits" argument. In the region given by these limits, the mean of the flux is set to 1. Once all the spectra are normalized and de-redshifted; *specstack* looks at the maximal wavelength window where the stacked spectrum can be computed with all the individual spectra. To do so it looks at all the de-redshifted grids and collects the starting-bluest and final-reddest wavelength (Thomas, 2019).

From the set of blue wavelengths, *specstack* will take the maximal wavelength (L_b). And from the set of red wavelengths it will take the minimal wavelength (L_r). This defines the final rest-frame window of the stacked spectra. This ensures that each point in the stack spectrum is computed with the same amount of individual flux points. Then all the individual spectra are rebinned in a common wavelength grid of bin = 1 Å and the limits L_b and L_r (Thomas, 2019). Once this is done, *specstack* computes the final stacked spectrum flux using the mean of all the individual spectra by using a sigma-clipping algorithm (see Maples et al., 2018).

For our spectra, the upper and lower limits of the wavelength region in the spectrum where the spectrum (each of the individual spectra have to be normalized before they are stacked) is normalized are 4200 Å and 4400 Å, respectively. The binning in wavelength increments of the new stacked spectrum is 0.316 Å. The wavelength increment of 0.316 Å was chosen because it is that of the SALT spectra before stacking, since all the SALT spectra have the same wavelength increments. The stacked spectrum should then also have the same wavelength increments.

Quick ref.	z range	BCGs in z range	Number of groups	Average number of BCGs per stack
(1)	(2)	(3)	(4)	(5)
1	$0.3 < z < 0.4$	21	12	10
2	$0.4 \leq z < 0.5$	17	08	7.8
3	$0.5 \leq z < 0.6$	14	09	5.8
4	$0.6 \leq z < 0.7$	20	11	10
5	$0.7 \leq z < 0.8$	09	06	3.6

Table 3.1: *Column 1*: Quick reference to the z range. *Column 2*: z range. *Column 3*: The number of BCGs in z range. *Column 4*: Is the number of groups in the z range. *Column 5*: Is the average number of BCGs used per stack.

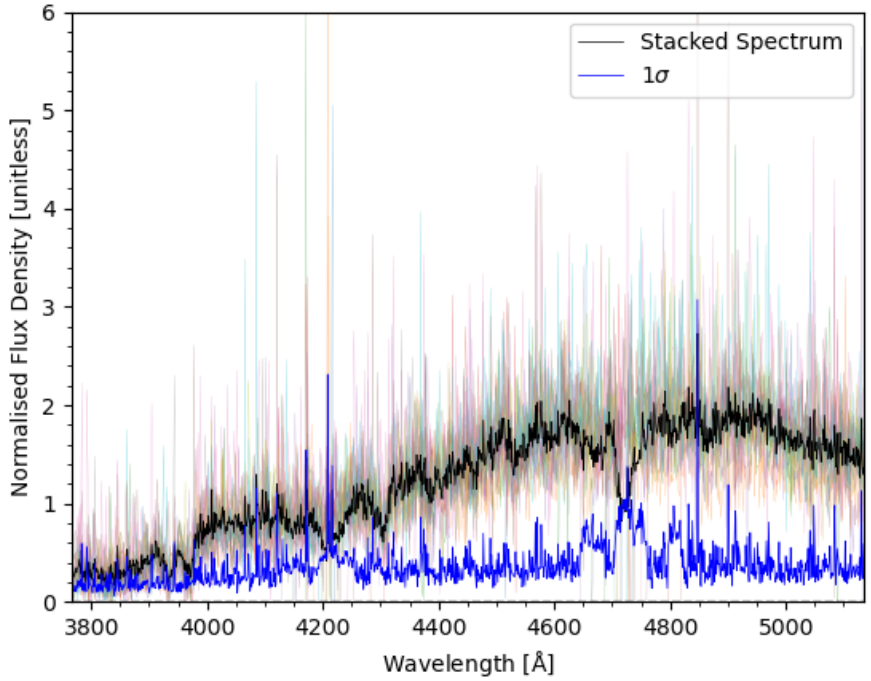
[3] https://specstack.readthedocs.io/en/latest/

In order to use *specstack*, the BCGs were firstly grouped into five groups, these groups were $0.3 < z < 0.4$, $0.4 \leq z < 0.5$, $0.5 \leq z < 0.6$, $0.6 \leq z < 0.7$ and $0.7 \leq z < 0.8$ and from these groups, the so-called "stacking groups" were derived by taking BCGs with redshift at $\pm$ 0.06 of each other. The data was divided into "stacking group" in order to better track which BCGs have been stacked and to better manage the data. The stacked spectra varied from 4 spectra to as many as 10 spectra per stacking group. Table 3.1 provides the basic information of the five z range groups that our data was divided into, this Table includes: the number of BCGs per z group, number of subgroups and average number of BCGs used per stack.

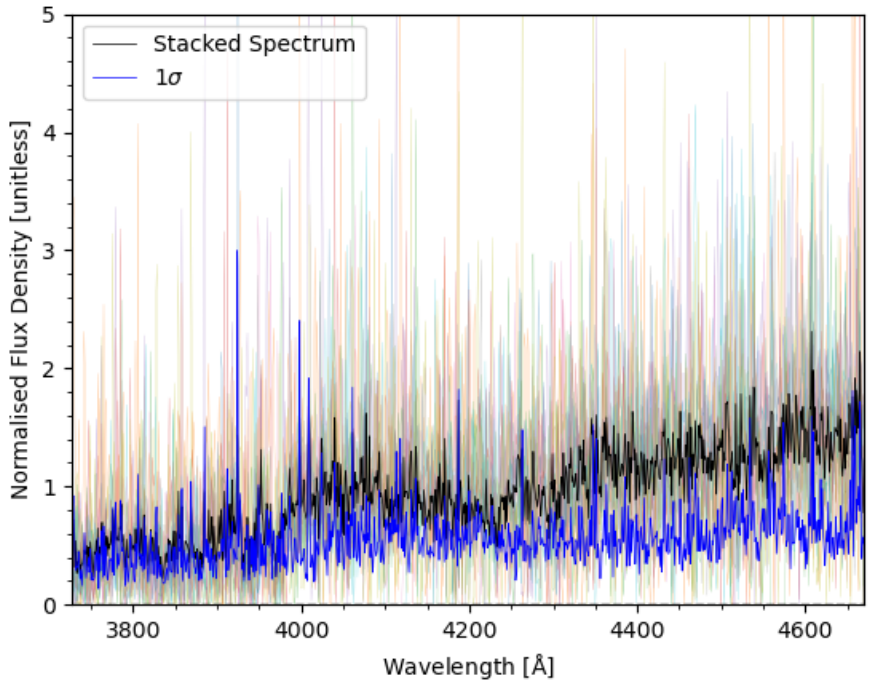
To determine the optimal number of BCGs to stack per group; we tested a number of configurations and experimented with the z range within the subgroups. The number of members in each group was used as the determining factor as to how many BCGs we can stack together. The difference in z between the member with the lowest and highest z value was also another factor to consider. We did not want to stack BCGs with redshifts too far apart (as the limits and chip gaps will cause too much wavelength lost). For example in the group $0.5 \leq z < 0.6$; the member with the lowest redshift has $z = 0.503$ and the highest has $z = 0.592$; a stack with those two members would result in a spectra with huge wavelength loss.

Using the z information given above we started stacking the spectra in each z range with respect to $\pm$ 0.06 difference in the redshift. For the first set of experiments we started with just using 3 BCGs per stack. For some groups the resultant stacked spectra from *specstack* still had a lot of noise. We then gradually added BCGs to the stack as we did further experimentation with the data. This was done to ensure that we arrive at an optimal number of stacked groups that have high enough S/N, but also to have as many stacks as we can, to use later in pPXF to make kinematic measurements.

One of the advantage of stacking spectra is that, stacking improves the S/N of the spectra and thus leading to more accurate measurements of stellar kinematic properties, such as the velocity dispersion. In Figure 3.4, we show as an example some of the fits produced by *specstack* from some of the "stacking groups". The complete list of Figures that were produced from *specstack* can be found here: https://drive.google.com/drive/folders/1gKVfdWPEYjAhUqYlXKeNnpdymW9YOdTp?usp=sharing.



(a)



(b)

Figure 3.4: Examples of stacked spectra fits produced by *specstack*. (a) Figure from the "$0.3 < z < 0.4$" group. (b) Figure from the "$0.6 \leq z < 0.7$" group. The black line represents the stacked spectra. The different coloured lines represent the different spectra that are stacked together. The blue line at the bottom represents the standard deviation.

3.4 Fitting stacked BCGs

Following the stacking procedure described above, we then attempt to measure kinematic properties from the stacked BCGs. The kinematic information and the resulting plots provided in this section, are measured from a modified version of pPXF [4] which uses the binned spectra from *specstack*. The new binned spectra should lead to more accurate measurements of the LOSVD. The velocity dispersions retrieved during this analysis will be used to further investigate the SFHs of our sample.

3.4.1 Results

In this section we present the measured velocity dispersions from pPXF and the resulting plots of the stacked spectra. The stacked BCGs in each group on this Section can be found on Appendix B.

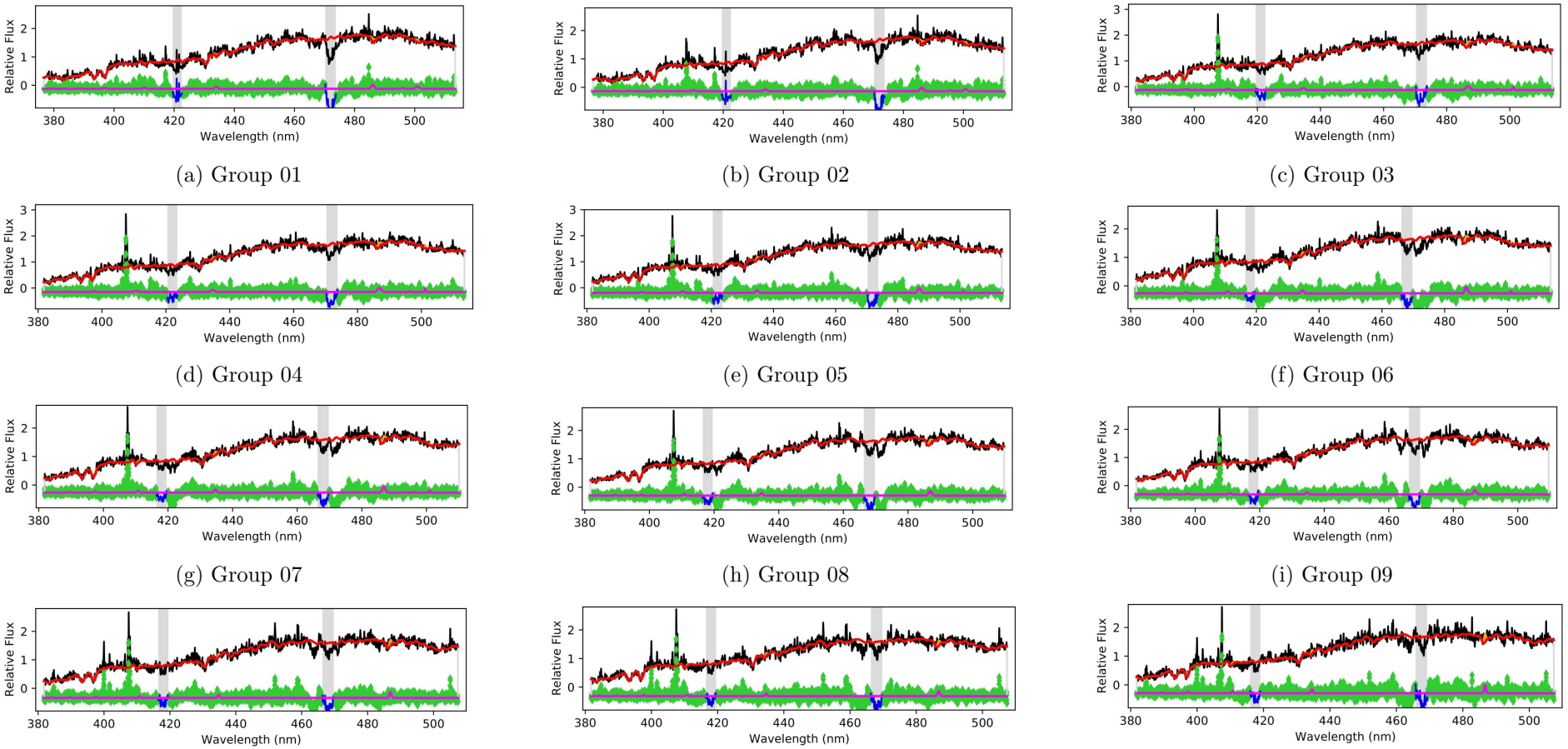
3.4.1.1 $0.3 < z < 0.4$

Here we give the summary of the results of the $0.3 < z < 0.4$ range. We present the velocity dispersions for the groups in this range in Table 3.2. Groups in this range were found to have an average $\sigma = 300 \pm 17$ km.s^{-1}.

Name (1)	σ (2)	Stacked BCGs (3)	$z_{\rm avg}$ (4)	Name (1)	σ (2)	Stacked BCGs (3)	$z_{\rm avg}$ (4)
Group 01	270	10	0.345	Group 07	311	10	0.369
Group 02	281	10	0.350	Group 08	325	10	0.372
Group 03	299	10	0.354	Group 09	308	10	0.375
Group 04	305	10	0.358	Group 10	289	10	0.378
Group 05	317	10	0.362	Group 11	289	10	0.381
Group 06	316	10	0.366	Group 12	289	10	0.384

Table 3.2: Recovered velocity dispersions of $0.3 < z < 0.4$. *Col. 1*: is the group name or number. *Col. 2*: represents the recovered stellar velocity dispersion (σ) measured in km.s^{-1}. *Col. 3*: is the number of stacked BCGs in each group. *Col. 4*: is the average *redshift* of the group.

[4] https://drive.google.com/file/d/1dqgofN-x9SQWVRSazZsb3aEL0dW1j8qD/view?usp=sharing



(a) Group 01 (b) Group 02 (c) Group 03

(d) Group 04 (e) Group 05 (f) Group 06

(g) Group 07 (h) Group 08 (i) Group 09

(j) Group 10 (k) Group 11 (l) Group 12

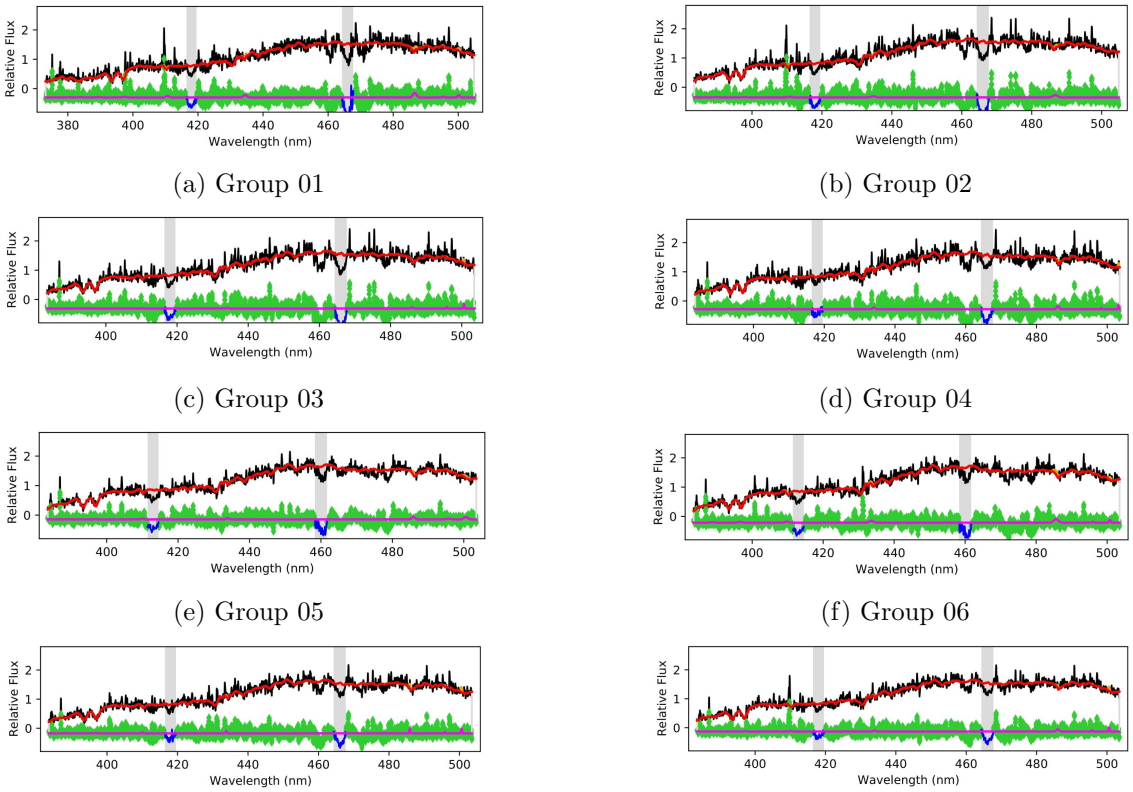
Figure 3.5: Result fits produced by pPXF for the stacked spectra for the z range: $0.3 \leq z < 0.4$. The black line is the relative flux of the stacked spectrum. The red line is the pPXF fit for the stellar component, while the orange line is a fit to the gas emission lines (where present). The green symbols and pink line at the bottom are the fit residuals. The grey solid lines represent the masked regions of the "SALT chip gaps".

3.4.1.2 $0.4 \leq z < 0.5$

In this section we give the summary of the results of the $0.4 \leq z < 0.5$ range. We present the velocity dispersions for this z range in Table 3.3. Groups in this range were found to have an average $\sigma = 249.13 \pm 37$ km.s^{-1}.

Name (1)	σ (2)	Stacked BCGs (3)	$z_{\rm avg}$ (4)	Name (1)	σ (2)	Stacked BCGs (3)	$z_{\rm avg}$ (4)
Group 01	261	07	0.417	Group 05	275	07	0.442
Group 02	225	07	0.428	Group 06	255	07	0.448
Group 03	214	07	0.432	Group 07	296	10	0.434
Group 04	187	07	0.437	Group 08	280	10	0.429

Table 3.3: Recovered velocity dispersions of $0.4 \leq z < 0.5$. The caption of the Table is the same as that of Table 3.2.



(a) Group 01 (b) Group 02

(c) Group 03 (d) Group 04

(e) Group 05 (f) Group 06

(g) Group 07 (h) Group 08

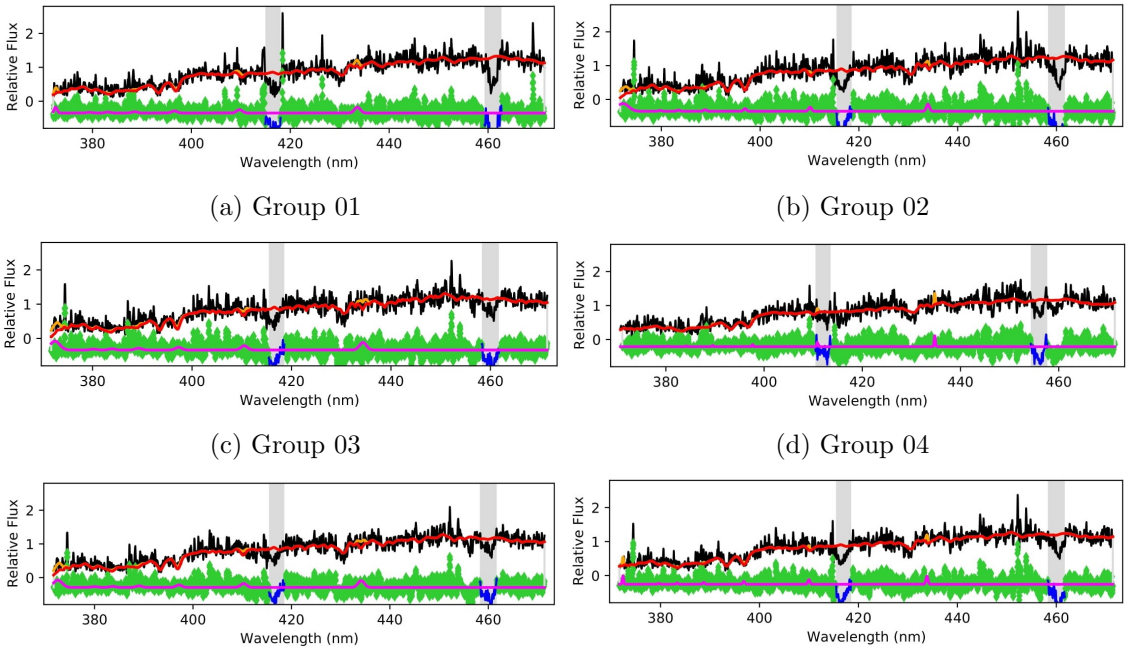
Figure 3.6: pPXF plots for the z range: $0.4 \leq z < 0.5$. The caption of the Figure is the same as that of Figure 3.5.

3.4.1.3 $0.5 \leq z < 0.6$

In this section we give the summary of the results of the $0.5 \leq z < 0.6$ range. We present the velocity dispersions for this range in Table 3.4. Groups in this range were found to have an average $\sigma = 323.9 \pm 80$ km.s^{-1}.

Name (1)	σ (2)	Stacked BCGs (3)	z_{avg} (4)
Group 01	327	05	0.535
Group 02	267	05	0.537
Group 03	187	05	0.540
Group 04	417	05	0.544
Group 05	261	06	0.542
Group 06	324	06	0.539
Group 07	344	06	0.536
Group 08	265	07	0.538
Group 09	420	08	0.540

Table 3.4: Recovered velocity dispersions of $0.5 \leq z < 0.6$. *Col. 1*: is the group name or number. *Col. 2*: represents the recovered stellar velocity dispersion (σ) measured in km.s^{-1}. *Col. 3*: is the number of stacked BCGs in each group. *Col. 4*: is the average *redshift* of the group.

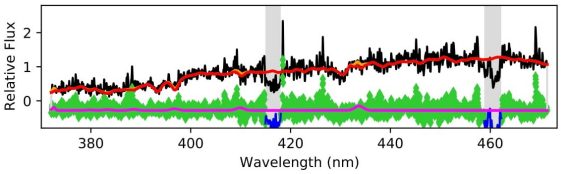


(a) Group 01 (b) Group 02

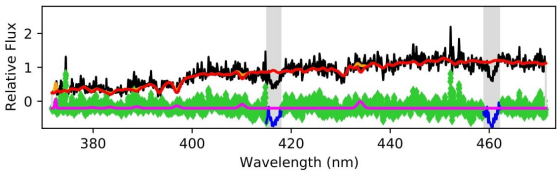
(c) Group 03 (d) Group 04

(e) Group 05 (f) Group 06

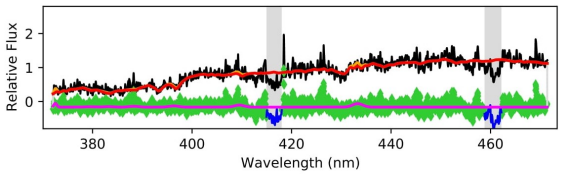
Figure 3.7: pPXF plots for the z range: $0.5 \leq z < 0.6$. The black line is the relative flux of the stacked spectrum. The red line is the pPXF fit for the stellar component, while the orange line is a fit to the gas emission lines (where present).



(g) Group 07



(h) Group 08



(i) Group 09

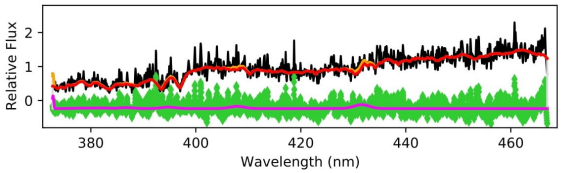
Figure 3.7: (continued) The green symbols and pink line at the bottom are the fit residuals. The grey solid lines represent the masked regions of the "SALT chip gaps".

3.4.1.4 $0.6 \leq z < 0.7$

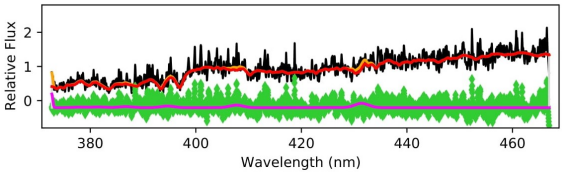
In this section we give the summary of the results of the $0.6 \leq z < 0.7$ range. We present the velocity dispersions for this range in Table 3.5. Groups in this range were found to have an average $\sigma = 311.1 \pm 72$ km.s^{-1}.

Name (1)	σ (2)	Stacked BCGs (3)	$z_{\rm avg}$ (4)
Group 01	233	10	0.619
Group 02	259	10	0.624
Group 03	405	10	0.630
Group 04	373	10	0.633
Group 05	350	10	0.642
Group 06	354	10	0.649
Group 07	369	10	0.655
Group 08	223	10	0.661
Group 09	236	10	0.667
Group 10	236	10	0.671
Group 11	384	10	0.676

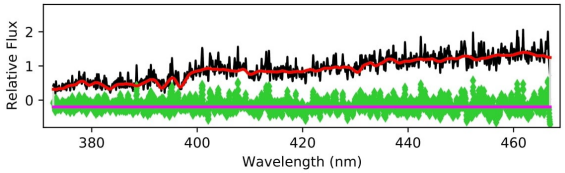
Table 3.5: Recovered velocity dispersions of $0.6 \leq z < 0.7$. *Col. 1*: is the group name or number. *Col. 2*: represents the recovered stellar velocity dispersion (σ) measured in km.s^{-1}. *Col. 3*: is the number of stacked BCGs in each group. *Col. 4*: is the average *redshift* of the group.



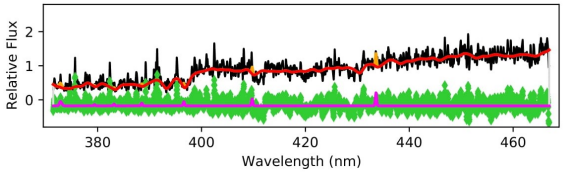
(a) Group 01



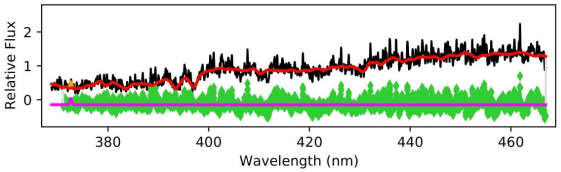
(b) Group 02



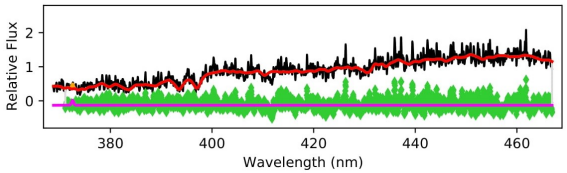
(c) Group 03



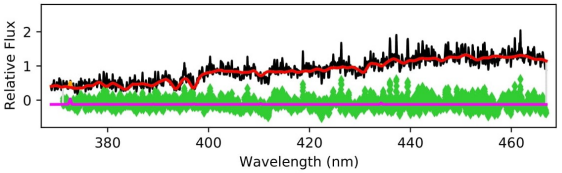
(d) Group 04



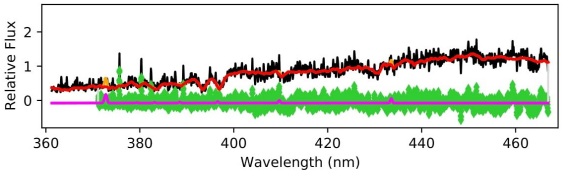
(e) Group 05



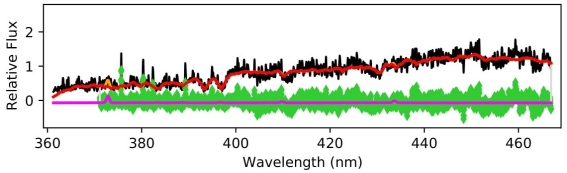
(f) Group 06



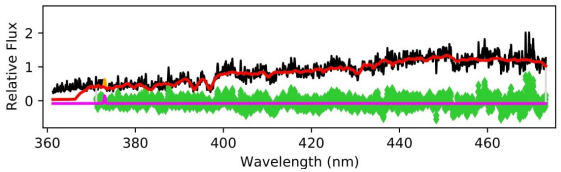
(g) Group 07



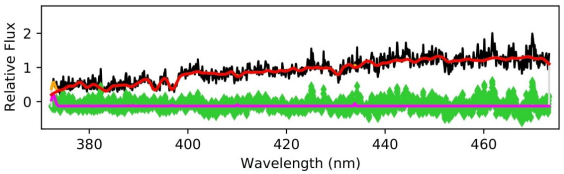
(h) Group 08



(i) Group 09



(j) Group 10



(k) Group 11

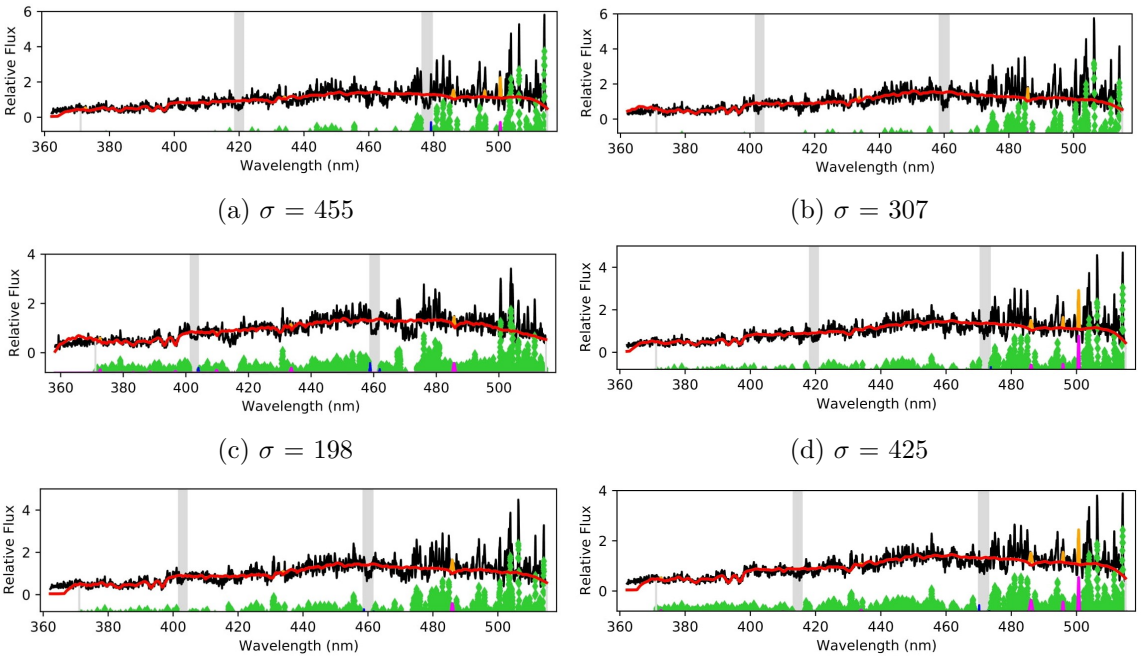
Figure 3.8: pPXF plots for the z range: $0.6 \leq z < 0.7$. The black line is the relative flux of the stacked spectrum. The red line is the pPXF fit for the stellar component, while the orange line is a fit to the gas emission lines (where present). The green symbols and pink line at the bottom are the fit residuals. The grey solid lines represent the masked regions of the "SALT chip gaps".

3.4.1.5 $0.7 \leq z < 0.8$

Here we give the summary of the results of the $0.7 \leq z < 0.8$ range. We present the velocity dispersions for this range in Table 3.6. Groups in this range were found to have an average $\sigma = 337 \pm 106$ km.s^{-1}. This is the only range that we didn't use in latter analysis in this study due to it having a few spectra and the S/N being still low, this means that we might not be able to extract reliable stellar population parameters in FIREFLY.

Name (1)	σ (2)	Stacked BCGs (3)	$z_{\rm avg}$ (4)	Name (1)	σ (2)	Stacked BCGs (3)	$z_{\rm avg}$ (4)
Group 01	455	03	0.745	Group 04	425	04	0.750
Group 02	307	03	0.755	Group 05	235	04	0.760
Group 03	198	03	0.764	Group 06	402	05	0.755

Table 3.6: Recovered velocity dispersions of $0.7 \leq z < 0.8$. Table caption is the same as that of Table 3.5.



(a) $\sigma = 455$ (b) $\sigma = 307$

(c) $\sigma = 198$ (d) $\sigma = 425$

(e) $\sigma = 235$ (f) $\sigma = 402$

Figure 3.9: pPXF plots for the z range: $0.7 \leq z < 0.8$. The caption of the Figure is the same as that of Figure 3.8.

Figures 3.5, 3.6, 3.7, 3.8 and 3.9 show the resulting fits from the new stacked spectra when computed in pPXF. We can see the improved quality of the fits compared to the fits shown in Figure 3.3 where a single BCG spectrum is used. The SALT CCD gaps are masked to improve the quality of the model fit of the spectra.

Chapter 4

Stellar populations and star formation histories

> "Stars, too, were time travelers. How many of those ancient points of light were the last echoes of suns now dead? How many had been born but their light not yet come this far? If all the suns but ours collapsed tonight, how many lifetimes would it take us to realize we were alone?"
>
> Ransom Riggs, *Miss Peregrine's Home for Peculiar Children.*

In order to study the star formation histories of BCGs we need to first measure their stellar population parameters, in order to thoroughly study the stellar populations of these galaxies. In this Chapter we will discuss the stellar population parameters (stellar ages and stellar metallicities) that are used throughout the analysis in this dissertation. We will achieve this by adopting the spectral fitting code FIREFLY (Wilkinson et al., 2017; Goddard et al., 2017; Comparat et al., 2017), taking into account estimates of the velocity dispersion obtained by using the pPXF spectral fitting code in the previous Chapter. In Section 4.1, we introduce the aforementioned software and we look at how it recovers the stellar population parameters of the BCGs. We run the fitting procedure with different options for the IMFs and input stellar libraries. In Section 4.2, we look at the measurements we made to recover the stellar population parameters from the galaxy spectra. Under this Section we also present the results measured from FIREFLY. We end the chapter in section 4.3, where we provide a detailed discussion of the results presented in this Chapter.

4.1 FIREFLY

The Fitting IteRativEly For Likelihood analYsis program (FIREFLY, Wilkinson et al., 2017; Goddard et al., 2017; Comparat et al., 2017)[1] is a χ^2 minimization fitting code that is used for deriving the stellar population properties. This code aims at disentangling stars and dust, subtracting the low-order continuum shape before fitting spectra (Cannarozzo, 2021). A set of SSPs with a wide variety of ages and metallicities are considered iteratively, in order to minimise the χ^2 fitting procedure, allowing FIREFLY to fit non-parametric SFHs (Wilkinson et al., 2017; Cannarozzo, 2021). For our scope, we adopt the stellar population models of Maraston et al. (2020, hereafter MaStar) and Maraston & Strömbäck (2011, hereafter M11). For a more detailed discussion of these models, the reader is referred to Section 1.6.2 of this work. We also make use of the Salpeter (1955) IMF and a Kroupa (2001) IMF. On Figure 4.1, we show as an example a representative fit produced by FIREFLY.

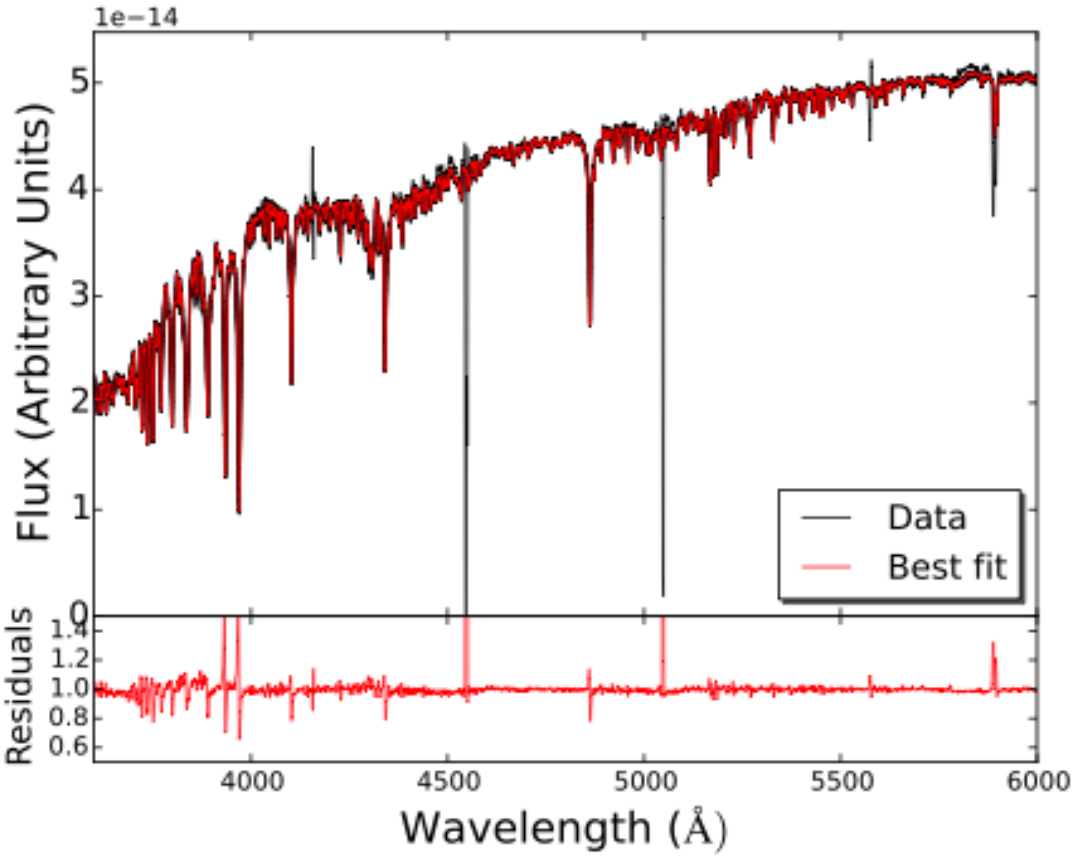


Figure 4.1: An example fit form FIREFLY. The black line (mostly hidden by the fit) is the relative flux of the observed spectrum. The red line is the FIREFLY fit for the specific stellar library. The red line at the bottom marked "Residuals" are the fit residuals. Image taken from https://github.com/FireflySpectra/firefly_release/blob/master/data/FF-fit-example.png.

[1]This software is publicly available at: http://www.icg.port.ac.uk/firefly/

4.1.1 How FIREFLY operates

FIREFLY works on the basis of fitting several model SSPs to a galaxy spectrum and determining which linear combination of SSPs best fit the spectrum (Wilkinson et al., 2017). For instance the spectrum of the galaxy $L(\lambda)$ is approximated as:

$$L(\lambda) = \sum_{i}^{n_{\rm SSP}} a_i L_{\rm SSP}(\lambda) \tag{4.1.1}$$

where $L(\lambda)$ is the luminosity of the galaxy at wavelength (λ), a_i are the weights to be determined and $L_{\rm SSP}(\lambda)$ are the luminosities of the SSPs at wavelength $L(\lambda)$ and $n_{\rm SSP}$ are the number of SSPs (Wilkinson et al., 2017).

FIREFLY fits models to the data by comparing fluxes at the same wavelength. And for each SSP model, FIREFLY tests the goodness of each of the model fits to the data by calculating the associated χ^2 value as (Wilkinson et al., 2017):

$$\chi^2(model_i|data) = \sum_{\lambda} \frac{\Big(F_{data}(\lambda) - F_{model_i}(\lambda)\Big)^2}{\sigma(\lambda)^2} \tag{4.1.2}$$

where F represents the flux of the data or of the model, and $\sigma(\lambda)$ represents the error at the wavelength point λ (Wilkinson et al., 2017). For its set of models FIREFLY recovers an order of ~ 1000 possible combinations of SSPs that fit the galaxy's spectrum. To determine the most statistically likely combination of SSPs, the calculated χ^2 values of the SSPs are weighted by their by corresponding probabilities. The χ^2 probability distribution function is given by Wilkinson et al. (2017) as:

$$P\big(X = \chi^2_o\big) = \int_{\chi^2_o}^{\infty} \frac{1}{2^{(k/2)}\Gamma(\frac{k}{2})} X^{(k/2)-1} e^{-X/2} \mathrm{dX} \tag{4.1.3}$$

where Γ is the Gamma function, χ^2_o is the value of the chi-squared used to find the probability density. k is the degrees of freedom, which according to Wilkinson et al. (2017) can be expressed as $k = N - \nu - 1$, where N is the number of independent observations and ν is the number of fitting parameters used by FIREFLY.

According to Wilkinson et al. (2017), the flux of the final best fitting solution of the spectral fit of the galaxy is the sum of all the fluxes of the solutions weighted by their likelihoods as:

$$F(\lambda) = \sum_{i}^{\rm fits} \frac{P(\chi^2(i))F_i(\lambda)}{\sum_i P(\chi^2(i))} \tag{4.1.4}$$

where $F_i(\lambda)$ is the flux of an individual solution as given in Equation 4.1.1. This can then be plotted as a complete spectral fit (Wilkinson et al., 2017).

4.1.2 Input and Output of FIREFLY

In order to run FIREFLY , the following variables need to be provided as input quantities:

1. The object's spectrum;
2. velocity dispersion (σ);
3. the redshift (z);
4. input stellar population models;
5. wavelength range for the fit.

The average fitting times for a single spectrum are $\sim$ 1 min on a standard computer. The default output of FIREFLY are:

1. Input model and fitting parameters (stellar library, IMF, wavelength range, etc.), galaxy's σ and z;
2. light- and mass weights of each SSP entering the average solution;
3. light- and mass-weighted averaged age and errors;
4. light- and mass-weighted averaged metallicity and errors;
5. best-fitting spectrum;
6. the reduced χ^2 of the average solution.

The above outputs contain a large amount of information which should be useful when robustly determining galaxies SFHs (Wilkinson et al., 2017).

4.2 Results

One of the aims of this dissertation is measuring the stellar populations of the BEAMS BCGs in order to study their star formation histories. The stellar populations are measured with the FIREFLY spectral fitting code, as discussed in Section 4.1. In order to achieve this, we use the stellar velocity dispersions that were measured in the previous Chapter to broaden the stellar templates in FIREFLY. This allows us to fit the BEAMS stacked spectrum to obtain light-weighted stellar metallicities and stellar ages for our BCGs. In this Section the stellar populations for the BEAMS BCGs are presented.

4.2.1 Stellar Populations of the BEAMS BCGs

In this Section, we present the ages and metallicities of our BCGs as shown in Tables 4.1, 4.2, 4.3 and 4.4. In the aforementioned tables, we also provide the reduced-χ^2 ($\chi^2_{\rm red}$) of our plots which measures the goodness of the fit. In this study we utilized different models, namely the M11 Models and MaStar Model, and IMF combinations in FIREFLY to estimate the stellar populations of our BCG groups across various *redshift* intervals. The M11 models incorporate both STELIB and MILES stellar libraries. Each model has its own unique parameters (e.g. stellar library, wavelength range, sampling, and coverage of stellar parameter space, etc.) which results in varying measurements of the stellar populations. We also take into account the $\chi^2_{\rm red}$ value of each FIREFLY produced fit to calculate their systematic errors.

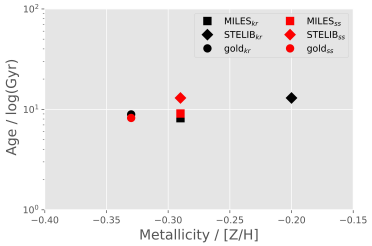
In Figures 4.2, 4.3, 4.4 and 4.5 we present the relationship between age and metallicity for each group within the different redshift intervals. From these plots, we can see that the sample of BCGs used in this analysis has a wider distribution of metallicities compared to their age distributions, with a significant variation seen in the metallicities. However, to account for models that frequently appear as outliers, the metallicity is adjusted by inversely weighing it against the $\chi^2_{\rm red}$, which accounts for the impact of poorer fits in determining the overall metallicity for the sample at each redshift interval.

One possible reason for the large variation in metallicities could be due to the inadequate metallicity coverage in the STELIB stellar library used by the M11 model, leading to overestimation of metallicity for [Fe/H] $>$ 0 dex and underestimation for -1 $<$ [Fe/H] $<$ 0. This is because the STELIB library has a strong concentration of stars found at solar metallicity, making it unreliable for galaxies with metallicities that are outside this scope. A study by Koleva et al. (2008) found that there were systematic biases in the STELIB library's wavelength calibration compared to the MILES library. The MILES stellar library also has limited metallicity coverage, resulting in some BCGs appearing to have higher metallicity, and thus hitting the upper limits of metallicity values. Furthermore, M11 models have a limited representation of low metallicity stars in their parameter space.

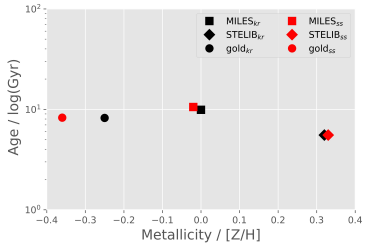
0.3 < z < 0.4

Group	Parameters	M11				MaStar	
		$MILES_{ss}$	$MILES_{kr}$	$STELIB_{ss}$	$STELIB_{kr}$	$gold_{ss}$	$gold_{kr}$
(1)	(2)	(3)	(4)	(5)	(6)	(7)	(8)
01	Age (Gyr)	9.08	8.17	12.98	12.98	8.21	8.91
	Met. (dex)	-0.29	-0.29	-0.29	-0.20	-0.33	-0.33
	χ^2_{red}	0.397	0.361	0.612	0.619	0.577	0.576
02	Age (Gyr)	10.55	9.90	5.54	5.54	8.26	8.21
	Met. (dex)	-0.02	0	0.33	0.32	-0.36	-0.25
	χ^2_{red}	0.433	0.435	0.610	0.610	0.527	0.526
03	Age (Gyr)	11.98	9.82	10.51	8.27	0.02	0.02
	Met. (dex)	-0.14	-0.04	0.13	0.33	0.02	0.02
	χ^2_{red}	0.285	0.283	0.502	0.517	0.168	0.168
04	Age (Gyr)	5.01	3.19	0.74	11.51	1.19	1.19
	Met. (dex)	0.19	0.19	0.33	-0.13	-0.03	-0.03
	χ^2_{red}	0.123	0.126	0.189	0.458	0.161	0.161
05	Age (Gyr)	7.0	3.75	7.36	7.40	8.17	8.17
	Met. (dex)	-0.28	-0.49	0.33	0.32	-0.36	-0.25
	χ^2_{red}	0.139	0.142	0.498	0.510	0.264	0.264
06	Age (Gyr)	7.52	7.82	12.98	4.98	0.2	0.2
	Met. (dex)	-0.59	-0.65	-0.2	0.05	-0.33	-0.33
	χ^2_{red}	0.181	0.187	0.487	0.487	0.241	0.240
07	Age (Gyr)	5.01	6.01	8.31	8.27	10.94	10.94
	Met. (dex)	0.19	-0.28	0.33	0.33	0.05	0.05
	χ^2_{red}	0.118	0.116	0.467	0.460	0.320	0.322
08	Age (Gyr)	4.62	3.62	8.22	8.27	0.46	0.37
	Met. (dex)	0	0	0.35	0.33	-0.37	-0.34
	χ^2_{red}	0.210	0.196	0.477	0.478	0.248	0.276
09	Age (Gyr)	4.01	6.01	6.36	6.36	2.71	7.56
	Met. (dex)	-0.14	-0.25	-0.29	-0.29	0.31	0.16
	χ^2_{red}	0.146	0.145	0.269	0.268	0.269	0.271
10	Age (Gyr)	3.67	7.26	0.92	0.92	7.35	7.35
	Met. (dex)	0.32	0	0.33	0.33	0.31	0.31
	χ^2_{red}	0.253	0.252	0.180	0.181	0.317	0.317
11	Age (Gyr)	3.67	3.67	3.68	3.67	8.17	5.53
	Met. (dex)	0.32	0.35	0.33	0.33	-.33	0.35
	χ^2_{red}	0.225	0.226	0.320	0.319	0.256	0.302
12	Age (Gyr)	4.27	4.27	4.72	6.49	3.66	4.49
	Met. (dex)	0.35	0.35	0.35	0.21	0.32	0.35
	χ^2_{red}	0.337	0.336	0.427	0.453	0.33	0.332

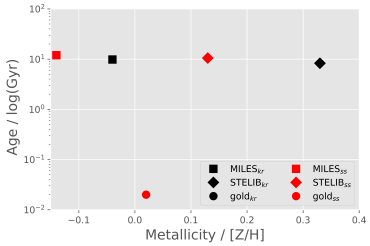
Table 4.1: FIREFLY results for $0.3 \leq z < 0.4$. *Col. 1*: Group number; *col. 2*: parameters measured by FIREFLY, which are the age in Gyr, metallicity in dex and χ^2_{red} which measures the goodness of the fit. *col. 3*: measurements from the MILES model for the Salpeter IMF; *col. 4*: measurements from the MILES model for the Kroupa IMF; *col. 5*: measurements from the STELIB model for the Salpeter IMF and *col. 6*: measurements from the STELIB model for the Kroupa IMF. *col. 7*: measurements from the gold model for the Salpeter IMF; *col. 8*: measurements from the gold model for the Kroupa IMF.



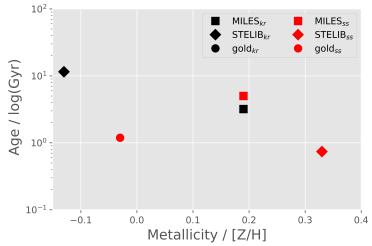
(a) Group 01



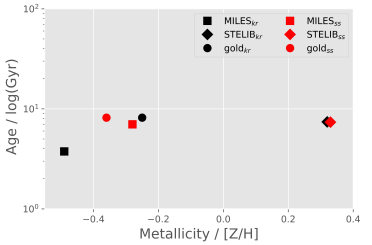
(b) Group 02



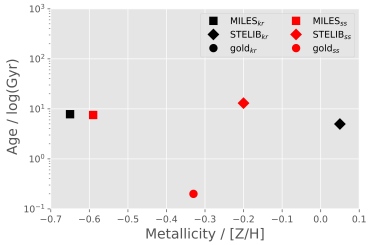
(c) Group 03



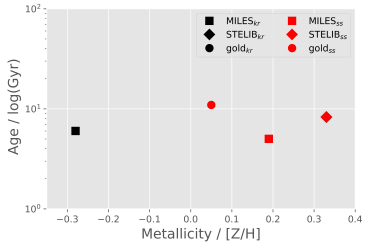
(d) Group 04



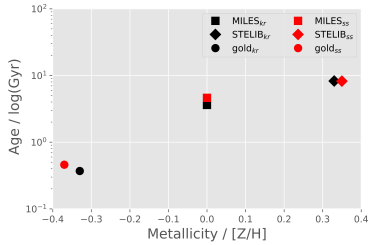
(e) Group 05



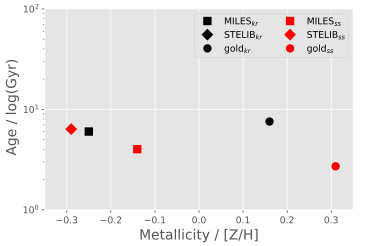
(f) Group 06



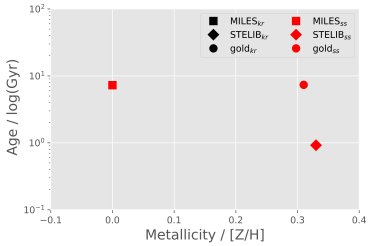
(g) Group 07



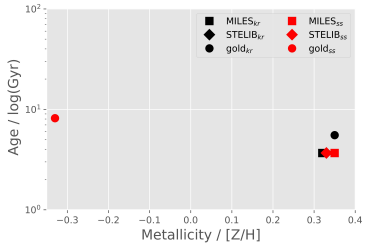
(h) Group 08



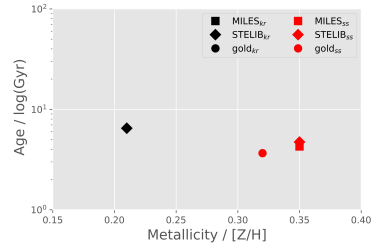
(i) Group 09



(j) Group 10



(k) Group 11



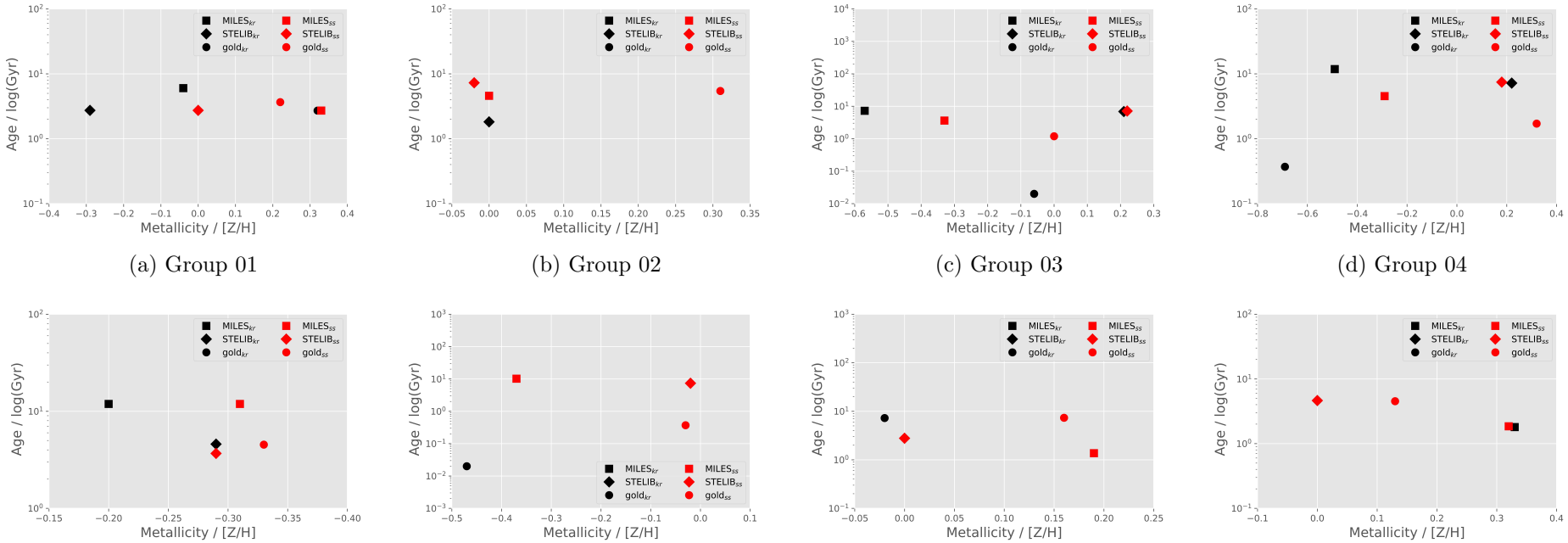
(l) Group 12

Figure 4.2: Age vs. metallicity plots for $0.3 < z < 0.4$. The red markers represent the Salpeter IMF, whereas the black markers represent the Kroupa IMF. The filled in square blocks represent the MILES models, the filled circles represent the gold models and the filled diamonds are for the STELIB Models.

0.4 $\leq z <$ 0.5

Group	Parameters	M11				MaStar	
		$MILES_{ss}$	$MILES_{kr}$	$STELIB_{ss}$	$STELIB_{kr}$	$gold_{ss}$	$gold_{kr}$
(1)	(2)	(3)	(4)	(5)	(6)	(7)	(8)
01	Age (Gyr)	2.71	6.01	2.73	2.73	3.66	2.71
	Met. (dex)	0.33	-0.04	0	-0.29	0.22	0.32
	χ^2_{red}	0.529	0.537	0.334	0.454	0.876	1.01
02	Age (Gyr)	4.58	4.58	7.27	1.82	5.44	5.44
	Met. (dex)	0	0	-0.02	0	0.31	0.31
	χ^2_{red}	0.242	0.243	0.274	0.243	0.335	0.335
03	Age (Gyr)	3.62	7.26	7.14	6.88	1.19	0.02
	Met. (dex)	-0.33	-0.57	0.22	0.21	0	-0.06
	χ^2_{red}	0.190	0.191	0.323	0.340	0.195	0.252
04	Age (Gyr)	4.53	11.81	7.44	7.19	1.71	0.37
	Met. (dex)	-0.29	-0.49	0.18	0.22	0.32	-0.69
	χ^2_{red}	0.203	0.214	0.314	0.316	0.198	0.198
05	Age (Gyr)	11.9	11.9	3.68	4.59	4.53	4.53
	Met. (dex)	-0.31	-0.2	-0.29	-0.29	-0.33	-0.33
	χ^2_{red}	0.350	0.350	0.356	0.361	0.384	0.383
06	Age (Gyr)	10.16	10.16	7.36	7.36	0.37	0.02
	Met. (dex)	-0.37	-0.37	-0.02	-0.02	-0.03	-0.47
	χ^2_{red}	0.293	0.287	0.447	0.44	0.275	0.275
07	Age (Gyr)	1.37	1.37	2.78	2.78	7.35	7.26
	Met. (dex)	0.19	0.19	0	0	0.16	-0.02
	χ^2_{red}	0.137	0.137	0.327	0.327	0.374	0.373
08	Age (Gyr)	1.85	1.80	4.63	4.63	4.53	4.53
	Met. (dex)	0.32	0.33	0	0	0.13	0.13
	χ^2_{red}	0.222	0.225	0.351	0.350	0.421	0.421

Table 4.2: FIREFLY results for $0.4 \leq z < 0.5$. *Col. 1*: Group number; *col. 2*: parameters measured by FIREFLY, which are the age in Gyr, metallicity in dex and χ^2_{red} which measures the goodness of the fit. *Col. 3 - 6*: gives the M11 models; *col. 3*: measurements from the MILES model for the Salpeter IMF; *col. 4*: measurements from the MILES model for the Kroupa IMF; *col. 5*: measurements from the STELIB model for the Salpeter IMF and *col. 6*: measurements from the STELIB model for the Kroupa IMF. *Col. 7 - 10*: gives the MaStar models; *col. 7*: measurements from the gold model for the Salpeter IMF; *col. 8*: measurements from the gold model for the Kroupa IMF.



(a) Group 01 (b) Group 02 (c) Group 03 (d) Group 04

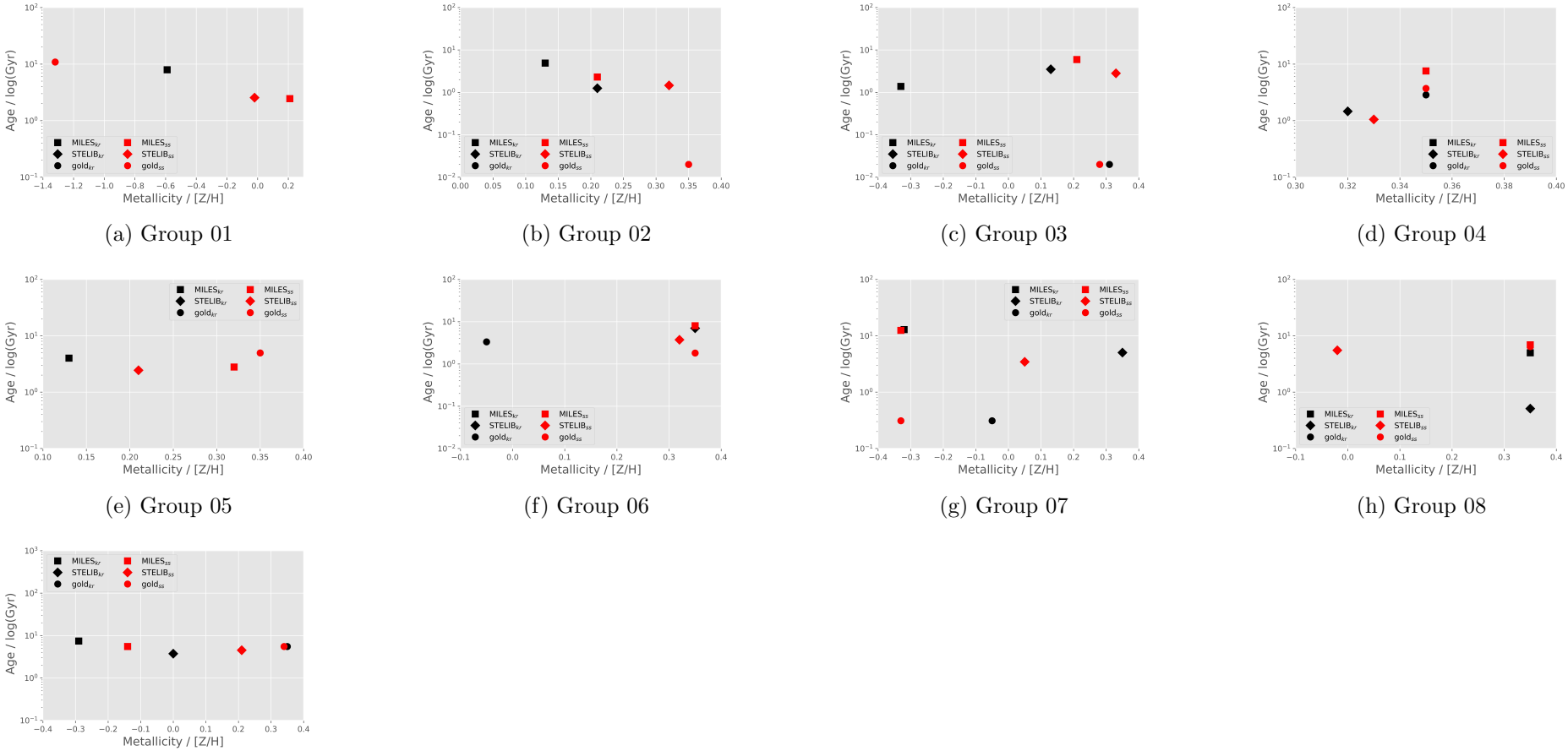
(e) Group 05 (f) Group 06 (g) Group 07 (h) Group 08

Figure 4.3: Age vs. metallicity plots for $0.4 \leq z < 0.5$. The red markers represent the Salpeter IMF, whereas the black markers represent the Kroupa IMF. The filled in square blocks represent the MILES models, the filled circles represent the gold models and the filled diamonds are for the STELIB Models.

0.5 $\leq z <$ 0.6

Group	Parameters	M11				MaStar	
		$MILES_{ss}$	$MILES_{kr}$	$STELIB_{ss}$	$STELIB_{kr}$	$gold_{ss}$	$gold_{kr}$
(1)	(2)	(3)	(4)	(5)	(6)	(7)	(8)
01	Age (Gyr)	2.45	7.93	2.55	2.55	10.88	10.88
	Met. (dex)	0.21	-0.59	-0.02	-0.02	-1.32	-1.32
	χ^2_{red}	0.443	0.443	0.333	0.332	0.434	0.432
02	Age (Gyr)	2.3	4.9	1.46	1.25	0.02	0.02
	Met. (dex)	0.21	0.13	0.32	0.21	0.35	0.35
	χ^2_{red}	0.424	0.426	0.268	0.268	0.564	0.564
03	Age (Gyr)	5.94	1.38	2.81	3.5	0.02	0.02
	Met. (dex)	0.21	-0.33	0.33	0.13	0.28	0.31
	χ^2_{red}	0.456	0.241	0.382	0.385	0.754	0.747
04	Age (Gyr)	7.56	7.56	1.05	1.46	3.71	2.85
	Met. (dex)	0.35	0.35	0.33	0.32	0.35	0.35
	χ^2_{red}	0.620	0.620	0.252	0.251	0.726	0.700
05	Age (Gyr)	2.79	4.01	2.44	2.44	4.96	4.01
	Met. (dex)	0.32	0.13	0.21	0.21	0.35	0.35
	χ^2_{red}	0.410	0.400	0.334	0.335	0.791	0.830
06	Age (Gyr)	8.02	7.96	3.73	6.99	1.81	3.34
	Met. (dex)	0.35	0.35	0.32	0.35	0.35	-0.05
	χ^2_{red}	0.977	0.965	0.460	0.760	0.654	0.654
07	Age (Gyr)	12.47	12.87	3.45	5.03	0.31	0.31
	Met. (dex)	-0.33	-0.32	0.05	0.35	-0.33	-0.33
	χ^2_{red}	0.635	0.630	0.414	0.628	0.874	0.875
08	Age (Gyr)	6.92	4.99	5.52	0.51	6.43	6.43
	Met. (dex)	0.35	0.35	-0.02	0.35	0.35	0.35
	χ^2_{red}	0.765	0.767	0.401	0.214	1.113	1.115
09	Age (Gyr)	5.51	7.41	4.51	3.73	5.51	5.51
	Met. (dex)	-0.14	-0.29	0.21	0	0.34	0.35
	χ^2_{red}	0.458	0.458	0.470	0.334	0.736	0.747

Table 4.3: FIREFLY results for $0.5 \leq z < 0.6$. *Col. 1*: Group number; *col. 2*: parameters measured by FIREFLY, which are the age in Gyr, metallicity in dex and χ^2_{red} which measures the goodness of the fit. *Col. 3 - 6*: gives the M11 models; *col. 3*: measurements from the MILES model for the Salpeter IMF; *col. 4*: measurements from the MILES model for the Kroupa IMF; *col. 5*: measurements from the STELIB model for the Salpeter IMF and *col. 6*: measurements from the STELIB model for the Kroupa IMF. *Col. 7 - 10*: gives the MaStar models; *col. 7*: measurements from the gold model for the Salpeter IMF; *col. 8*: measurements from the gold model for the Kroupa IMF.



(a) Group 01 (b) Group 02 (c) Group 03 (d) Group 04

(e) Group 05 (f) Group 06 (g) Group 07 (h) Group 08

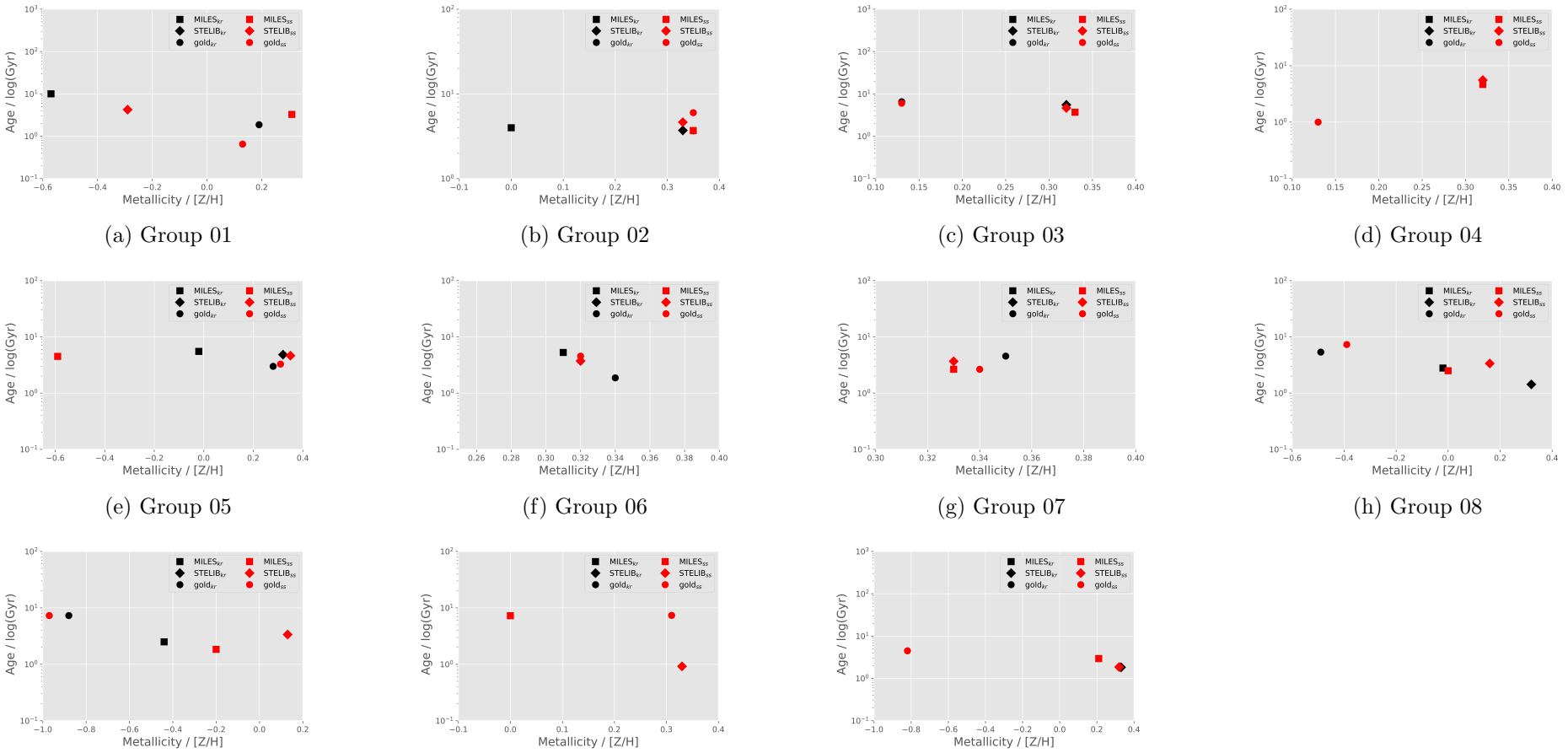
(i) Group 09

Figure 4.4: Age vs. metallicity plots for $0.5 \leq z < 0.6$. The red markers represent the Salpeter IMF, whereas the black markers represent the Kroupa IMF. The filled in square blocks represent the MILES models, the filled circles represent the gold models and the filled diamonds are for the STELIB Models.

0.6 $\leq z <$ 0.7

Group	Parameters	M11				MaStar	
		$MILES_{ss}$	$MILES_{kr}$	$STELIB_{ss}$	$STELIB_{kr}$	$gold_{ss}$	$gold_{kr}$
(1)	(2)	(3)	(4)	(5)	(6)	(7)	(8)
01	Age (Gyr)	3.28	10.04	4.25	4.25	0.65	0.65
	Met. (dex)	0.31	-0.57	-0.29	-0.29	0.13	0.13
	χ^2_{red}	0.418	0.250	0.210	0.210	0.536	0.534
02	Age (Gyr)	3.66	3.98	3.7	3.7	3.66	3.66
	Met. (dex)	0.35	0	0.33	0.33	0.35	0.35
	χ^2_{red}	0.530	0.400	0.372	0.383	0.810	0.810
03	Age (Gyr)	3.69	3.69	4.63	5.52	6.0	6.52
	Met. (dex)	0.33	0.33	0.32	0.32	0.13	0.13
	χ^2_{red}	0.676	0.676	0.466	0.530	1.08	1.08
04	Age (Gyr)	4.64	4.64	5.55	5.55	1	1
	Met. (dex)	0.32	0.32	0.32	0.32	0.13	0.13
	χ^2_{red}	0.703	0.705	0.540	0.540	1.01	1.01
05	Age (Gyr)	4.5	5.51	4.63	4.83	3.28	2.99
	Met. (dex)	-0.59	-0.02	0.35	0.35	0.31	0.28
	χ^2_{red}	0.305	0.595	0.521	0.524	0.906	0.953
06	Age (Gyr)	5.19	5.28	3.73	3.72	4.55	1.87
	Met. (dex)	0.31	0.31	0.32	0.32	0.32	0.34
	χ^2_{red}	0.770	0.774	0.461	0.458	1.048	0.808
07	Age (Gyr)	2.65	2.65	3.68	3.68	4.61	4.55
	Met. (dex)	0.33	0.33	0.33	0.33	0.35	0.34
	χ^2_{red}	0.516	0.516	0.392	0.391	1.01	1.01
08	Age (Gyr)	3.66	2.79	6.44	1.43	5.36	5.36
	Met. (dex)	0	-0.02	0.16	0.32	-0.49	-0.49
	χ^2_{red}	0.407	0.406	0.356	0.210	0.430	0.428
09	Age (Gyr)	1.84	2.5	3.36	3.36	7.3	7.3
	Met. (dex)	-0.2	-0.44	0.13	0.13	-0.97	-0.88
	χ^2_{red}	0.284	0.294	0.215	0.215	0.381	0.380
10	Age (Gyr)	3.86	3.86	2.26	2.26	10.91	10.91
	Met. (dex)	0.13	0.13	-0.29	0.29	-0.61	-0.61
	χ^2_{red}	0.450	0.320	0.201	0.202	0.417	0.417
11	Age (Gyr)	2.94	2.94	1.86	1.83	4.49	4.49
	Met. (dex)	0.21	0.21	0.32	0.33	-0.82	-0.82
	χ^2_{red}	0.442	0.442	0.288	0.285	0.394	0.394

Table 4.4: FIREFLY results for $0.6 \leq z < 0.7$. *Col. 1*: Group number; *col. 2*: parameters measured by FIREFLY, which are the age in Gyr, metallicity in dex and χ^2_{red} which measures the goodness of the fit. *Col. 3 - 6*: gives the M11 models; *col. 3*: measurements from the MILES model for the Salpeter IMF; *col. 4*: measurements from the MILES model for the Kroupa IMF; *col. 5*: measurements from the STELIB model for the Salpeter IMF and *col. 6*: measurements from the STELIB model for the Kroupa IMF. *Col. 7 - 10*: gives the MaStar models; *col. 7*: measurements from the gold model for the Salpeter IMF; *col. 8*: measurements from the gold model for the Kroupa IMF.



(a) Group 01 (b) Group 02 (c) Group 03 (d) Group 04

(e) Group 05 (f) Group 06 (g) Group 07 (h) Group 08

(i) Group 09 (j) Group 10 (k) Group 11

Figure 4.5: Age vs. metallicity plots for $0.6 \leq z < 0.7$. The red markers represent the Salpeter IMF, whereas the black markers represent the Kroupa IMF. The filled in square blocks represent the MILES models, the filled circles represent the gold models and the filled diamonds are for the STELIB Models.

In Figures 4.6, 4.7 and Fig. 4.8, we show the individual age fits of each model along with their associated weighted ages in each redshift bin. The results shown in these figures were calculated using the Kroupa IMF. In Figure 4.6 we show the SSP-equivalent ages when using the MILES stellar library. In Figure 4.7 shows the results from using the STELIB stellar library. And Figure 4.8 shows the results from the MaStar stellar library.

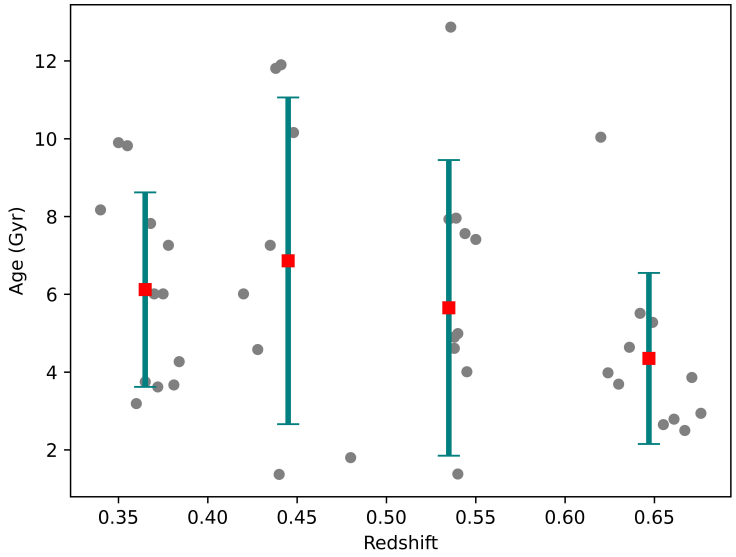


Figure 4.6: Individual fits using MILES model employing the Kroupa IMF (each grey symbol). The red squares represent the weighted ages and their errors (weighted standard deviation).

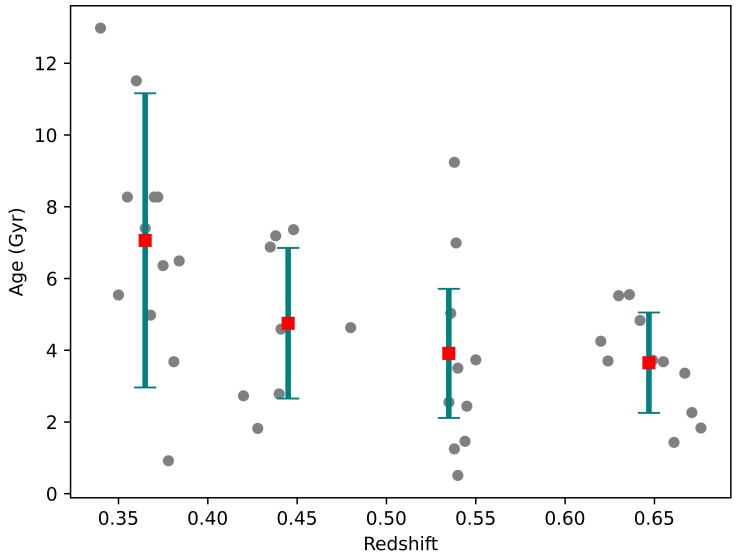


Figure 4.7: Individual fits using STELIB model employing the Kroupa IMF (each grey symbol). The red squares represent the weighted ages and their errors (weighted standard deviation).

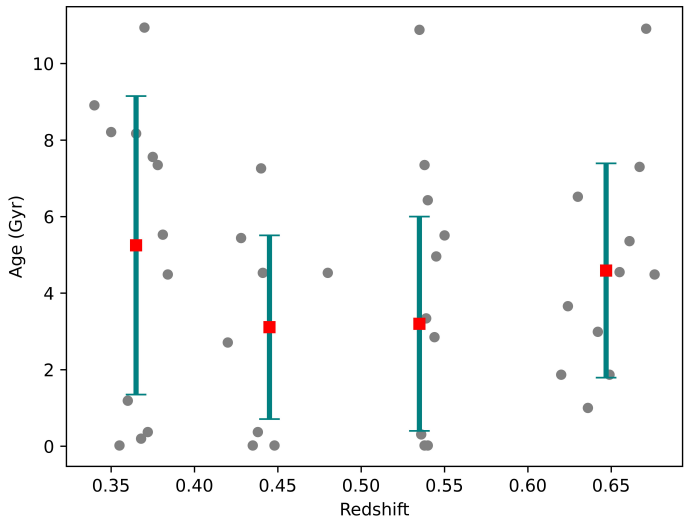


Figure 4.8: Individual fits using MaStar model employing the Kroupa IMF (each grey symbol). The red squares represent the weighted ages and their errors (weighted standard deviation).

In Figures 4.9, 4.10 and Fig. 4.11, we show the individual age fits of each model along with their associated weighted ages in each redshift bin. The results shown in these figures were calculated using the Kroupa IMF. Figure 4.9 are the SSP-equivalent ages when using the MILES stellar library. In Figure 4.10 we show the results from using the STELIB stellar library. And Figure 4.11 shows the results from the MaStar stellar library.

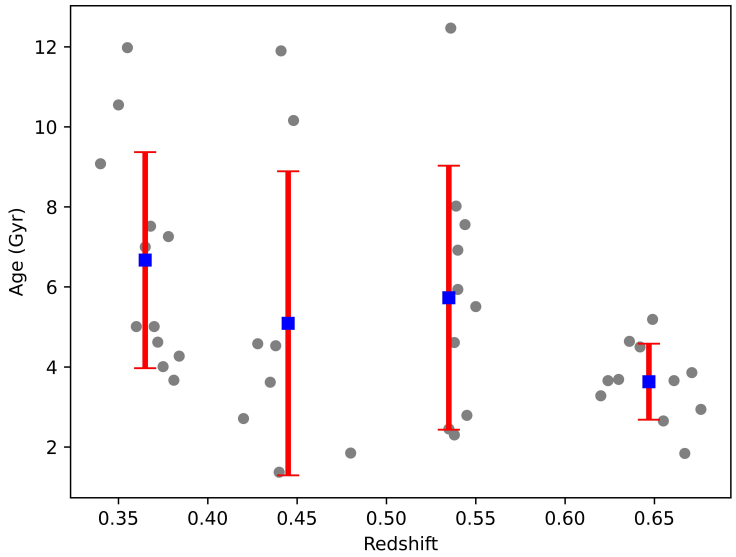


Figure 4.9: Individual fits using MILES model employing the Salpeter IMF (each grey symbol). The blue squares represent the weighted ages and their errors (weighted standard deviation).

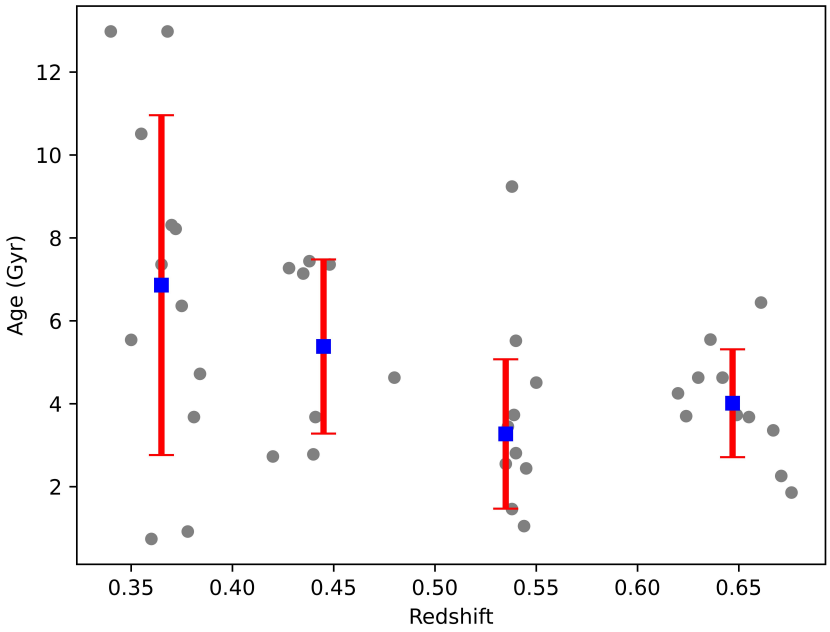


Figure 4.10: Individual fits using STELIB model employing the Salpeter IMF (each grey symbol). The blue squares represent the weighted ages and their errors (weighted standard deviation).

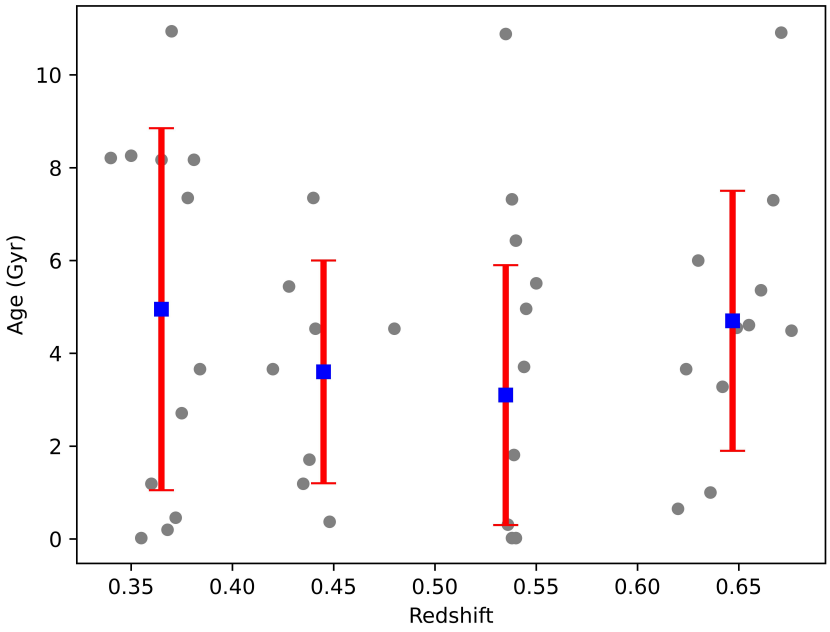


Figure 4.11: Individual fits using MaStar model employing the Salpeter IMF (each grey symbol). The blue squares represent the weighted ages and their errors (weighted standard deviation).

4.2.2 Weighted stellar Ages and Metallicities

Here we present the calculated $\chi^2_{\rm red}$ -weighted stellar ages and metallicities for each of the BEAMS BCG *redshift* intervals, based on the light-weighted ages measured by the respective stellar libraries and IMFs that were used in this analysis (see Section 4.1) and their corresponding $\chi^2_{\rm red}$ statistics. The calculated $\chi^2_{\rm age}$ are important because they provide a singular, statistically significant values for the stacked stellar populations of the BEAMS BCGs. This allows us to conveniently compare the ages of the stellar populations and their metallicities with other available literature. The weighted stellar ages and metallicities can be found in Table 4.5, the σ_v found in this table are from the previous Chapter.

Redshift Interval	Weighted Age_{kr} (Gyr)	Weighted Age_{ss} (Gyr)	$[\text{Z/H}]_{\text{kr}}$ (dex)	$[\text{Z/H}]_{\text{ss}}$ (dex)	Velocity Dispersion (km s^{-1})
$0.3 < z < 0.4$	6.30±1.5	6.40±1.8	0.15±0.28	0.14±0.28	300±17
$0.4 \leq z < 0.5$	4.70±1.5	4.80±1.5	-0.05±0.23	0.03±0.20	249±37
$0.5 \leq z < 0.6$	4.60±1.7	4.40±1.9	0.11±0.42	0.15±0.27	323±80
$0.6 \leq z < 0.7$	4.02±1.6	4.04±1.3	0.05±0.21	0.07±0.28	311±72

Table 4.5: Mean weighted properties of the BEAMS BCGs at different *redshift* intervals. Column 1 shows the redshift interval. Columns 2, 3, 4, 5 and 6 show the weighted ages in units of Gyr, [Z/H] in units of dex, and the velocity dispersion in units of km s^{-1} and their associated errors, respectively. Columns 2 and 4 show the weighted properties for the Kroupa IMF. Columns 3 and 5 show the weighted properties for the Salpeter IMF.

In Figures 4.12 and 4.13 we show the weighted ages of our sample as a function of redshift. On Figure 4.12 we show the weighted ages for the Kroupa IMF and Figure 4.13 shows the weighted ages for the Salpeter IMF.

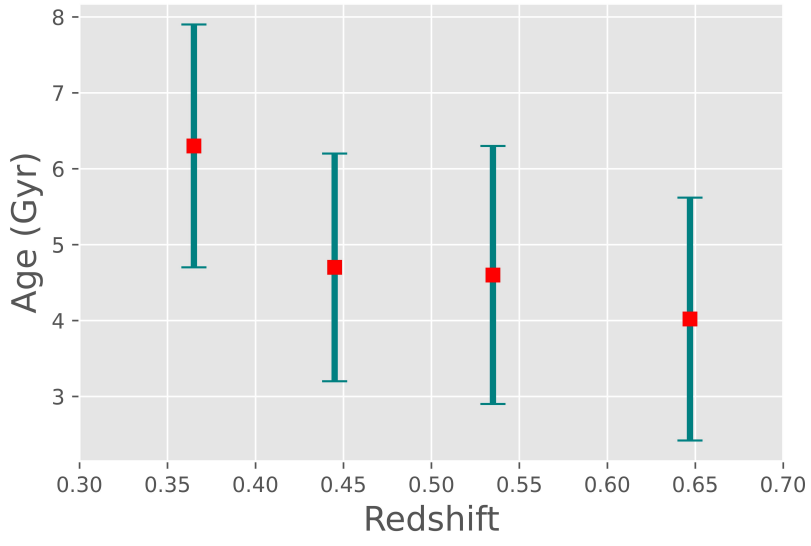


Figure 4.12: Mean weighted ages for our redshift intervals measured in Gyr for the Kroupa IMF and their associated errors.

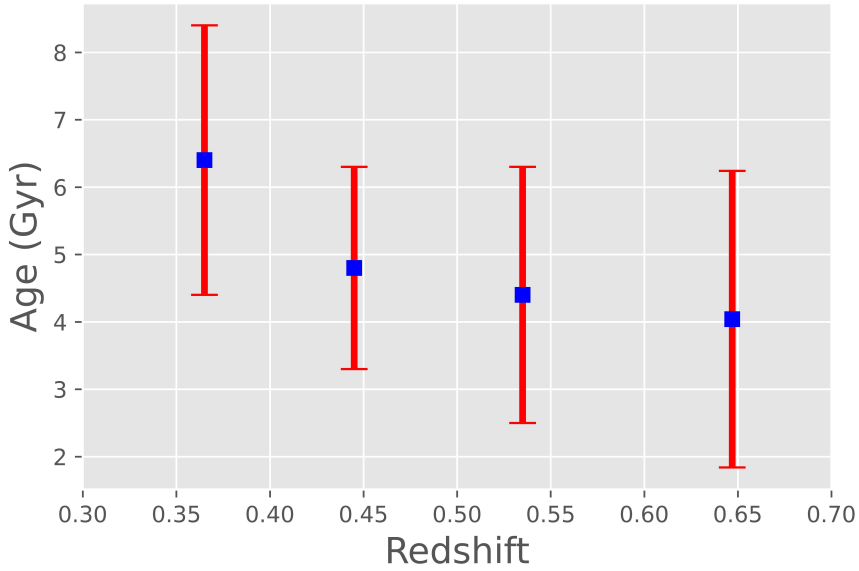


Figure 4.13: Mean weighted ages for our redshift intervals measured in Gyr for the Salpeter IMF and their associated errors.

In Figures 4.14 and 4.15 we show the weighted metallicities of our sample as a function of redshift. On Figure 4.14 we show the weighted metallicities for the Kroupa IMF and Figure 4.15 shows the weighted metallicities for the Salpeter IMF.

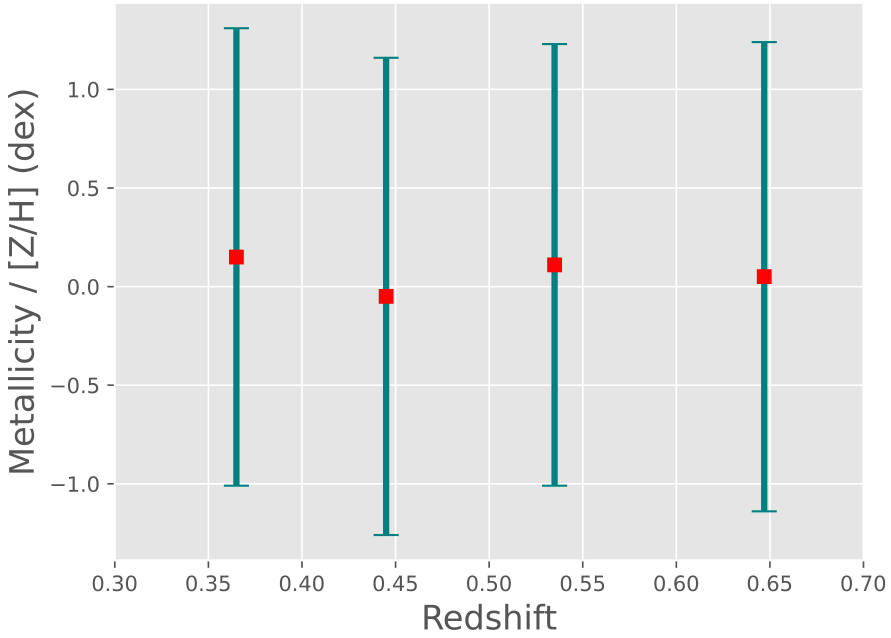


Figure 4.14: Mean weighted metallicities for our redshift intervals measured in dex for the Kroupa IMF and their associated errors.

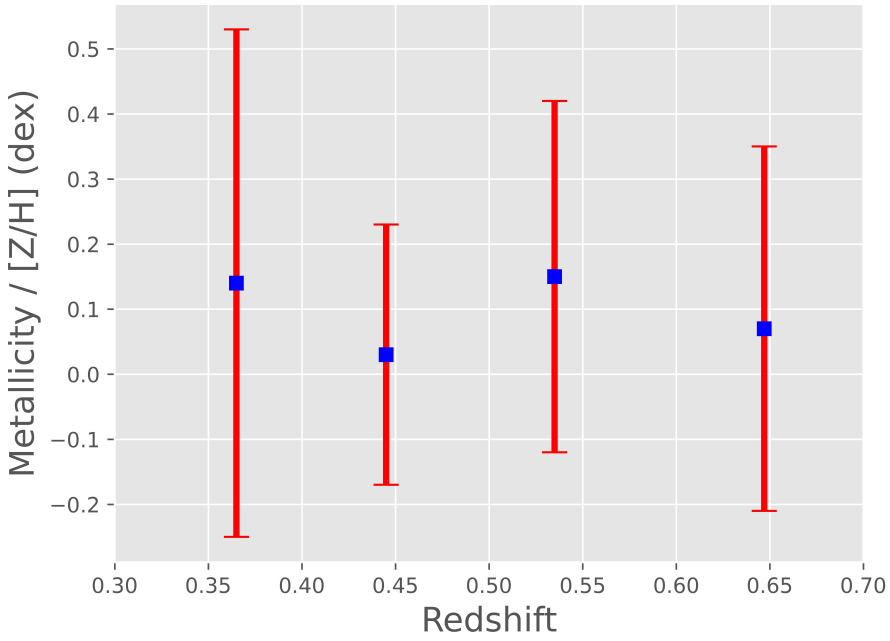


Figure 4.15: Mean weighted metallicities for our redshift intervals measured in dex for the Salpeter IMF and their associated errors.

4.3 Discussion

In this dissertation, we have obtained the ages and metallicities of BCGs as a function of redshift for a sample of brightest cluster galaxies selected from the BEAMS cluster sample covering the redshift range $0.3 < z < 0.8$. In this section the implications of these results will be discussed.

4.3.1 Age-Metallicity relation

In Figures 4.2, 4.3, 4.4 and 4.5, we presented the age-metallicity relation for various groups in different *redshift* intervals of our sample. Worthey et al. (1995) suggested the presence of a metallicity-age relation in type E/S0 galaxies, with younger galaxies appearing to be more metal-rich than older galaxies. However, in the analysis done in this work we do not observe this behaviour in our sample of BCGs. Moreover, when looking at the aforementioned Figures, we can see that the sample of BCGs used in this analysis have a wider distribution of metallicities compared to their age distributions, with a significant variation seen in the metallicities. The M11 models used in this study have a limited representation of low metallicity stars in their parameter space. The STELIB stellar library has an inadequate metallicity coverage for galaxies that have more than solar metallicity. The MILES stellar library also has limited metallicity coverage. It is also important to note that the analysis in this work was performed using a full-spectrum fitting and it was not limited to only fit either metal-sensitive (e.g. $<$ Fe $>$, M_{gb}) indicators or age-sensitive (e.g.

Hβ) indicators. It is therefore reasonable to see a break of the age-metallicity degeneracy in the aforementioned plots.

4.3.2 Age-Redshift relation

In Figures 4.6, 4.7 and 4.8 we presented the age-redshift relationship obtained from using full-spectrum fitting of the stacked spectra of BEAMS BCGs using the MILES, STELIB and MaStar models using the Kroupa IMF. And in the Figures 4.9, 4.10 and 4.11 we presented the age-redshift relationship for the Salpeter. The overall measured SSP equivalent ages are fairly consistent with each other, with the exception of the MaStar models. Each model is able to estimate a well defined and expected age evolution with redshift: we can see that the BCGs become younger as redshift increases, and they follow the ΛCDM cosmology, however for the MaStar model the mean ages of the BCGs get older (almost by $\sim$ 0.5 Gyr) on both IMFs although the error bars are large. Large error bars are also noticeable on the MILES model at $0.4 < z < 0.5$ where a few objects are stacked together to form the combined spectra, and where ages evolve differently: they display more scatter. And for the STELIB model we observe these errors at smaller redshifts $z < 0.4$, and at high redshifts $z > 0.4$, the evolution of the age is more stable. On Figures 4.6, 4.7 and Fig. 4.8, we see that the individual age plots are different in each model when assuming a Kroupa IMF. This behaviour is also observed on Figures 4.9, 4.10 and Fig. 4.11 which assumes a Salpeter IMF. In each individual fitting of the models, we can see a few ages approaching the boundary limitation, which in this case is the age of the Universe. These ages have contributed less in the measured weighted mean ages. This number is significantly higher in the ages that were derived from using the STELIB models. The estimated ages in this model are almost scattered around intermediate ages ($\sim$ 3.5 - 7 Gyr) over the entire redshift. Moreover, with the other two models, the spread of the estimated ages are mostly from 2 Gyr to 5 Gyr without considering the ages near the edge.

4.3.3 Age-Dating

In Figures 4.12, 4.13, 4.14 and Fig. 4.15 we presented the results of our analysis of the weighted ages and metallicities as a function of redshift. The data presented in these figures is also provided in Table 4.5. If we assume that BCGs are passively evolving systems, their ages can, potentially, be used to constrain the expansion of the Universe (see Ratsimbazafy et al., 2017, and references therein). Overall, these trends are consistent with expectations and can provide important constraints on cosmology (via the age–redshift relation). In Figures 4.12 and 4.13 we can see that the weighted age of our sample decreases as the redshift gets bigger and bigger. We also note little evolution in the shape of [Z/H] as can be observed on Figures 4.14 and 4.15. The age–dating of galaxies is an important topic in the study of the galaxy evolution. During the last few decades, this concept has been widely exploited by the creation of synthetic stellar population tools (Ratsimbazafy et al., 2017).

We compare the weighted ages of our BCG sample with 16 luminous red galaxies (LRGs) studied by Ratsimbazafy et al. (2017) which are shown in Figure 4.16. The sample of LRGs studied by Ratsimbazafy et al. (2017) were taken from the 2dF–SDSS LRG and QSO (2SLAQ) catalogue (Cannon et al., 2006) and the MegaZ–LRG photometric redshift catalogue (Collister et al., 2007) and lie between the redshift range $0.35 < z < 0.60$. Ratsimbazafy et al. (2017) used the University of Lyon Spectroscopic analysis Software (ULySS; Koleva et al., 2009) to recover ages for their sample with a Chabrier IMF using SSP models that are based on GALAXEV models (Bruzual & Charlot, 2003, hereafter BC03).

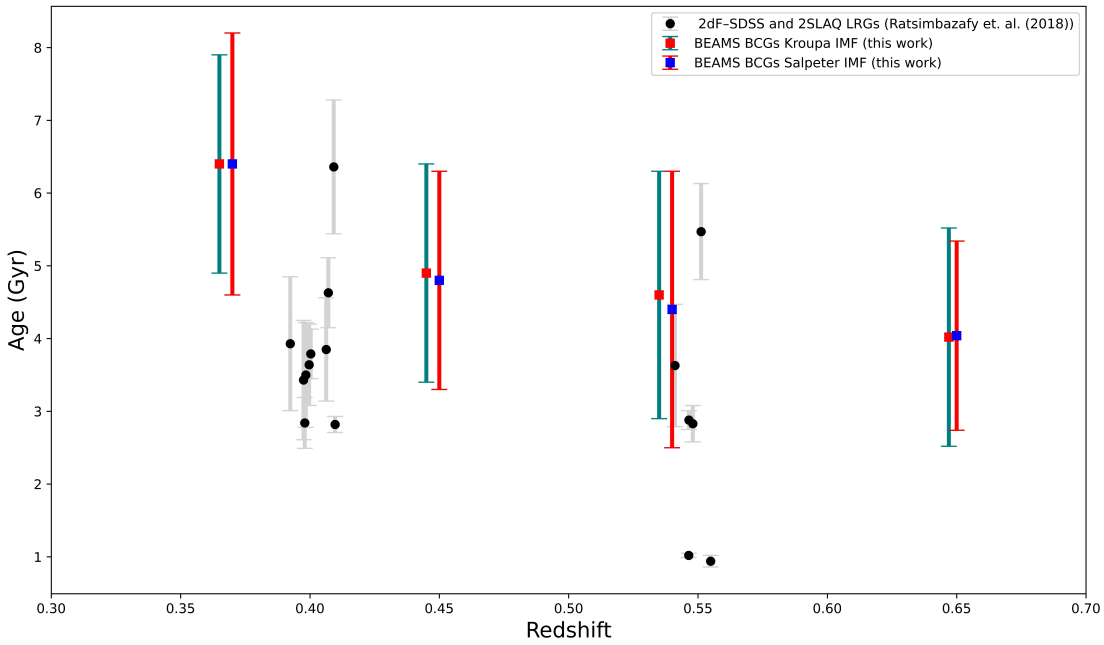


Figure 4.16: Different SSP equivalent ages derived from full spectrum fitting. The blue filled squares and the red filled squares are the weighted ages of the BEAMS BCGs from our study for both the Kroupa and Salpeter IMFs. The black filled circles are the results of Ratsimbazafy et al. (2017), who used the BC03 models and a Chabrier IMF showing the SSP equivalent ages as a function of redshift. The errors of their ages were derived from the covariance matrix.

From Figure 4.16, we can see that the BEAMS BCGs have much higher weighted ages in both IMFs compared to those of Ratsimbazafy et al. (2017). This may be due to the stacking of individual galaxies in our analysis and having a larger sample compared to their sample. We can also see that on average the Kroupa IMF provides higher ages compared to those that are calculated form using the Salpeter IMF. It is also important to take into consideration the different ingredients and settings used by each model to build their parameter grids. If the measured light–weighted SSP equivalent ages represents the ages of the galaxies, we can use these estimated ages to calculate the Hubble parameter via the difference in ages associated with the corresponding difference in redshifts. Ratsimbazafy et al. (2017) also noted that the model dependence of these ages provides some changes

when estimating the Hubble parameter. We provide these relationships here, to show that BCGs can be used to measure the Hubble parameter and also constrain cosmological parameters.

Chapter 5

Summary and future work

In this dissertation, long-slit spectra of 89 BEAMS BCGs covering the redshift range $0.3 < z < 0.8$, observed by SALT, were analysed using full-spectrum fitting. These galaxies were stacked together in different redshift bins and their spectra was fitted to SSP synthetic spectra to recover their ages and metallicities, in order to study their evolution as a function of redshift.

The results of our analysis can be summarised as follows:

- In Chapter 3, we performed a kinematical analysis on our BCG sample using stacked spectra with respect to redshift to measure their velocity dispersions. This result allowed us to perform an analysis of their stellar population parameters.
- In Chapter 4, we measured the stellar population parameters, age and metallicity of our sample from full-spectrum fitting using three different stellar population libraries, namely the MILES, STELIB and the MaStar model.
- In the age-metallicity relation fits of our sample we found that the sample is spread more in metallicity than it is on age and some models are often outliers indicating large systematic differences caused by the different model ingredients.
- We also do not observe a direct relationship between the measured ages and the metallicities as suggested by Worthey et al. (1995). Our plots of age vs metallicity indicate that the full-spectrum fitting used on the SALT data, in this wavelength range breaks the age-metallicity degeneracy.
- The individual models are able to estimate well defined and expected ages that evolve with redshift. The observed BCGs become younger as the redshift increases, and they follow the ΛCDM cosmology.

Our measurements can now be used for further studies, e.g., the ages of our BCG sample can be used to measure the expansion rate of the Universe $H(z)$ as well constraining the cosmological parameters.

In the future, we hope to utilise the entire BEAMS BCG data, to conduct an analysis of the stellar population parameters of the sample. These measurements will then be used to study the age-redshift relation over an extended redshift range. We also hope to make use of this data to physically measure the Hubble parameter $H(z)$, these measurements will then contribute as an extension of the number of the observational $H(z)$ data. We will also see how comparable it is to the existing value in literature, which is mostly found by using LRGs as the standard candles. There is also the issue of systematic errors between the various SSP models that are used that also remains to be the subject of discussion.

"The mindset isn't about seeking a result — it's more about the process of getting to that result. It's about the journey and the approach. It's a way of life. I do think that it's important, in all endeavors, to have that mentality".

— Kobe Bean Bryant, The Mamba Mentality: How I Play.

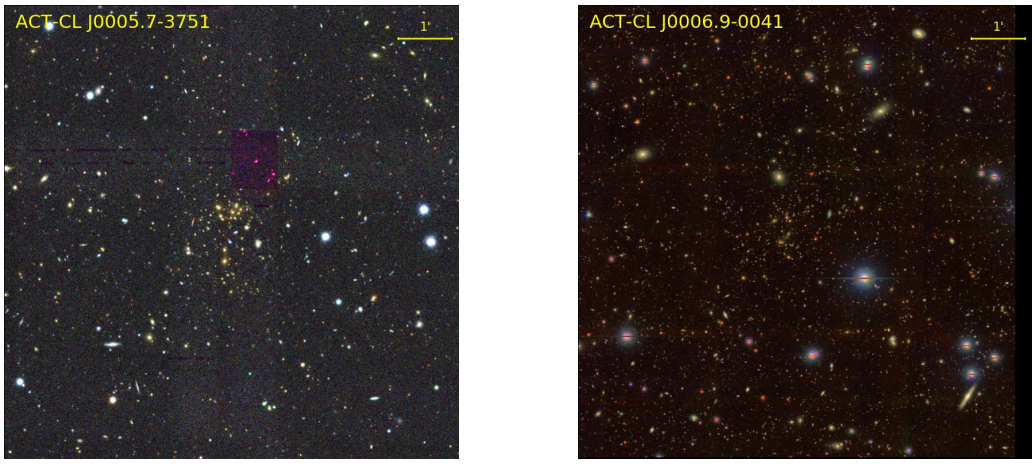
Appendices

Appendix A

BEAMS BCGs

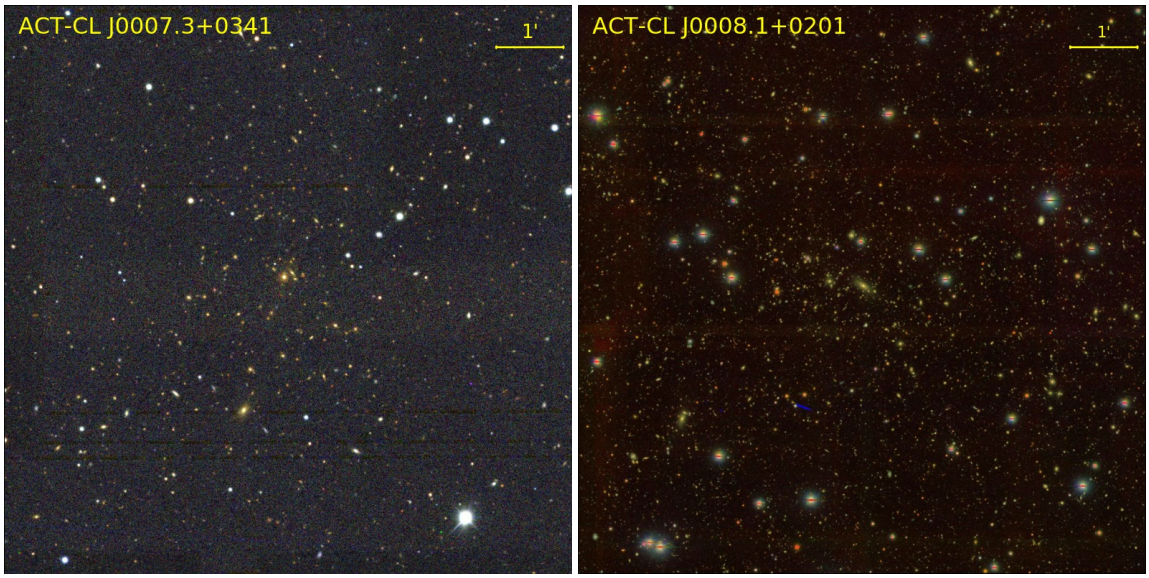
In this Appendix we provide the list of DES Imaging as mentioned in Chapter 2.

A.1 DES images



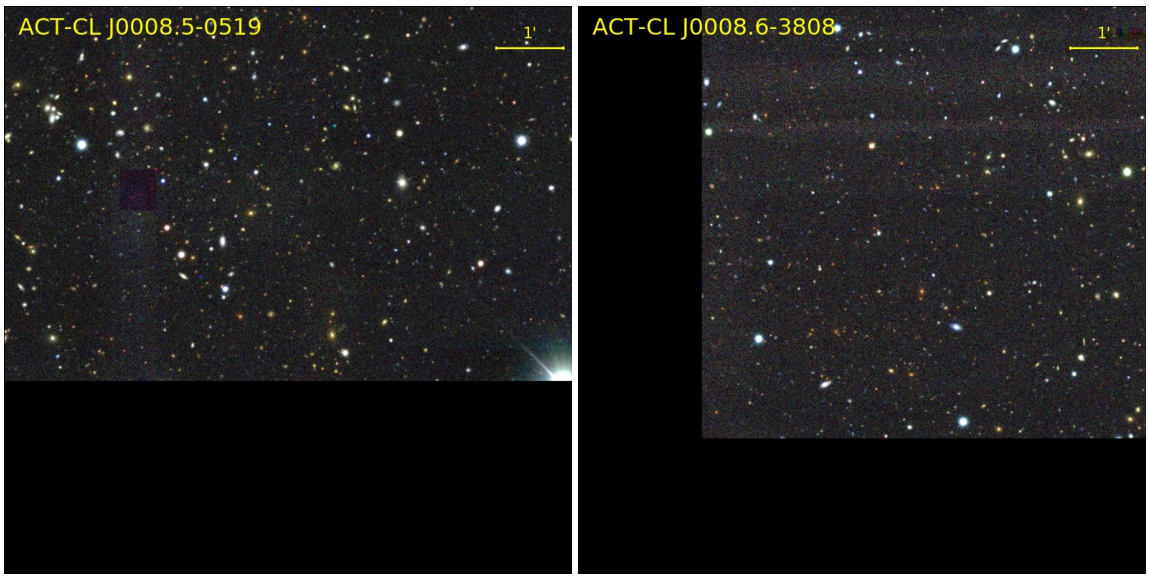
(a) (b)

Figure A.1.1: DES cluster images of (a) ACT-CL J0005.7-3751 and (b) ACT-CL J0006.9-0041.



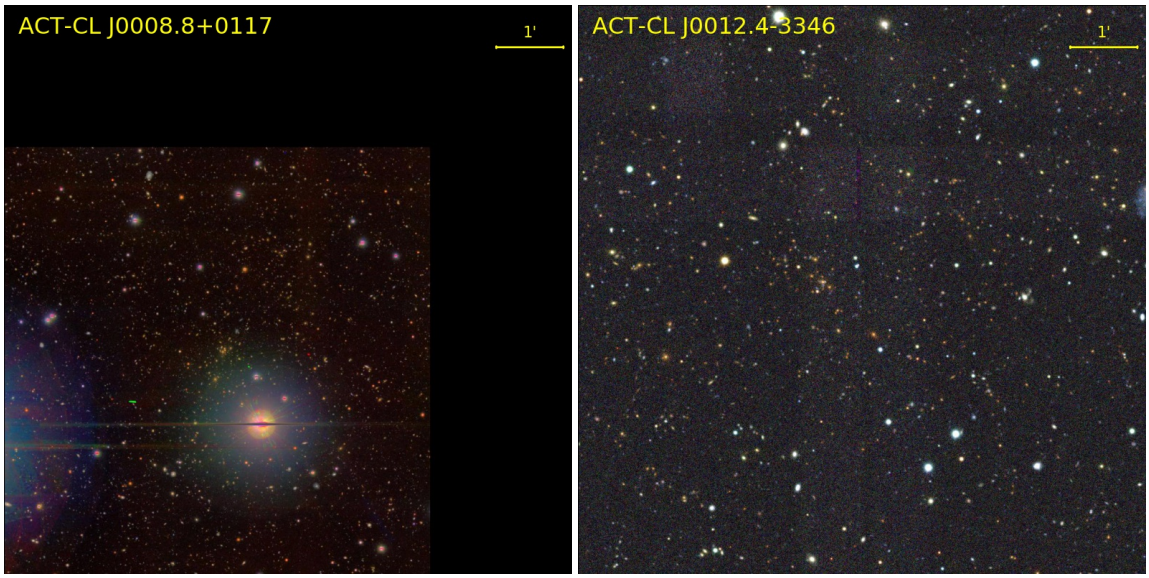
(a) (b)

Figure A.1.2: DES cluster images of (a) ACT-CL J0007.3+0341 and (b) ACT-CL J0008.1+0201.



(a) (b)

Figure A.1.3: DES cluster images of (a) ACT-CL J0008.5-0519 and (b) ACT-CL J0008.6-3808.



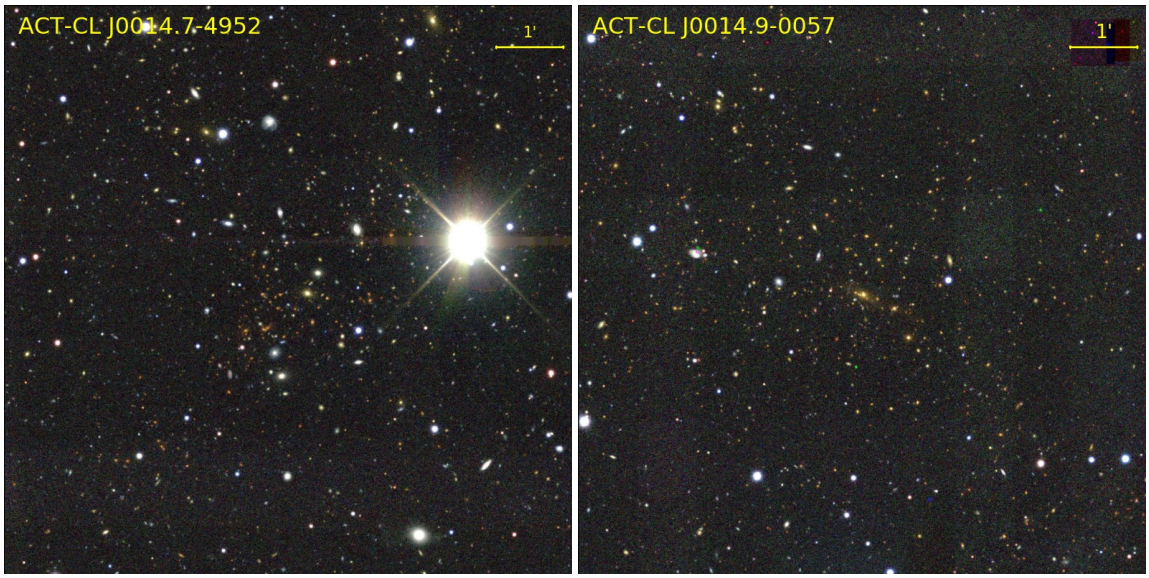
(a) (b)

Figure A.1.4: DES cluster images of (a) ACT-CL J0008.8+0117 and (b) ACT-CL J0012.4-3346.



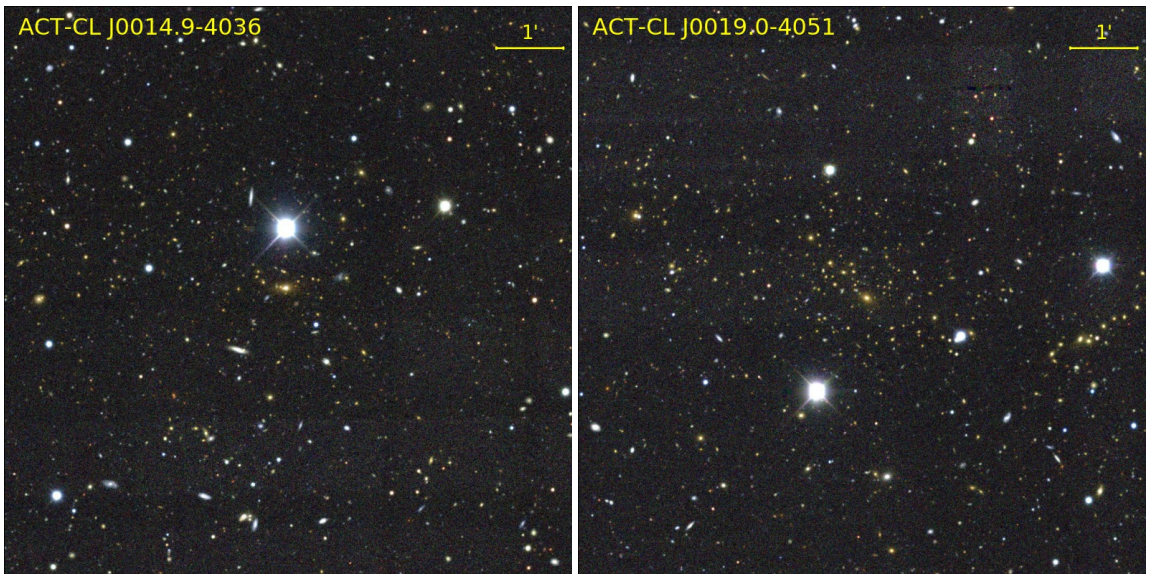
(a) (b)

Figure A.1.5: DES cluster images of (a) ACT-CL J0013.2-4906 and (b) ACT-CL J0014.0+0227.



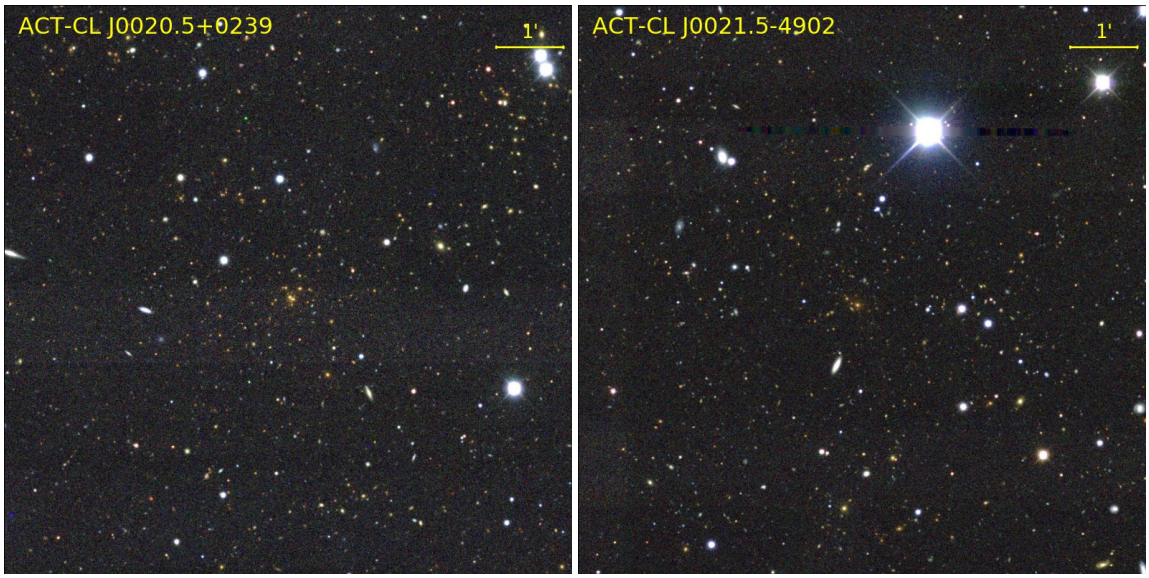
(a) (b)

Figure A.1.6: DES cluster images of (a) ACT-CL J0014.7-4952 and (b) ACT-CL J0014.9-0057.



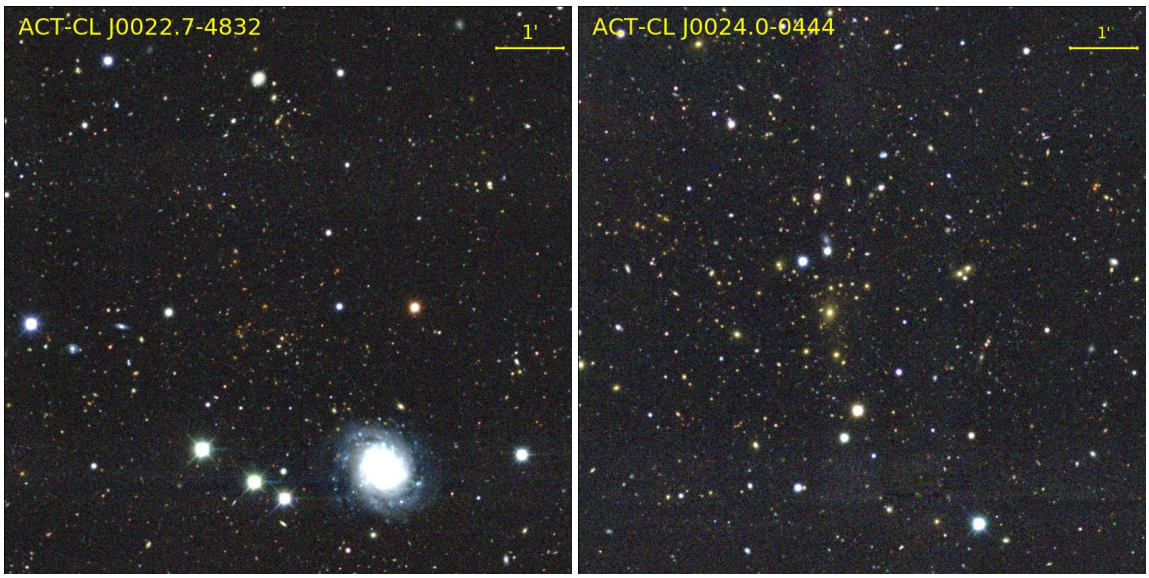
(a) (b)

Figure A.1.7: DES cluster images of (a) ACT-CL J0014.9-4036 and (b) ACT-CL J0019.0-4051.



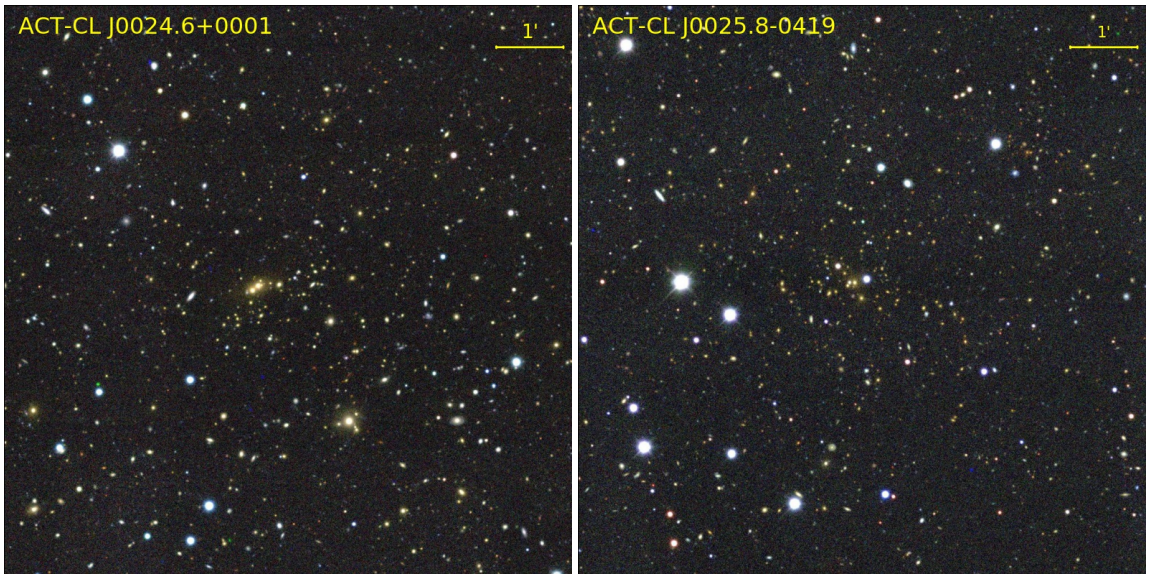
(a) (b)

Figure A.1.8: DES cluster images of (a) ACT-CL J0020.5+0239 and (b) ACT-CL J021.5-4902.



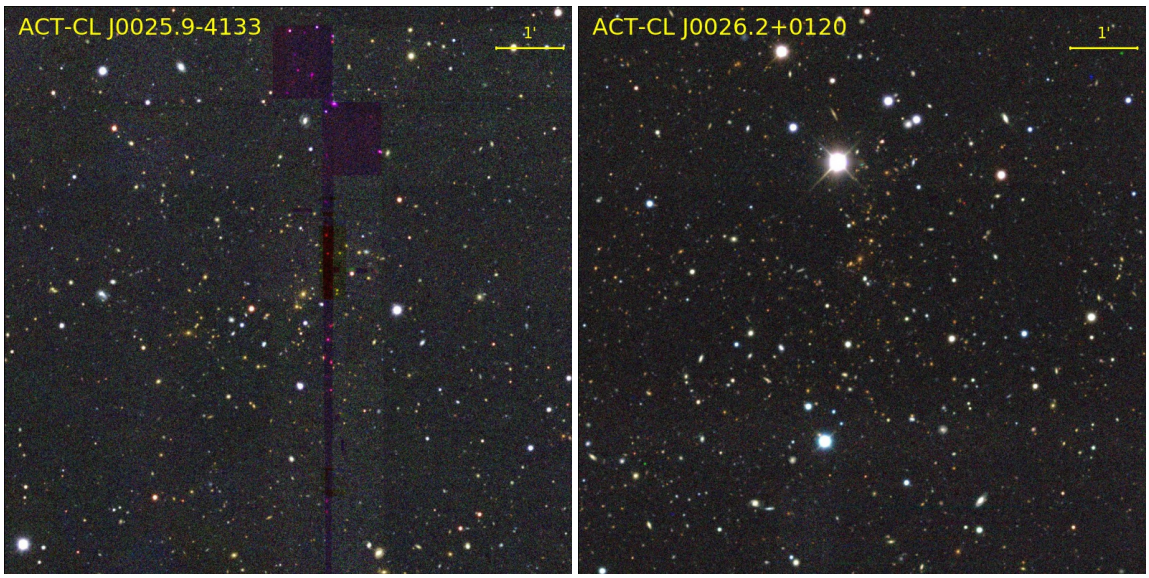
(a) (b)

Figure A.1.9: DES cluster images of (a) ACT-CL J0022.7-4832 and (b) ACT-CL J0024.0-0444.



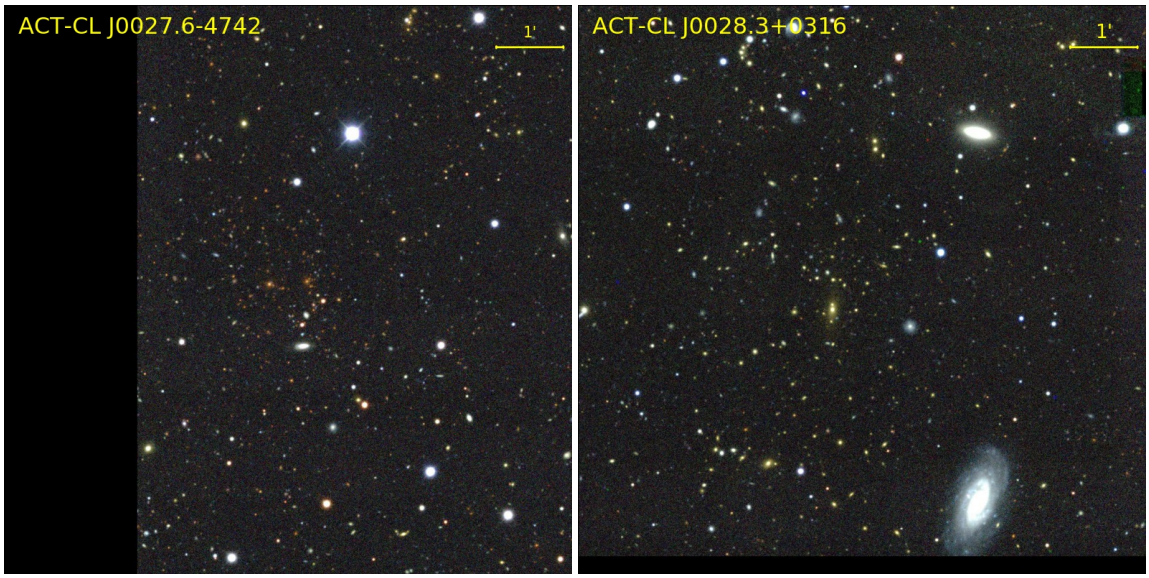
(a) (b)

Figure A.1.10: DES cluster images of (a) ACT-CL J0024.6+0001 and (b) ACT-CL J0025.8-0419.



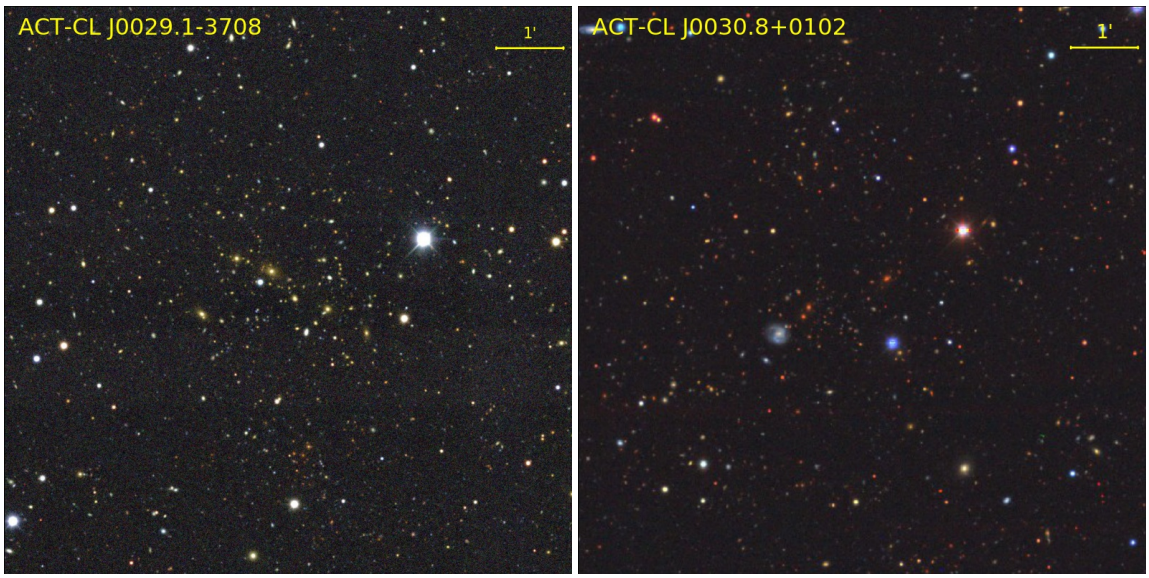
(a) (b)

Figure A.1.11: DES cluster images of (a) ACT-CL J0025.9-4133 and (b) ACT-CL J0026.2+0120.



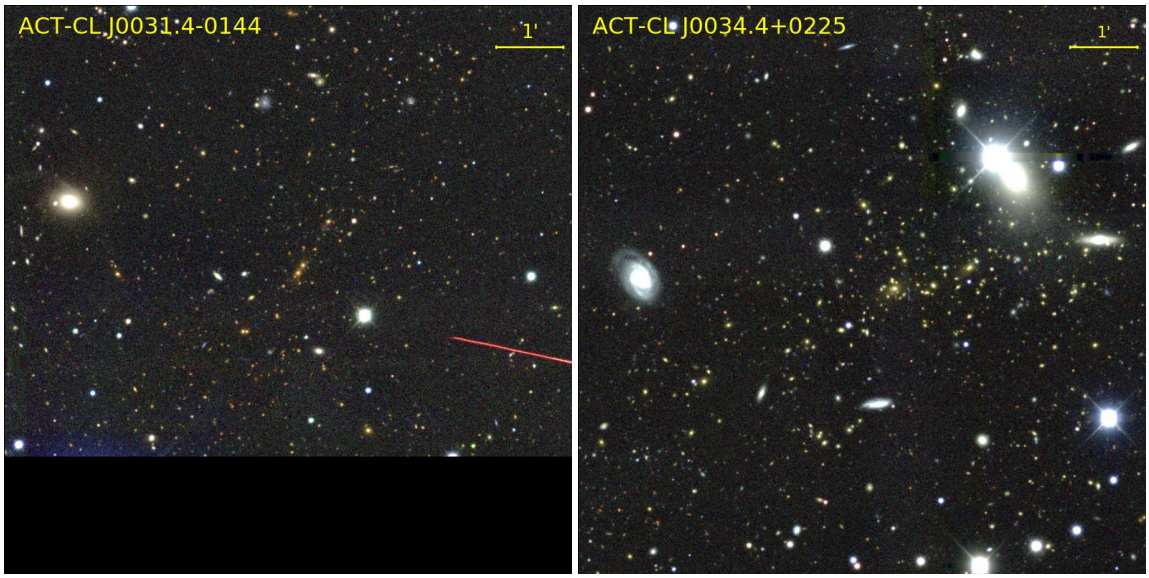
(a) (b)

Figure A.1.12: DES cluster images of (a) ACT-CL J0027.6-4742 and (b) ACT-CL J0028.3+0316.



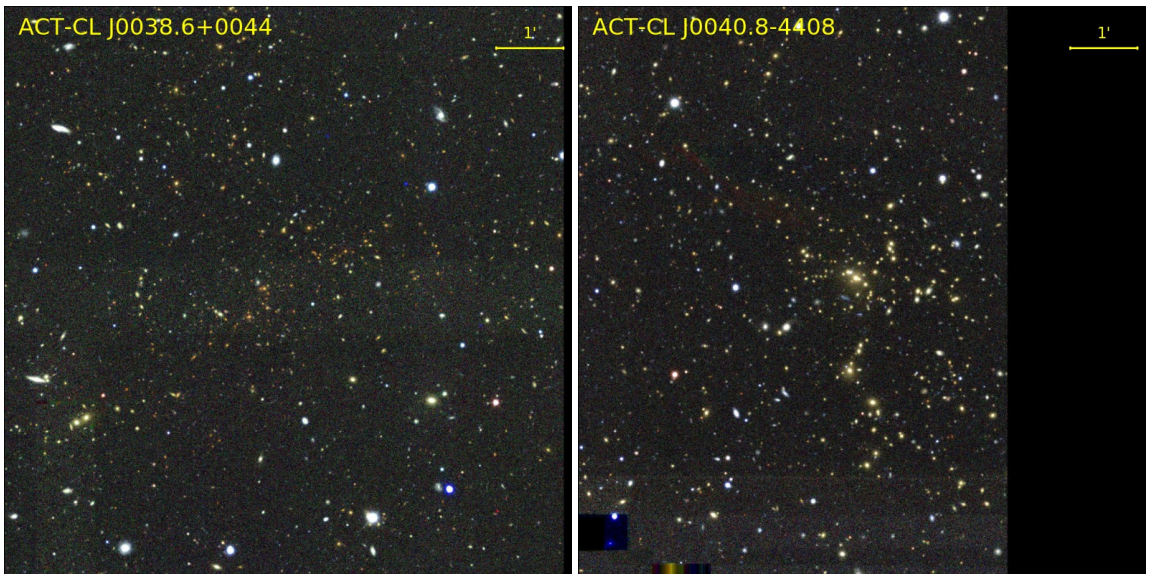
(a) (b)

Figure A.1.13: DES cluster images of (a) ACT-CL J0029.1-3708 and (b) ACT-CL J0030.8+0102.



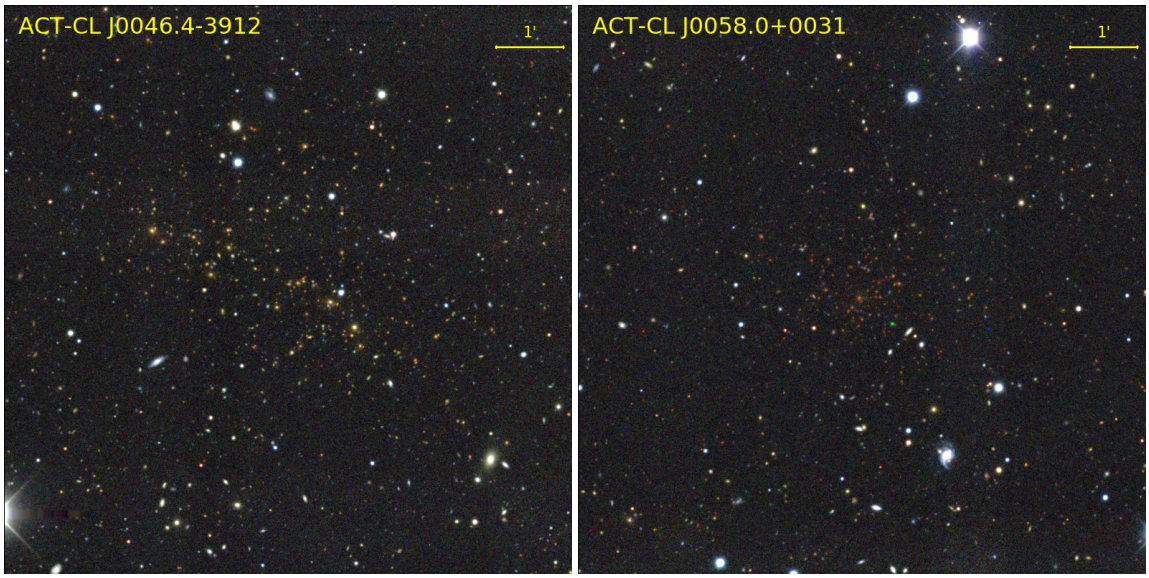
(a) (b)

Figure A.1.14: DES cluster images of (a) ACT-CL J0031.4-0144 and (b) ACT-CL J0034.4.0+0225.



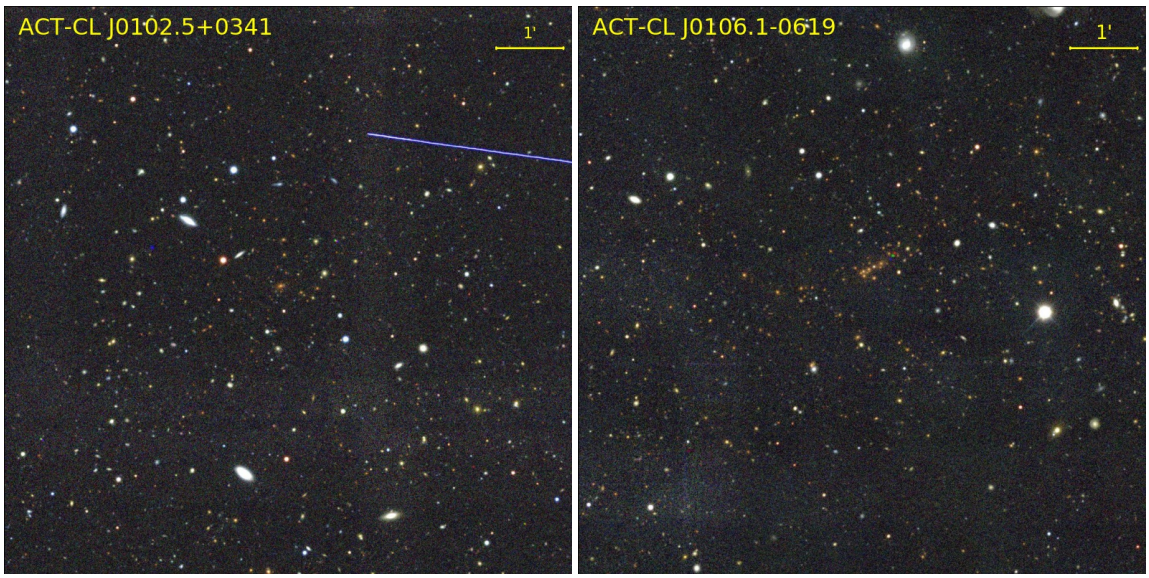
(a) (b)

Figure A.1.15: DES cluster images of (a) ACT-CL J0038.6+0044 and (b) ACT-CL J0040.8-4408.



(a) (b)

Figure A.1.16: DES cluster images of (a) ACT-CL J0046.4-3912 and (b) ACT-CL J0058.0+0031.



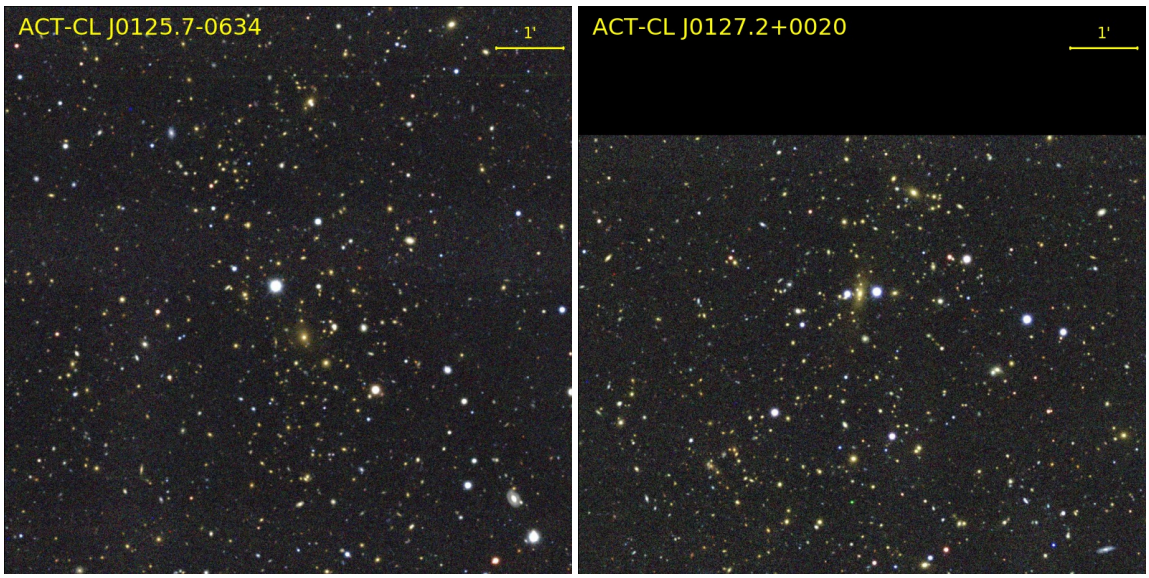
(a) (b)

Figure A.1.17: DES cluster images of (a) ACT-CL J0102.5+0341 and (b) ACT-CL J0106.1-0619.



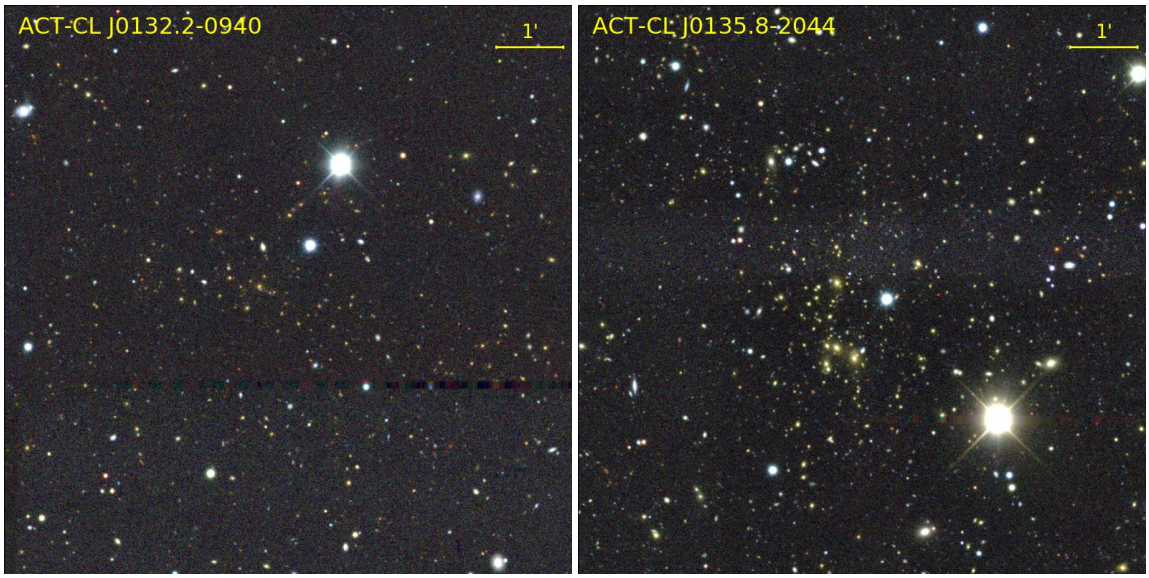
(a) (b)

Figure A.1.18: DES cluster images of (a) ACT-CL J0108.0+0251 and (b) ACT-CL J0119.9+0055.



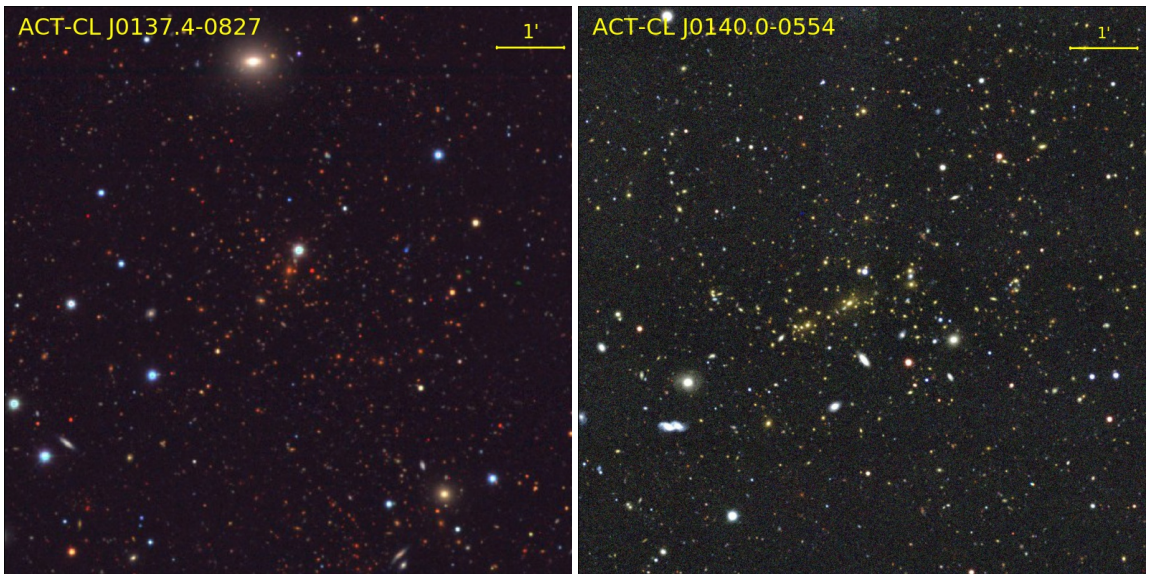
(a) (b)

Figure A.1.19: DES cluster images of (a) ACT-CL J0125.7-0634 and (b) ACT-CL J0127.2+0020.



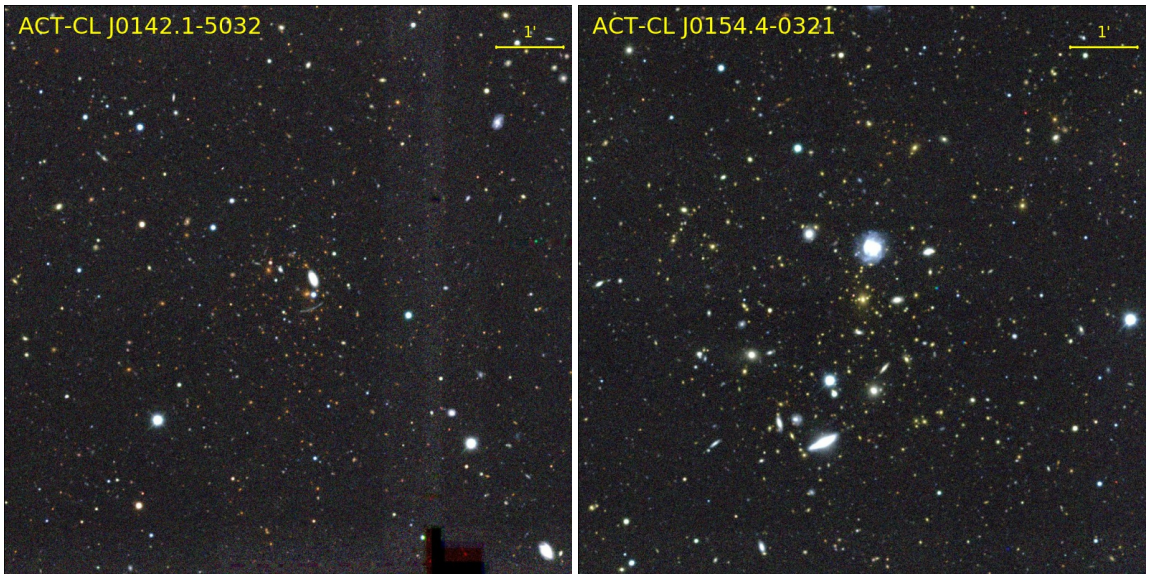
(a) (b)

Figure A.1.20: DES cluster images of (a) ACT-CL J0132.2-0940 and (b) ACT-CL J0135.8-2044.



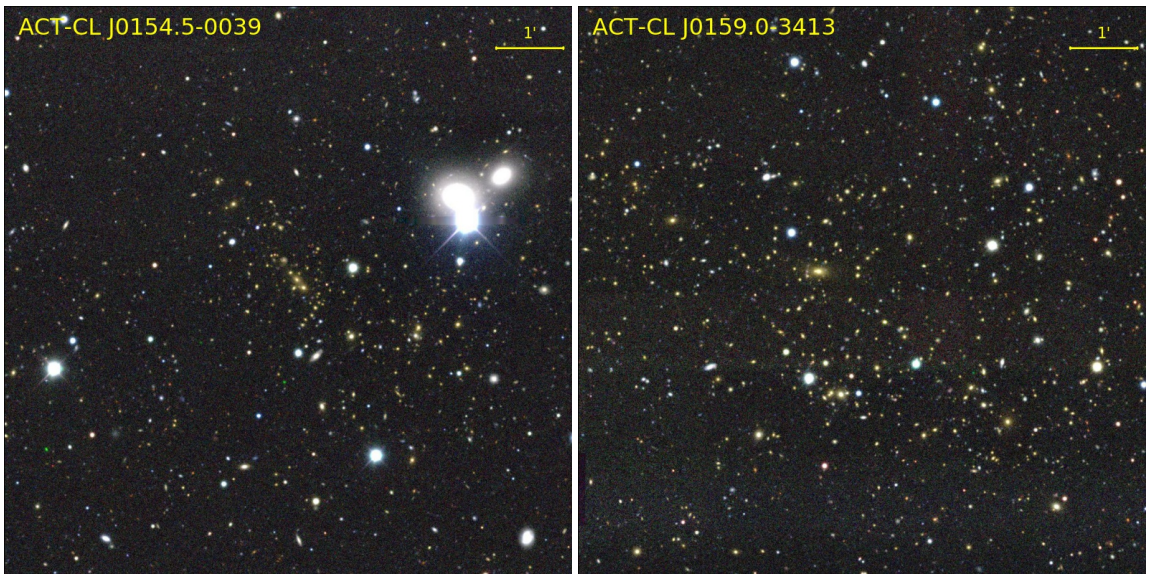
(a) (b)

Figure A.1.21: DES cluster images of (a) ACT-CL J0137.4-0827 and (b) ACT-CL J0140.0-0554.



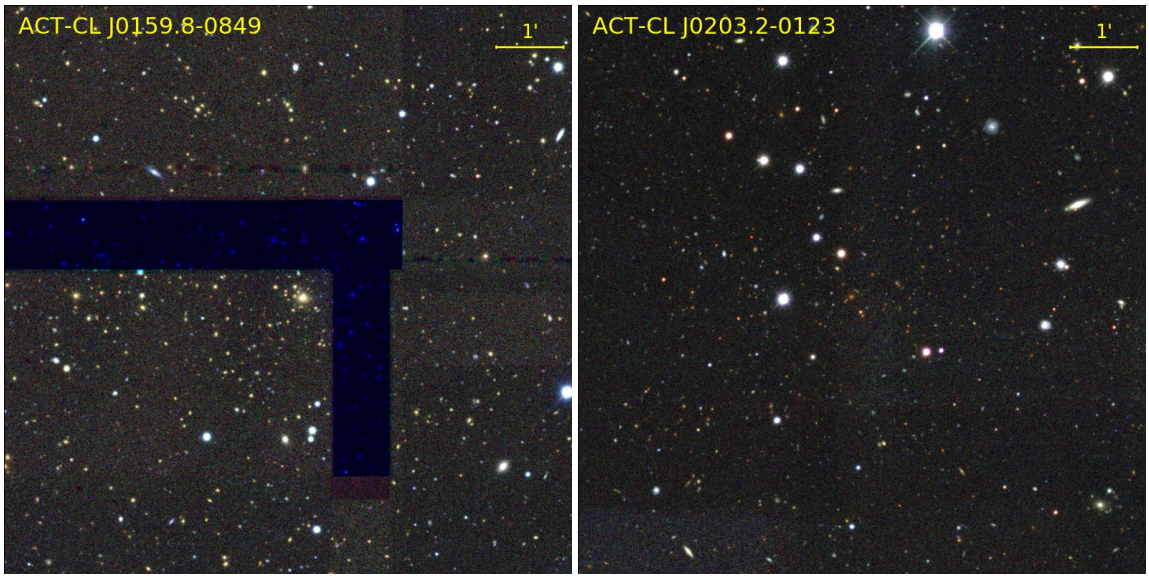
(a) (b)

Figure A.1.22: DES cluster images of (a) ACT-CL J0142.1-5032 and (b) ACT-CL J0154.4-0321.



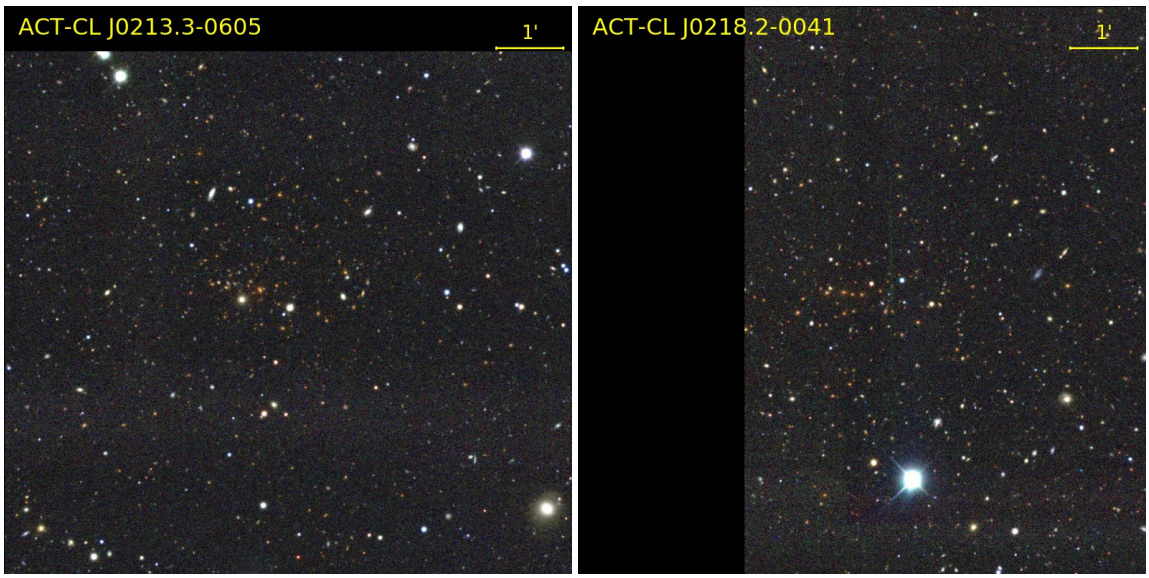
(a) (b)

Figure A.1.23: DES cluster images of (a) ACT-CL J0154.5-0039 and (b) ACT-CL J0159.0-3413.



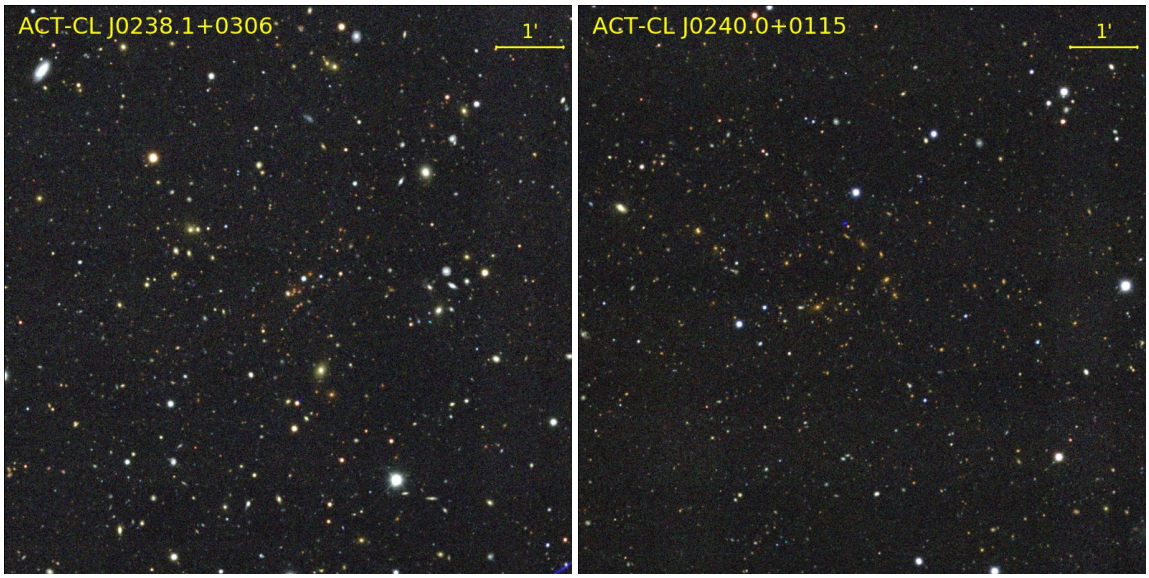
(a) (b)

Figure A.1.24: DES cluster images of (a) ACT-CL J0159.8-0849 and (b) ACT-CL J0203.2-0123.



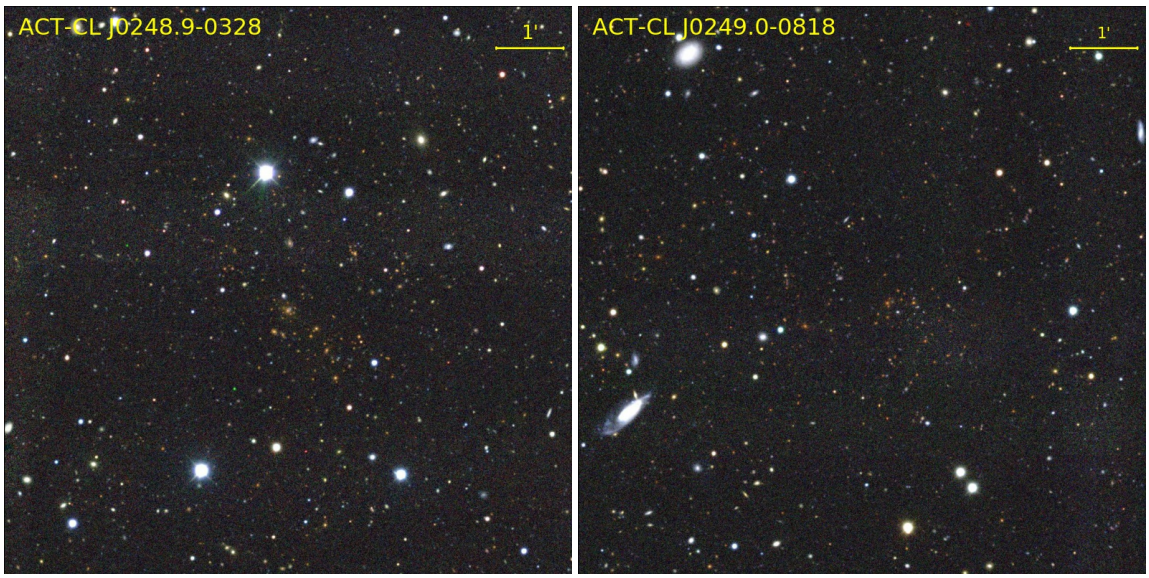
(a) (b)

Figure A.1.25: DES cluster images of (a) ACT-CL J0213.3-0605 and (b) ACT-CL J0218.2-0041.



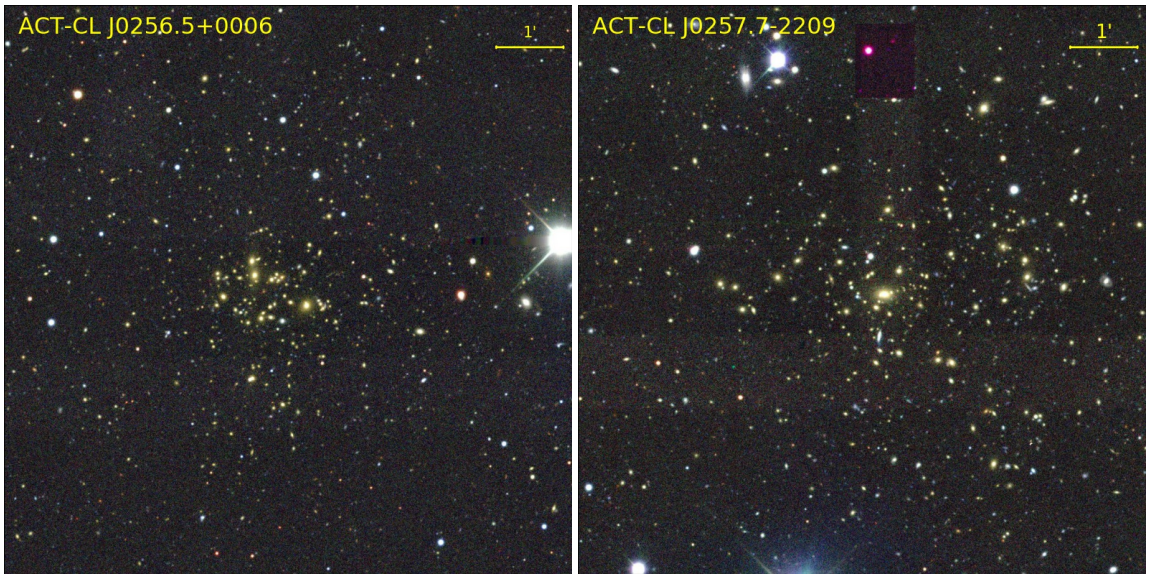
(a) (b)

Figure A.1.26: DES cluster images of (a) ACT-CL J0238.1+0306 and (b) ACT-CL J0240.0+0115.



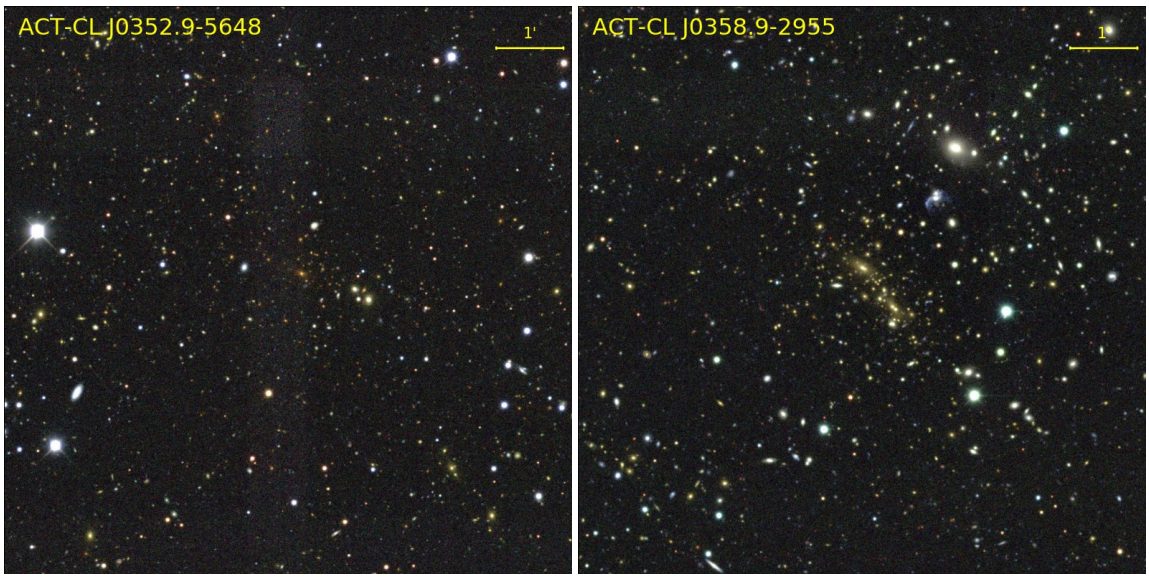
(a) (b)

Figure A.1.27: DES cluster images of (a) ACT-CL J0248.9-0328 and (b) ACT-CL J0249.0-0818.



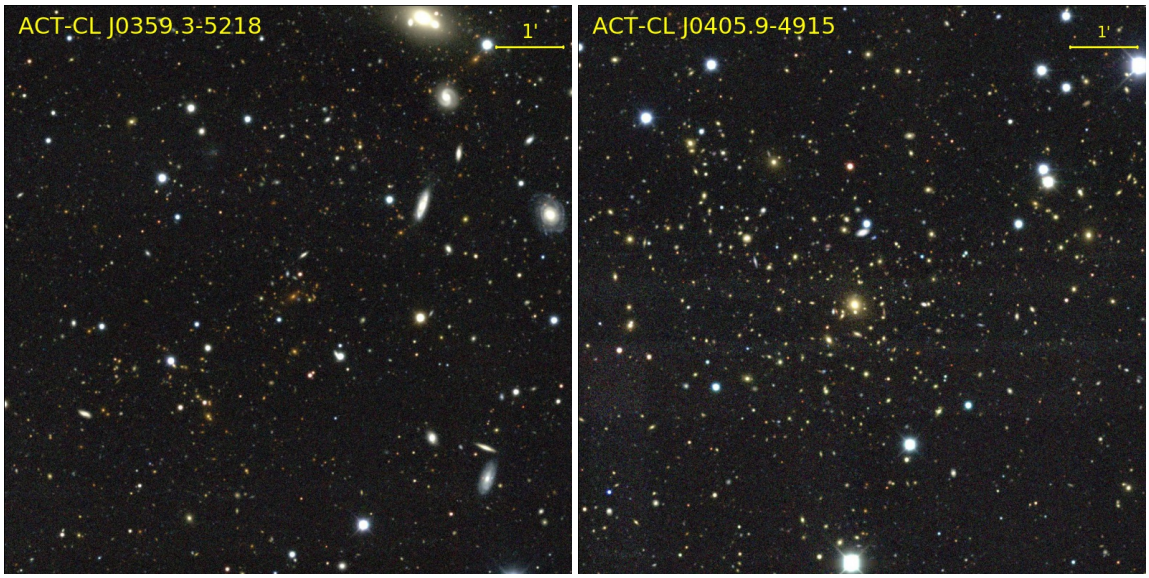
(a) (b)

Figure A.1.28: DES cluster images of (a) ACT-CL J0256.5+0006 and (b) ACT-CL J0257.7.1-2209.



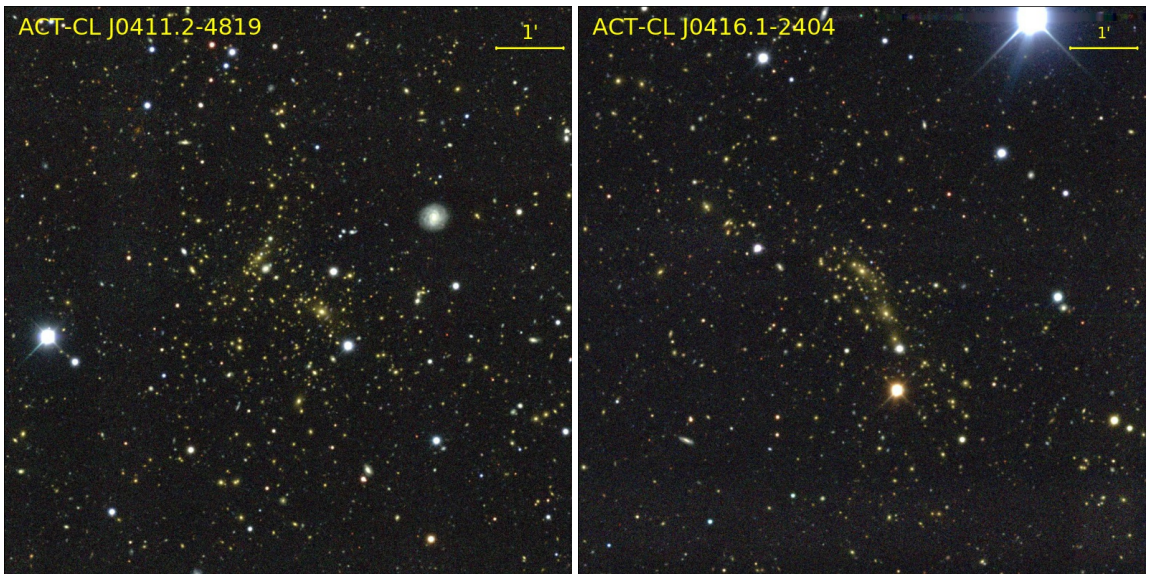
(a) (b)

Figure A.1.29: DES cluster images of (a) ACT-CL J0352.9-5648 and (b) ACT-CL J0358.9-2955.



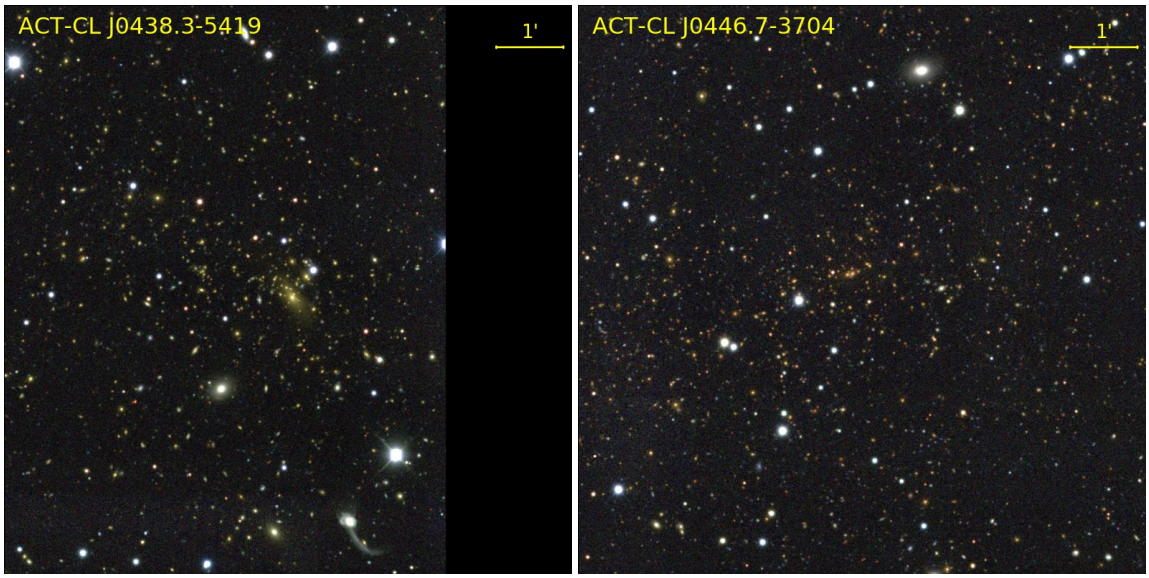
(a) (b)

Figure A.1.30: DES cluster images of (a) ACT-CL J0359.3-5218 and (b) ACT-CL J0405.9-4915.



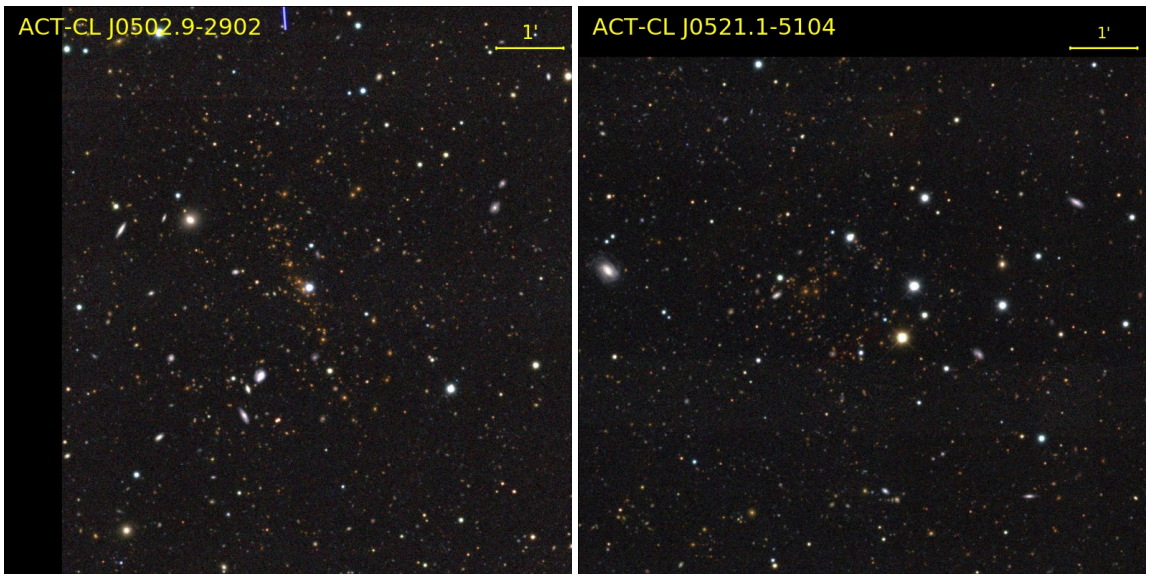
(a) (b)

Figure A.1.31: DES cluster images of (a) ACT-CL J0411.2-4819 and (b) ACT-CL J0416.1-2404.



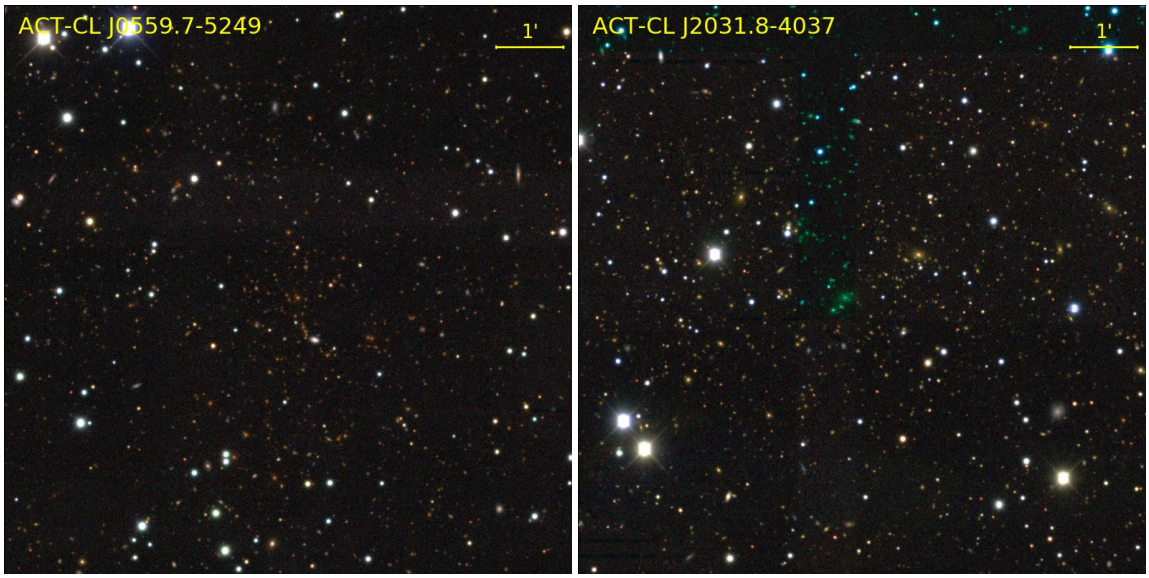
(a) (b)

Figure A.1.32: DES cluster images of (a) ACT-CL J0438.3-5419 and (b) ACT-CL J0446.7-3703.



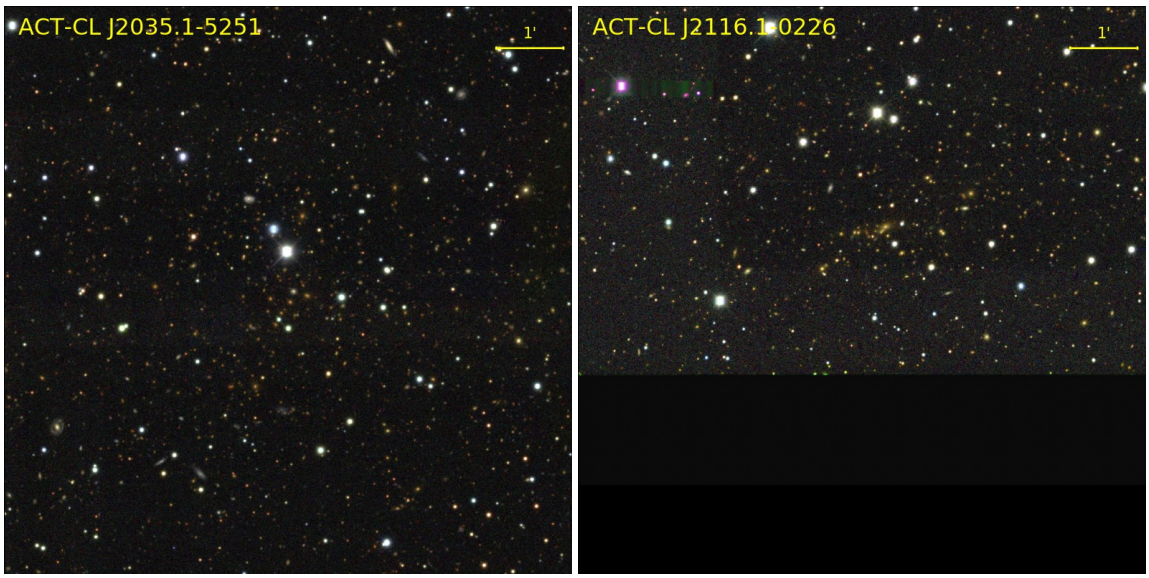
(a) (b)

Figure A.1.33: DES cluster images of (a) ACT-CL J0502.9+2902 and (b) ACT-CL J0521.1-5104.



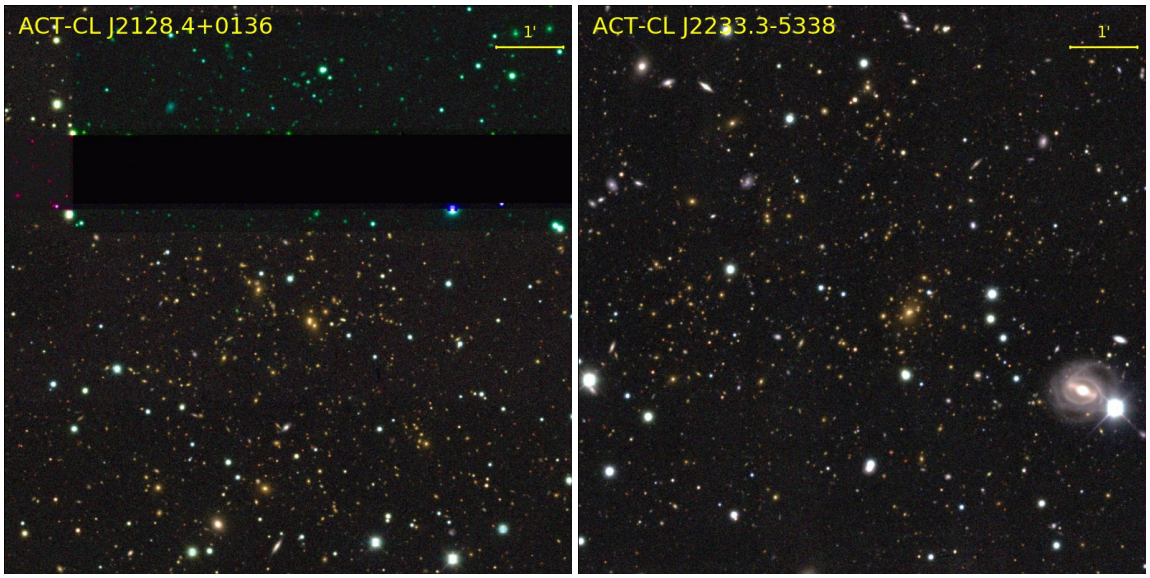
(a) (b)

Figure A.1.34: DES cluster images of (a) ACT-CL J0559.7-5249 and (b) ACT-CL J2031.8-4037.



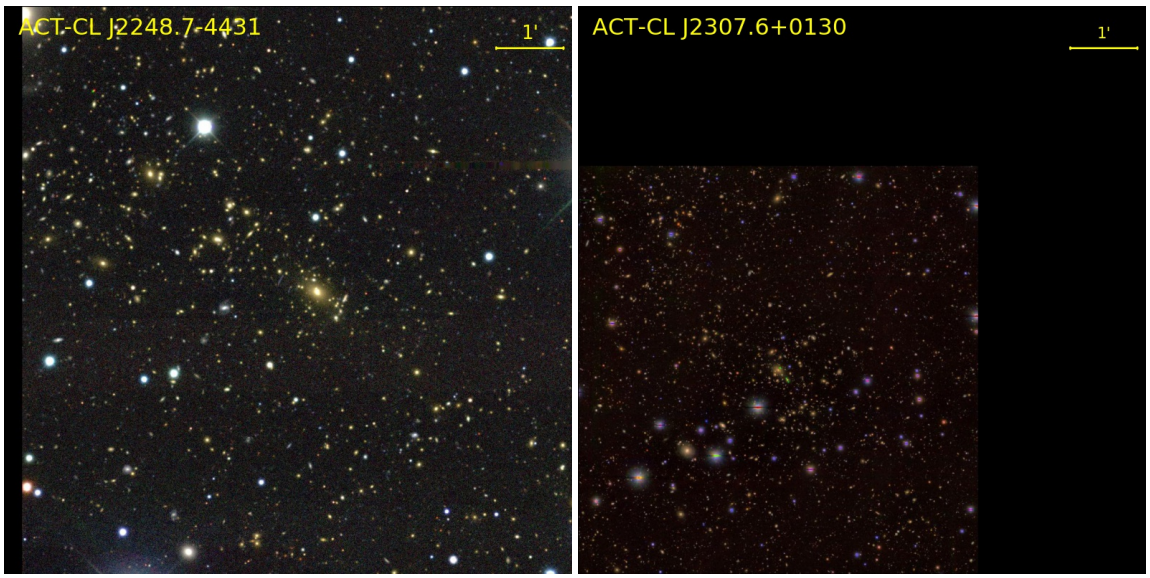
(a) (b)

Figure A.1.35: DES cluster images of (a) ACT-CL J2035.1-5251 and (b) ACT-CL J2116.1-0226.



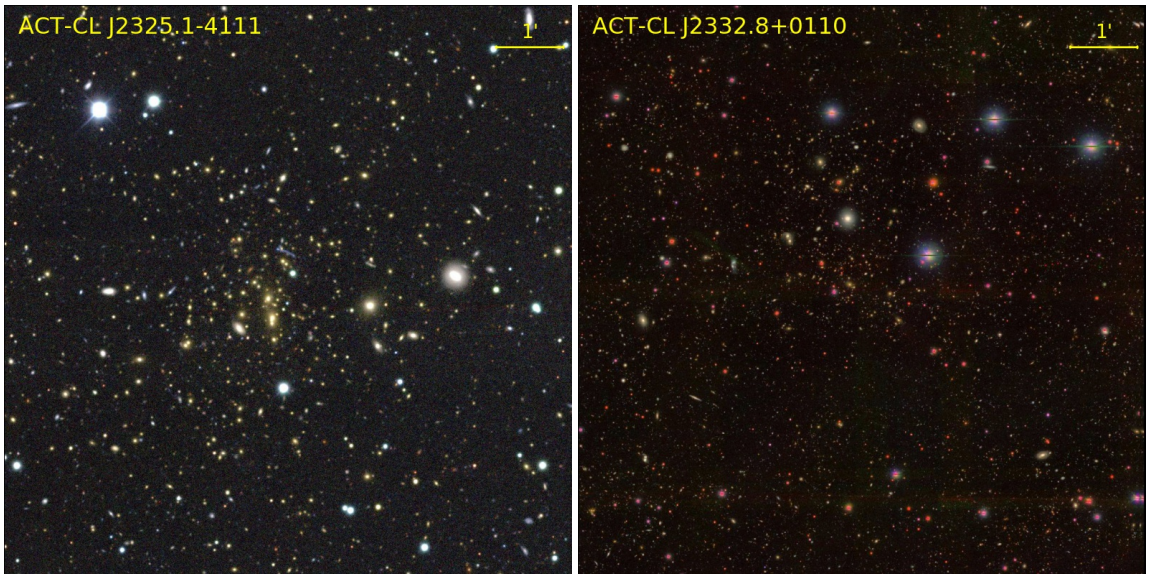
(a) (b)

Figure A.1.36: DES cluster images of (a) ACT-CL J2128.4+0136 and (b) ACT-CL J2233.3-5338.



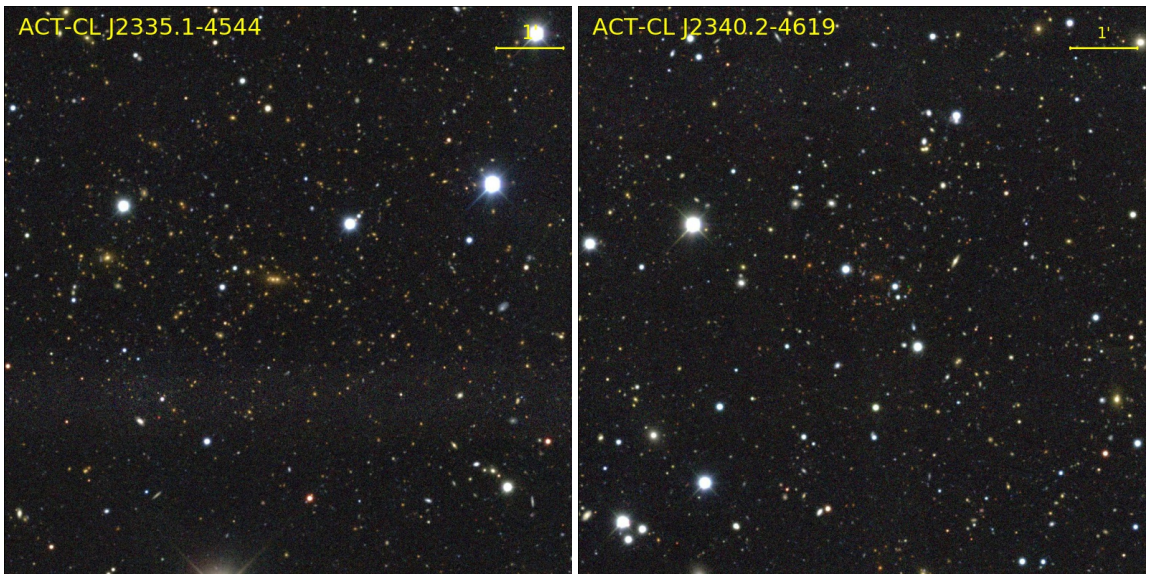
(a) (b)

Figure A.1.37: DES cluster images of (a) ACT-CL J2248.7-4431 and (b) ACT-CL J2307.6+0130.



(a) (b)

Figure A.1.38: DES cluster images of (a) ACT-CL J2325.1-4111 and (b) ACT-CL J2332.8+0110.



(a) (b)

Figure A.1.39: DES cluster images of (a) ACT-CL J2335.1-4544 and (b) ACT-CL J2340.2-4619.

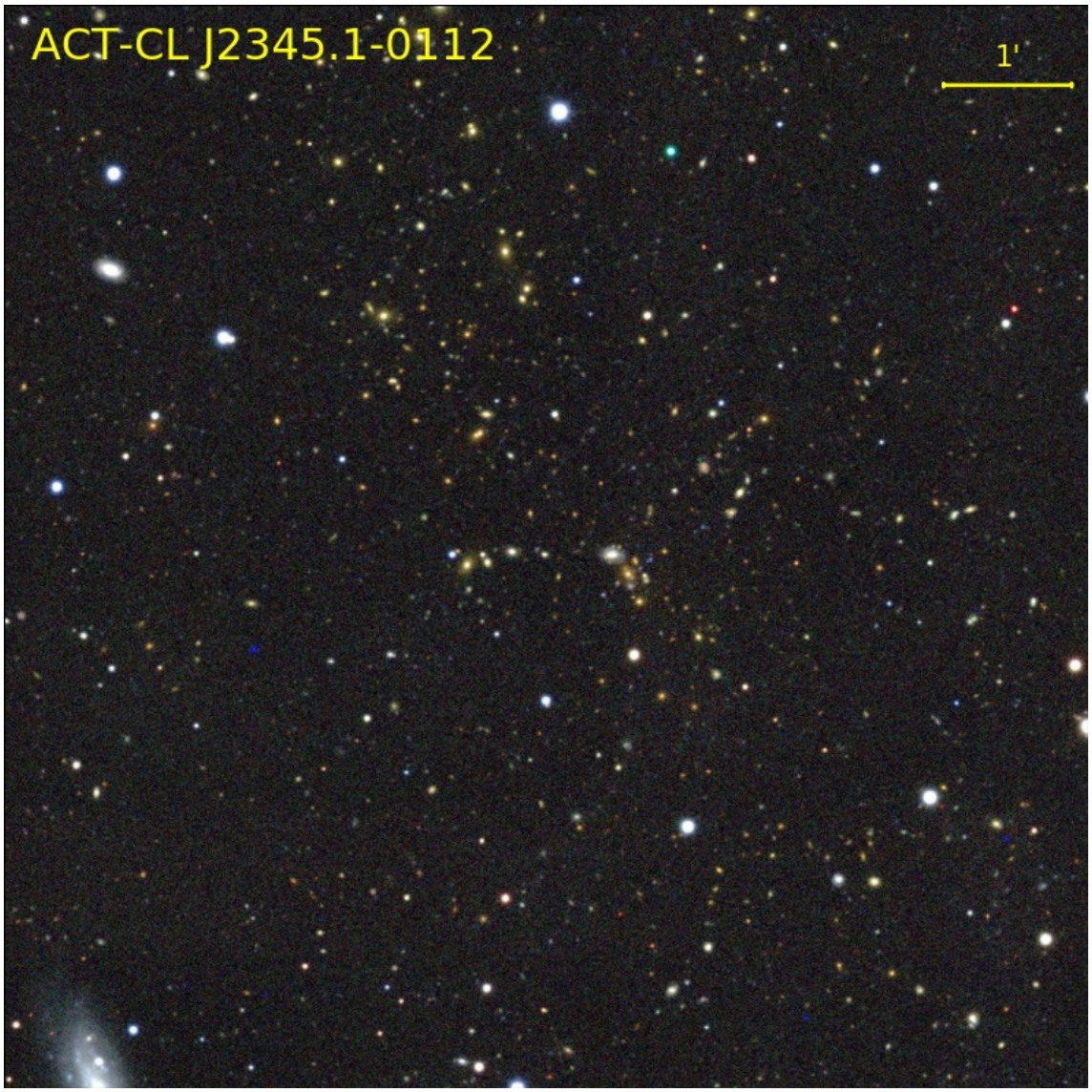


Figure A.1.40: DES cluster image of ACT-CL J2345.1-0112.

Appendix B

Stacking Groups

In this Appendix, we present the stacked BCG group members mentioned in Chapter 3.

B.1 BCG stacking groups

Name	Members (ACT-CL)
Group 01	J0257.7-2209
	J0405.9–4915
	J0014.0+0227
	J0127.2+0020
	J2031.8–4037
	J0040.8–4408
	J2325.1–4111
	J0044.4+0150
	J0008.1+0201
	J0219.9+0130
Group 02	J0405.9–4915
	J0014.0+0227
	J0127.2+0020
	J2031.8–4037
	J0040.8–4408
	J2325.1–4111
	J0044.4+0150
	J0008.1+0201
	J0219.9+0130
	J0028.3+0317

Name	Members (ACT-CL)
Group 03	J0014.0+0227
	J0127.2+0020
	J2031.8–4037
	J0040.8–4408
	J2325.1–4111
	J0044.4+0150
	J0008.1+0201
	J0219.9+0130
	J0028.3+0317
	J0154.5–0039
Group 04	J0127.2+0020
	J2031.8–4037
	J0040.8–4408
	J2325.1–4111
	J0044.4+0150
	J0008.1+0201
	J0219.9+0130
	J0028.3+0317
	J0154.5–0039
	J0024.6+0001

Table B.1: Stacked members of $0.3 \leq z < 0.4$.

Name	Members (ACT-CL)
Group 05	J2031.8–4037
	J0040.8–4408
	J2325.1–4111
	J0044.4+0150
	J0008.1+0201
	J0219.9+0130
	J0028.3+0317
	J0154.5–0039
	J0024.6+0001
	J0239.8–0134
Group 06	J0040.8–4408
	J2325.1–4111
	J0044.4+0150
	J0008.1+0201
	J0219.9+0130
	J0028.3+0317
	J0154.5–0039
	J0024.6+0001
	J0239.8–0134
	J0034.5+0225
Group 07	J2325.1–4111
	J0044.4+0150
	J0008.1+0201
	J0219.9+0130
	J0028.3+0317
	J0154.5–0039
	J0024.6+0001
	J0239.8–0134
	J0034.5+0225
	J0135.8–2044
Group 08	J0044.4+0150
	J0008.1+0201
	J0219.9+0130
	J0028.3+0317
	J0154.5–0039
	J0024.6+0001
	J0239.8–0134
	J0034.5+0225
	J0135.8–2044
	J2307.6+0130

Name	Members (ACT-CL)
Group 09	J0008.1+0201
	J0219.9+0130
	J0028.3+0317
	J0154.5–0039
	J0024.6+0001
	J0239.8–0134
	J0034.5+0225
	J0135.8–2044
	J2307.6+0130
	J0024.0–0444
Group 10	J0219.9+0130
	J0028.3+0317
	J0154.5–0039
	J0024.6+0001
	J0239.8–0134
	J0034.5+0225
	J0135.8–2044
	J2307.6+0130
	J0024.0–0444
	J2128.4+0136
Group 11	J0028.3+0317
	J0154.5–0039
	J0024.6+0001
	J0239.8–0134
	J0034.5+0225
	J0135.8–2044
	J2307.6+0130
	J0024.0–0444
	J2128.4+0136
	J0416.1–2404
Group 12	J0154.5–0039
	J0024.6+0001
	J0239.8–0134
	J0034.5+0225
	J0135.8–2044
	J2307.6+0130
	J0024.0–0444
	J2128.4+0136
	J0416.1–2404
	J0159.8–0849

Table B.2: Table B.1 continued.

Name	Members (ACT-CL)
Group 01	J0013.2–4906
	J0256.5+0006
	J0411.2–4819
	J0159.0–3413
	J0438.3–5419
	J0358.9–2955
	J0125.7–0634
Group 02	J0256.5+0006
	J0411.2–4819
	J0159.0–3413
	J0438.3–5419
	J0358.9–2955
	J0125.7–0634
	J2233.3–5338
Group 03	J0411.2–4819
	J0159.0–3413
	J0438.3–5419
	J0358.9–2955
	J0125.7–0634
	J2233.3–5338
	J0154.4–0321
Group 04	J0159.0–3413
	J0438.3–5419
	J0358.9–2955
	J0125.7–0634
	J2233.3–5338
	J0154.4–0321
	J0140.0–0554
Group 05	J0438.3–5419
	J0358.9–2955
	J0125.7–0634
	J2233.3–5338
	J0154.4–0321
	J0140.0–0554
	J2116.1–0226
Group 06	J0358.9–2955
	J0125.7–0634
	J2233.3–5338
	J0154.4–0321
	J0140.0–0554
	J2116.1–0226
	J0008.5–0519
Group 07	J0256.5+0006
	J0411.2–4819
	J0159.0–3413
	J0438.3–5419
	J0358.9–2955
	J0125.7–0634
	J2233.3–5338
	J0154.4–0321
	J0140.0–0554
	J2116.1–0226
Group 08	J0013.2–4906
	J0256.5+0006
	J0411.2–4819
	J0159.0–3413
	J0438.3–5419
	J0358.9–2955
	J0125.7–0634
	J2233.3–5338
	J0154.4–0321
	J0140.0–0554

Table B.3: Stacked members of $0.4 \leq z < 0.5$.

Name	Members (ACT-CL)
Group 01	J0108.0+0251
	J0014.9–0057
	J2035.1–5251
	J0132.2–0940
	J0025.9–4133
Group 02	J0014.9–0057
	J2035.1–5251
	J0132.2–0940
	J0025.9–4133
	J0006.9–0041
Group 03	J2035.1–5251
	J0132.2–0940
	J0025.9–4133
	J0006.9–0041
	J2335.1–4544
Group 04	J0132.2–0940
	J0025.9–4133
	J0006.9–0041
	J2335.1–4544
	J0031.4–0144
Group 05	J2035.1–5251
	J0132.2–0940
	J0025.9–4133
	J0006.9–0041
	J2335.1–4544
	J0031.4–0144

Name	Members (ACT-CL)
Group 06	J0014.9–0057
	J2035.1–5251
	J0132.2–0940
	J0025.9–4133
	J0006.9–0041
	J2335.1–4544
Group 07	J0108.0+0251
	J0014.9–0057
	J2035.1–5251
	J0132.2–0940
	J0025.9–4133
	J0006.9–0041
Group 08	J0108.0+0251
	J0014.9–0057
	J2035.1–5251
	J0132.2–0940
	J0025.9–4133
	J0006.9–0041
	J2335.1–4544
Group 09	J0108.0+0251
	J0014.9–0057
	J2035.1–5251
	J0132.2–0940
	J0025.9–4133
	J0006.9–0041
	J2335.1–4544
	J0031.4–0144

Table B.4: Stacked members of $0.5 \leq z < 0.6$.

Name	Members (ACT-CL)
Group 01	J0240.0+0115
	J0020.5+0239
	J0446.7–3703
	J0502.9–2902
	J0559.7–5249
	J0352.9–5648
	J0030.8+0102
	J0008.8+0117
	J0106.1–0618
	J0058.0+0031
Group 02	J0020.5+0239
	J0446.7–3703
	J0502.9–2902
	J0559.7–5249
	J0352.9–5648
	J0030.8+0102
	J0008.8+0117
	J0106.1–0618
	J0058.0+0031
	J0026.2+0120
Group 03	J0446.7–3703
	J0502.9–2902
	J0559.7–5249
	J0352.9–5648
	J0030.8+0102
	J0008.8+0117
	J0106.1–0618
	J0058.0+0031
	J0026.2+0120
	J0248.9–0328
Group 04	J0502.9–2902
	J0559.7–5249
	J0352.9–5648
	J0030.8+0102
	J0008.8+0117

Name	Members (ACT-CL)
Group 04	J0106.1–0618
	J0058.0+0031
	J0026.2+0120
	J0248.9–0328
	J0021.5–4902
Group 05	J0559.7–5249
	J0352.9–5648
	J0030.8+0102
	J0008.8+0117
	J0106.1–0618
	J0058.0+0031
	J0026.2+0120
	J0248.9–0328
	J0021.5–4902
	J0022.7–4832
Group 06	J0352.9–5648
	J0030.8+0102
	J0008.8+0117
	J0106.1–0618
	J0058.0+0031
	J0026.2+0120
	J0248.9–0328
	J0021.5–4902
	J0022.7–4832
	J0521.1–5104
Group 07	J0030.8+0102
	J0008.8+0117
	J0106.1–0618
	J0058.0+0031
	J0026.2+0120
	J0248.9–0328
	J0021.5–4902
	J0022.7–4832
	J0521.1–5104
	J0142.1–5032

Table B.5: Stacked members of $0.6 \leq z < 0.7$.

Name	Members (ACT-CL)
Group 08	J0008.8+0117 J0106.1–0618 J0058.0+0031 J0026.2+0120 J0248.9–0328 J0021.5–4902 J0022.7–4832 J0521.1–5104 J0142.1–5032 J0218.2–0041
Group 09	J0106.1–0618 J0058.0+0031 J0026.2+0120 J0248.9–0328 J0021.5–4902 J0022.7–4832 J0521.1–5104 J0142.1–5032 J0218.2–0041 J0359.3–5218

Name	Members (ACT-CL)
Group 10	J0058.0+0031 J0026.2+0120 J0248.9–0328 J0021.5–4902 J0022.7–4832 J0521.1–5104 J0142.1–5032 J0218.2–0041 J0359.3–5218 J0012.4–3346
Group 11	J0026.2+0120 J0248.9–0328 J0021.5–4902 J0022.7–4832 J0521.1–5104 J0142.1–5032 J0218.2–0041 J0359.3–5218 J0012.4–3346 J0213.3+0605

Table B.6: Table B.5 continued.

Name	Members (ACT-CL)
Group 01	J0119.9+0055 J2340.2–4619 J0008.6–3808
Group 02	J2340.2–4619 J0008.6–3808 J0102.5+0341
Group 03	J0008.6–3808 J0102.5+0341 J0027.6–4742
Group 04	J0119.9+0055 J2340.2–4619 J0008.6–3808 J0102.5+0341

Name	Members (ACT-CL)
Group 05	J2340.2–4619 J0008.6–3808 J0102.5+0341 J0027.6–4742
Group 06	J0119.9+0055 J2340.2–4619 J0008.6–3808 J0102.5+0341 J0027.6–4742

Table B.7: Stacked members of $0.7 \leq z < 0.8$.

Bibliography

Abell, G. O. (1958). The distribution of rich clusters of galaxies. *The Astrophysical Journal Supplement Series*, 3, 211.

Abell, G. O. (1965). Clustering of galaxies. *Annual Review of Astronomy and Astrophysics*, 3(1), 1–22.

Andreon, S., Garilli, B., Maccagni, D., Gregorini, L., & Vettolani, G. (1992). Multicolor surface photometry of brightest cluster galaxies. *Astronomy and Astrophysics*, 266, 127–139.

Aragón-Salamanca, A., Ellis, R. S., Couch, W. J., & Carter, D. (1993). Evidence for systematic evolution in the properties of galaxies in distant clusters. *Monthly Notices of the Royal Astronomical Society*, 262(3), 764–794.

Baade, W. (1944). The resolution of messier 32, ngc 205, and the central region of the andromeda nebula. *The Astrophysical Journal*, 100, 137.

Bacon, R., Copin, Y., Monnet, G., Miller, B. W., Allington-Smith, J., Bureau, M., Marcella Carollo, C., Davies, R. L., Emsellem, E., Kuntschner, H., et al. (2001). The sauron project–i. the panoramic integral-field spectrograph. *Monthly Notices of the Royal Astronomical Society*, 326(1), 23–35.

Bahcall, N. A. (1999). Clusters and superclusters of galaxies. *Formation of Structure in the Universe*, 4, 135.

Bastian, N., Covey, K. R., & Meyer, M. R. (2010). A universal stellar initial mass function? a critical look at variations. *Annual Review of Astronomy and Astrophysics*, 48, 339–389.

Beifiori, A., Maraston, C., Thomas, D., & Johansson, J. (2011). On the spectral resolution of the miles stellar library. *Astronomy & Astrophysics*, 531, A109.

Bernardi, M., Hyde, J. B., Sheth, R. K., Miller, C. J., & Nichol, R. C. (2007). The luminosities, sizes, and velocity dispersions of brightest cluster galaxies: implications for formation history. *The Astronomical Journal*, 133(4), 1741.

Biesiadzinski, T., McMahon, J., Miller, C. J., Nord, B., & Shaw, L. (2012). Impact of systematics on sz–optical scaling relations. *The Astrophysical Journal*, 757(1), 1.

Binney, J. & Merrifield, M. (2000). Galactic astronomy.

Blanc, G. A., Weinzirl, T., Song, M., Heiderman, A., Gebhardt, K., Jogee, S., Evans, N. J., van den Bosch, R. C., Luo, R., Drory, N., et al. (2013). The virus-p exploration of nearby galaxies (venga): survey design, data processing, and spectral analysis methods. *The Astronomical Journal*, 145(5), 138.

Bleem, L., Stalder, B., De Haan, T., Aird, K., Allen, S., Applegate, D., Ashby, M. L., Bautz, M., Bayliss, M., Benson, B., et al. (2015). Galaxy clusters discovered via the sunyaev–zel'dovich effect in the 2500-square-degree spt-sz survey. *The Astrophysical Journal Supplement Series*, 216(2), 27.

Bocquet, S., Dietrich, J., Schrabback, T., Bleem, L., Klein, M., Allen, S., Applegate, D., Ashby, M., Bautz, M., Bayliss, M., et al. (2019). Cluster cosmology constraints from the 2500 deg2 spt-sz survey: inclusion of weak gravitational lensing data from magellan and the hubble space telescope. *The Astrophysical Journal*, 878(1), 55.

Böttcher, M., Van Soelen, B., Britto, R. J., Buckley, D. A., Marais, J. P., & Schutte, H. (2017). Salt spectropolarimetry and self-consistent sed and polarization modeling of blazars. *Galaxies*, 5(3), 52.

Bower, R. G., Lucey, J., & Ellis, R. S. (1992). Precision photometry of early-type galaxies in the coma and virgo clusters: a test of the universality of the colour–magnitude relation–i. the data. *Monthly Notices of the Royal Astronomical Society*, 254(4), 589–600.

Bruzual, G. & Charlot, S. (2003). Stellar population synthesis at the resolution of 2003. *Monthly Notices of the Royal Astronomical Society*, 344(4), 1000–1028.

Buckley, D., Swart, G., Meiring, J., & Stepp, L. (2006). Ground-based and airborne telescopes. In *Proc. SPIE*, volume 6267.

Bundy, K., Bershady, M. A., Law, D. R., Yan, R., Drory, N., MacDonald, N., Wake, D. A., Cherinka, B., Sánchez-Gallego, J. R., Weijmans, A.-M., et al. (2014). Overview of the sdss-iv manga survey: mapping nearby galaxies at apache point observatory. *The Astrophysical Journal*, 798(1), 7.

Cannarozzo, C. (2021). *The merger-driven evolution of early-type galaxies and the connection with their dark matter halos.* PhD thesis, Alma Mater Studiorum - Universitá di Bologna.

Cannon, R., Drinkwater, M., Edge, A., Eisenstein, D., Nichol, R., Outram, P., Pimbblet, K., De Propris, R., Roseboom, I., Wake, D., et al. (2006). The 2df-sdss lrg and qso (2slaq) luminous red galaxy survey. *Monthly Notices of the Royal Astronomical Society*, 372(1), 425–442.

Cappellari, M. (2017). Improving the full spectrum fitting method: Accurate convolution with gauss–hermite functions. *MNRAS*, 466(1), 798–811.

Cappellari, M. (2022). Full spectrum fitting with photometry in ppxf: non-parametric star formation history, metallicity and the quenching boundary from 3200 lega-c galaxies at redshift z˜ 0.8. *arXiv preprint arXiv:2208.14974*.

Cappellari, M. & Emsellem, E. (2004). Parametric recovery of line-of-sight velocity distributions from absorption-line spectra of galaxies via penalized likelihood. *Publications of the Astronomical Society of the Pacific*, 116(816), 138.

Cappellari, M., Emsellem, E., Krajnović, D., McDermid, R. M., Serra, P., Alatalo, K., Blitz, L., Bois, M., Bournaud, F., Bureau, M., et al. (2011). The atlas3d project–vii. a new look at the morphology of nearby galaxies: the kinematic morphology–density relation. *Monthly Notices of the Royal Astronomical Society*, 416(3), 1680–1696.

Carson, D. P. & Nichol, R. C. (2010). The age–redshift relation for luminous red galaxies in the sloan digital sky survey. *Monthly Notices of the Royal Astronomical Society*, 408(1), 213–233.

Chabrier, G. (2003). Galactic stellar and substellar initial mass function1. *Publications of the Astronomical Society of the Pacific*, 115(809), 763.

Collister, A., Lahav, O., Blake, C., Cannon, R., Croom, S., Drinkwater, M., Edge, A., Eisenstein, D., Loveday, J., Nichol, R., et al. (2007). Megaz-lrg: a photometric redshift catalogue of one million sdss luminous red galaxies. *Monthly Notices of the Royal Astronomical Society*, 375(1), 68–76.

Comparat, J., Maraston, C., Goddard, D., et al. (2017). Stellar population properties for 2 million galaxies from sdss dr14 and deep2 dr4 from full spectral fitting. *arXiv preprint arXiv:1711.06575*.

Conroy, C. (2013). Modeling the panchromatic spectral energy distributions of galaxies. *Annual Review of Astronomy and Astrophysics*, 51, 393–455.

Conroy, C., Van Dokkum, P. G., & Villaume, A. (2017). The stellar initial mass function in early-type galaxies from absorption line spectroscopy. iv. a super-salpeter imf in the center of ngc 1407 from non-parametric models. *The Astrophysical Journal*, 837(2), 166.

Conroy, C., Wechsler, R. H., & Kravtsov, A. V. (2007). The hierarchical build-up of massive galaxies and the intracluster light since z= 1. *The Astrophysical Journal*, 668(2), 826.

Conselice, C. J., Gallagher III, J. S., & Wyse, R. F. (2001). On the nature of the ngc 1275 system. *The Astronomical Journal*, 122(5), 2281.

Cowie, L. & Binney, J. (1977). Radiative regulation of gas flow within clusters of galaxies-a model for cluster x-ray sources. *The Astrophysical Journal*, 215, 723–732.

Crawford, C., Allen, S., Ebeling, H., Edge, A., & Fabian, A. (1999). The rosat brightest cluster sample—iii. optical spectra of the central cluster galaxies. *Monthly Notices of the Royal Astronomical Society*, 306(4), 857–896.

Crawford, S. M., Still, M., Schellart, P., Balona, L., Buckley, D. A., Dugmore, G., Gulbis, A. A., Kniazev, A., Kotze, M., Loaring, N., et al. (2010). Pysalt: the salt science pipeline. In *Observatory Operations: Strategies, Processes, and Systems III*, volume 7737 (pp. 773725).: International Society for Optics and Photonics.

Croom, S. M., Lawrence, J. S., Bland-Hawthorn, J., Bryant, J. J., Fogarty, L., Richards, S., Goodwin, M., Farrell, T., Miziarski, S., Heald, R., et al. (2012). The sydney-aao multi-object integral field spectrograph. *Monthly Notices of the Royal Astronomical Society*, 421(1), 872–893.

De Lucia, G. & Blaizot, J. (2007). The hierarchical formation of the brightest cluster galaxies. *Monthly Notices of the Royal Astronomical Society*, 375(1), 2–14.

de Zeeuw, T. P., Bureau, M., Emsellem, E., Bacon, R., Marcella Carollo, C., Copin, Y., Davies, R. L., Kuntschner, H., Miller, B. W., Monnet, G., et al. (2002). The sauron project—ii. sample and early results. *Monthly Notices of the Royal Astronomical Society*, 329(3), 513–530.

Dib, S. (2014). Testing the universality of the imf with bayesian statistics: young clusters. *Monthly Notices of the Royal Astronomical Society*, 444(2), 1957–1981.

Donahue, M., Bruch, S., Wang, E., Voit, G. M., Hicks, A. K., Haarsma, D. B., Croston, J. H., Pratt, G. W., Pierini, D., O'Connell, R. W., et al. (2010). Star formation and uv colors of the brightest cluster galaxies in the representative xmm-newton cluster structure survey. *The Astrophysical Journal*, 715(2), 881.

Dressler, A. (1980). Galaxy morphology in rich clusters-implications for the formation and evolution of galaxies. *The Astrophysical Journal*, 236, 351–365.

Dubinski, J. (1998). The origin of the brightest cluster galaxies. *The Astrophysical Journal*, 502(1), 141.

Edwards, L. O., Hudson, M. J., Balogh, M. L., & Smith, R. J. (2007). Line emission in the brightest cluster galaxies of the noao fundamental plane and sloan digital sky surveys. *Monthly Notices of the Royal Astronomical Society*, 379(1), 100–110.

Eggen, O., Lynden-Bell, D., & Sandage, A. (1962). Evidence from the motions of old stars that the galaxy collapsed. *The Astrophysical Journal*, 136, 748.

Emsellem, E., Cappellari, M., Peletier, R. F., McDermid, R. M., Bacon, R., Bureau, M., Copin, Y., Davies, R. L., Krajnović, D., Kuntschner, H., et al. (2004). The sauron project–iii. integral-field absorption-line kinematics of 48 elliptical and lenticular galaxies. *Monthly Notices of the Royal Astronomical Society*, 352(3), 721–743.

Faber, S. (1972). Quadratic programming applied to the problem of galaxy population synthesis. *Astronomy and Astrophysics*, 20, 361–374.

Fabian, A. C. (1994). Cooling flows in clusters of galaxies. *Annual Review of Astronomy and Astrophysics*, 32(1), 277–318.

Ferreras, I., La Barbera, F., & Vazdekis, A. (2016). Is the stellar initial mass function universal? *Astronomy & Geophysics*, 57(2), 2–32.

Gerhard, O. E. (1993). Line-of-sight velocity profiles in spherical galaxies: breaking the degeneracy between anisotropy and mass. *Monthly Notices of the Royal Astronomical Society*, 265(1), 213–230.

Gerssen, J. (2000). *Stellar kinematics in disk galaxies*. PhD thesis, Rijksuniversiteit Groningen.

Gifford, D., Kern, N., & Miller, C. J. (2017). Stacking caustic masses from galaxy clusters. *The Astrophysical Journal*, 834(2), 204.

Goddard, D., Thomas, D., Maraston, C., Westfall, K., Etherington, J., Riffel, R., Mallmann, N. D., Zheng, Z., Argudo-Fernandez, M., Lian, J., et al. (2017). Sdss-iv manga: Spatially resolved star formation histories in galaxies as a function of galaxy mass and type. *MNRAS*, 466(4), 4731–4758.

Green, T. et al. (2017). *A Study of Brightest Cluster Galaxies Over the Last Five Billion Years*. PhD thesis, Durham University.

Groenewald, D. & Loubser, S. (2014). Investigating the star formation histories of the brightest cluster galaxies. *Monthly Notices of the Royal Astronomical Society*, 444(1), 808–826.

Gustafsson, B., Bell, R., Eriksson, K., & Nordlund, Å. (1975). A grid of model atmospheres for metal-deficient giant stars. i. *Astronomy and Astrophysics*, 42, 407–432.

Gustafsson, B., Edvardsson, B., Eriksson, K., Jørgensen, U. G., Nordlund, Å., & Plez, B. (2008). A grid of marcs model atmospheres for late-type stars-i. methods and general properties. *Astronomy & Astrophysics*, 486(3), 951–970.

Gustafsson, B., Edvardsson, B., Eriksson, K., Mizuno-Wiedner, M., Jørgensen, U., Plez, B., Hubeny, I., Mihalas, D., & Werner, K. (2003). Stellar atmosphere modeling. In *ASP Conf. ser*, volume 288 (pp. 331).

Henden, N. A. (2019). *Exploring galaxy clusters and groups with cosmological simulations*. PhD thesis, University of Cambridge.

Henderson, S., Allison, R., Austermann, J., Baildon, T., Battaglia, N., Beall, J., Becker, D., De Bernardis, F., Bond, J., Calabrese, E., et al. (2016). Advanced actpol cryogenic detector arrays and readout. *Journal of Low Temperature Physics*, 184(3), 772–779.

Hilton, M. et al. (2018). The atacama cosmology telescope: the two-season actpol sunyaev–zel'dovich effect selected cluster catalog. *ApJS*, 235(1), 20.

Hilton, M. et al. (2021). The atacama cosmology telescope: A catalog of > 4000 sunyaev-zel'dovich galaxy clusters. *ApJS*, 253(1), 3.

Hoffer, A. S., Donahue, M., Hicks, A., & Barthelemy, R. (2012). Infrared and ultraviolet star formation in brightest cluster galaxies in the accept sample. *The Astrophysical Journal Supplement Series*, 199(1), 23.

Hubble, E. (1929). A relation between distance and radial velocity among extra-galactic nebulae. *Proceedings of the national academy of sciences*, 15(3), 168–173.

Illingworth, G. (1977). Rotation in 13 elliptical galaxies. *The Astrophysical Journal*, 218, L43–L47.

Jordán, A., Côté, P., West, M. J., Marzke, R. O., Minniti, D., & Rejkuba, M. (2004). Hubble space telescope observations of cd galaxies and their globular cluster systems. *The Astronomical Journal*, 127(1), 24.

Kaastra, J., Ferrigno, C., Tamura, T., Paerels, F., Peterson, J., & Mittaz, J. (2001). Xmm-newton observations of the cluster of galaxies sérsic 159-03. *Astronomy & Astrophysics*, 365(1), L99–L103.

Kauffmann, G., White, S. D., & Guiderdoni, B. (1993). The formation and evolution of galaxies within merging dark matter haloes. *Monthly Notices of the Royal Astronomical Society*, 264(1), 201–218.

Kirk, B. et al. (2015). Salt spectroscopic observations of galaxy clusters detected by act and a type ii quasar hosted by a brightest cluster galaxy. *Monthly Notices of the Royal Astronomical Society*, 449(4), 4010–4026.

Koleva, M., Prugniel, P., Bouchard, A., & Wu, Y. (2009). Ulyss: a full spectrum fitting package. *Astronomy & Astrophysics*, 501(3), 1269–1279.

Koleva, M., Prugniel, P., Ocvirk, P., Le Borgne, D., & Soubiran, C. (2008). Spectroscopic ages and metallicities of stellar populations: validation of full spectrum fitting. *Monthly Notices of the Royal Astronomical Society*, 385(4), 1998–2010.

Kroupa, P. (2001). On the variation of the initial mass function. *Monthly Notices of the Royal Astronomical Society*, 322(2), 231–246.

Kuijken, K. & Merrifield, M. R. (1993). A new method for obtaining stellar velocity distributions from absorption-line spectra: unresolved gaussian decomposition. *Monthly Notices of the Royal Astronomical Society*, 264(3), 712–720.

Larson, R. B. (2006). Understanding the stellar initial mass function. In *Revista mexicana de astronomia y astrofisica conference series*, volume 26 (pp. 55–59).

Lauer, T. R., Gebhardt, K., Faber, S., Richstone, D., Tremaine, S., Kormendy, J., Aller, M., Bender, R., Dressler, A., Filippenko, A. V., et al. (2007). The centers of early-type galaxies with hubble space telescope. vi. bimodal central surface brightness profiles. *The Astrophysical Journal*, 664(1), 226.

Lauer, T. R., Postman, M., Strauss, M. A., Graves, G. J., & Chisari, N. E. (2014). Brightest cluster galaxies at the present epoch. *The Astrophysical Journal*, 797(2), 82.

Le Borgne, J.-F., Bruzual, G., Pelló, R., Lançon, A., Rocca-Volmerange, B., Sanahuja, B., Schaerer, D., Soubiran, C., & Vílchez-Gómez, R. (2003). Stelib: A library of stellar spectra at. *Astronomy & Astrophysics*, 402(2), 433–442.

Leveque, A. (2017). *Evolution of galaxies in clusters.* PhD thesis, Università degli Studi di Napoli Federico II.

Lidman, C., Suherli, J., Muzzin, A., Wilson, G., Demarco, R., Brough, S., Rettura, A., Cox, J., DeGroot, A., Yee, H., et al. (2012). Evidence for significant growth in the stellar mass of brightest cluster galaxies over the past 10 billion years. *Monthly Notices of the Royal Astronomical Society*, 427(1), 550–568.

Lin, Y.-T., Mohr, J. J., & Stanford, S. A. (2003). Near-infrared properties of galaxy clusters: luminosity as a binding mass predictor and the state of cluster baryons. *The Astrophysical Journal*, 591(2), 749.

Liu, F., Mao, S., Deng, Z., Xia, X., & Wen, Z. (2009). Major dry mergers in early-type brightest cluster galaxies. *Monthly Notices of the Royal Astronomical Society*, 396(4), 2003–2010.

Loubser, S. (2009). *Kinematics and stellar populations in brightest cluster galaxies.* PhD thesis, University of Central Lancashire.

Loubser, S., Babul, A., Hoekstra, H., Bahé, Y., O'Sullivan, E., & Donahue, M. (2020). Dynamical masses of brightest cluster galaxies i: stellar velocity anisotropy and mass-to-light ratios. *MNRAS*, 496(2), 1857–1880.

Loubser, S., Babul, A., Hoekstra, H., Mahdavi, A., Donahue, M., Bildfell, C., & Voit, G. (2016). The regulation of star formation in cool-core clusters: imprints on the stellar populations of brightest cluster galaxies. *MNRAS*, 456(2), 1565–1578.

Loubser, S., Hoekstra, H., Babul, A., Bahé, Y., & Donahue, M. (2021). Dynamical masses of brightest cluster galaxies–ii. constraints on the stellar imf. *Monthly Notices of the Royal Astronomical Society*, 500(3), 4153–4165.

Maples, M., Reichart, D., Konz, N., Berger, T., Trotter, A., Martin, J., Dutton, D., Paggen, M., Joyner, R., & Salemi, C. (2018). Robust chauvenet outlier rejection. *The Astrophysical Journal Supplement Series*, 238(1), 2.

Maraston, C. (1998). Evolutionary synthesis of stellar populations: a modular tool. *Monthly Notices of the Royal Astronomical Society*, 300(3), 872–892.

Maraston, C., Hill, L., Thomas, D., Yan, R., Chen, Y., Lian, J., Parikh, T., Neumann, J., Meneses-Goytia, S., Bershady, M., et al. (2020). Stellar population models based on the sdss-iv mastar library of stellar spectra–i. intermediate-age/old models. *MNRAS*, 496(3), 2962–2997.

Maraston, C. & Strömbäck, G. (2011). Stellar population models at high spectral resolution. *MNRAS*, 418(4), 2785–2811.

McDonald, M., Benson, B., Veilleux, S., Bautz, M. W., & Reichardt, C. L. (2013). An hst/wfc3-uvis view of the starburst in the cool core of the phoenix cluster. *The Astrophysical Journal Letters*, 765(2), L37.

McDonald, M., Roediger, J., Veilleux, S., & Ehlert, S. (2014). Hst-cos spectroscopy of the cooling flow in a1795—evidence for inefficient star formation in condensing intracluster gas. *The Astrophysical Journal Letters*, 791(2), L30.

McDonald, M., Stalder, B., Bayliss, M., Allen, S., Applegate, D., Ashby, M., Bautz, M., Benson, B., Bleem, L., Brodwin, M., et al. (2016). Star-forming brightest cluster galaxies at 0.25¡ z¡ 1.25: a transitioning fuel supply. *The Astrophysical Journal*, 817(2), 86.

McDonald, M. & Veilleux, S. (2009). Mmtf-hα and hst-fuv imaging of the filamentary complex in abell 1795. *The Astrophysical Journal*, 703(2), L172.

McNamara, B., Rafferty, D., Bîrzan, L., Steiner, J., Wise, M., Nulsen, P. J., Carilli, C., Ryan, R., & Sharma, M. (2006). The starburst in the abell 1835 cluster central galaxy: a case study of galaxy formation regulated by an outburst from a supermassive black hole. *The Astrophysical Journal*, 648(1), 164.

McNamara, B. R. & O'Connell, R. W. (1989). Star formation in cooling flows in clusters of galaxies. *The Astronomical Journal*, 98, 2018–2043.

McNamara, B. R. & O'Connell, R. W. (1992). Color gradients in cooling flows in clusters of galaxies. *The Astrophysical Journal*, 393, 579–610.

McNamara, B. R., Wise, M., Sarazin, C. L., Jannuzi, B. T., & Elston, R. (1996). Optical structure in the abell 1795 cluster central galaxy: Evidence for stripping and deflection of radio jets. *The Astrophysical Journal*, 466(1), L9.

Merritt, D. (1983). Relaxation and tidal stripping in rich clusters of galaxies. i. evolution of the mass distribution. *The Astrophysical Journal*, 264, 24–48.

Merritt, D. (1984). Relaxation and tidal stripping in rich clusters of galaxies. ii. evolution of the luminosity distribution. *The Astrophysical Journal*, 276, 26–37.

Merritt, D. (1985). Relaxation and tidal stripping in rich clusters of galaxies. iii-growth of a massive central galaxy. *The astrophysical journal*, 289, 18–32.

Minkowski, R. (1962). Internal Dispersion of Velocities in Other Galaxies. In G. C. McVittie (Ed.), *Problems of Extra-Galactic Research, Proceedings from IAU Symposium no. 15* (pp. 112).

Mittal, R., McDonald, M., Whelan, J. T., & Bruzual, G. (2016). The challenging task of determining star formation rates: the case of a massive stellar burst in the brightest cluster galaxy of phoenix galaxy cluster. *Monthly Notices of the Royal Astronomical Society*, 465(3), 3143–3153.

Mo, H., Van den Bosch, F., & White, S. (2010). *Galaxy formation and evolution*. Cambridge University Press.

Morgan, W. & Lesh, J. R. (1965). The supergiant galaxies. *The Astrophysical Journal*, 142, 1364.

Myers, A. T., Krumholz, M. R., Klein, R. I., & McKee, C. F. (2011). Metallicity and the universality of the imf. *arXiv preprint arXiv:1102.2023*.

Ocvirk, P., Pichon, C., Lançon, A., & Thiébaut, E. (2006). Stecmap: Stellar content from high-resolution galactic spectra via maximum a posteriori. *Monthly Notices of the Royal Astronomical Society*, 365(1), 46–73.

Ostriker, J. & Hausman, M. (1977). Cannibalism among the galaxies-dynamically produced evolution of cluster luminosity functions. *The Astrophysical Journal*, 217, L125–L129.

Ostriker, J. & Tremaine, S. (1975). Another evolutionary correction to the luminosity of giant galaxies. *The Astrophysical Journal*, 202, L113–L117.

O'Dea, C. P., Baum, S. A., Mack, J., Koekemoer, A. M., & Laor, A. (2004). Hubble space telescope stis far-ultraviolet observations of the central nebulae in the cooling-core clusters a1795 and a2597. *The Astrophysical Journal*, 612(1), 131.

Peebles, P. (1982). Large scale background temperature and mass fluctuations due to scale invariant primeval perturbations.

Penzias, A. A. & Wilson, R. W. (1965). A measurement of excess antenna temperature at 4080 mc/s. *The Astrophysical Journal*, 142, 419–421.

Perez, S. J. A., Nichol, B., Percival, W., Thomas, D. B., Collaboration, D., et al. (2018). The dark energy survey: Data release 1. *Astrophysical Journal, Supplement Series*, 239(2), 18.

Peterson, R. C., Terndrup, D. M., Sadler, E. M., & Walker, A. R. (2001). Hot horizontal-branch stars in the galactic bulge. i. *The Astrophysical Journal*, 547(1), 240.

Prichard, L. J. (2018). *The evolution of early-type galaxies*. PhD thesis, University of Oxford.

Prugniel, P. & Soubiran, C. (2001). A database of high and medium-resolution stellar spectra. *Astronomy & Astrophysics*, 369(3), 1048–1057.

Prugniel, P., Soubiran, C., Koleva, M., & Le Borgne, D. (2007). Vizier online data catalog: Elodie library v3. 1 (prugniel+ 2007). *VizieR Online Data Catalog*, (pp. III–251).

Ratsimbazafy, A., Loubser, S., Crawford, S., Cress, C., Bassett, B., Nichol, R., & Väisänen, P. (2017). Age-dating luminous red galaxies observed with the southern african large telescope. *Monthly Notices of the Royal Astronomical Society*, 467(3), 3239–3254.

Rix, H.-W. & White, S. D. (1992). Optimal estimates of line-of-sight velocity distributions from absorption line spectra of galaxies: nuclear discs in elliptical galaxies. *Monthly Notices of the Royal Astronomical Society*, 254(3), 389–403.

Rodríguez Del Pino, B. (2015). *The influence of environment on the star formation properties of galaxies*. PhD thesis, University of Nottingham.

Rood, H. J. (1965). The dynamics of the coma cluster of galaxies. *Ph. D. Thesis*.

Rubin, V. C., Ford Jr, W. K., & Thonnard, N. (1980). Rotational properties of 21 sc galaxies with a large range of luminosities and radii, from ngc 4605/r= 4kpc/to ugc 2885/r= 122 kpc. *The Astrophysical Journal*, 238, 471–487.

Ruszkowski, M. & Springel, V. (2009). The role of dry mergers for the formation and evolution of brightest cluster galaxies. *The Astrophysical Journal*, 696(2), 1094.

Rykoff, E., Rozo, E., Hollowood, D., Bermeo-Hernandez, A., Jeltema, T., Mayers, J., Romer, A. K., Rooney, P., Saro, A., Cervantes, C. V., et al. (2016). The redmapper galaxy cluster catalog from des science verification data. *The Astrophysical Journal Supplement Series*, 224(1), 1.

Salaris, M. & Cassisi, S. (2005). *Evolution of stars and stellar populations*. John Wiley & Sons.

Salome, P. & Combes, F. (2003). Cold molecular gas in cooling flow clusters of galaxies. *Astronomy & Astrophysics*, 412(3), 657–667.

Salpeter, E. E. (1955). The luminosity function and stellar evolution. *The Astrophysical Journal*, 121, 161.

Sánchez, S., Kennicutt, R., De Paz, A. G., Van de Ven, G., Vílchez, J., Wisotzki, L., Walcher, C., Mast, D., Aguerri, J., Albiol-Pérez, S., et al. (2012). Califa, the calar alto legacy integral field area survey-i. survey presentation. *Astronomy & Astrophysics*, 538, A8.

Sánchez-Blázquez, P., Peletier, R., Jiménez-Vicente, J., Cardiel, N., Cenarro, A. J., Falcon-Barroso, J., Gorgas, J., Selam, S., & Vazdekis, A. (2006). Medium-resolution isaac newton telescope library of empirical spectra. *Monthly Notices of the Royal Astronomical Society*, 371(2), 703–718.

Sanderson, A. J., Ponman, T., Finoguenov, A., Lloyd-Davies, E., & Markevitch, M. (2003). The birmingham—cfa cluster scaling project—i. gas fraction and the m—tx relation. *Monthly Notices of the Royal Astronomical Society*, 340(3), 989–1010.

Sarazin, C. & Boller, T. (1989). Book-review-x-ray emission from clusters of galaxies. *Astronomische Nachrichten*, 310, 362.

Sargent, W. L., Schechter, P. L., Boksenberg, A., & Shortridge, K. (1977). Velocity dispersions for 13 galaxies. *The Astrophysical Journal*, 212, 326–334.

Scalo, J. M. (1986). The stellar initial mass function. *Fundamentals of cosmic physics*, 11, 1–278.

Sifon, C., Battaglia, N., Hasselfield, M., Menanteau, F., Barrientos, L. F., Bond, J. R., Crichton, D., Devlin, M. J., Dünner, R., Hilton, M., et al. (2016). The atacama cosmology telescope: dynamical masses for 44 sz-selected galaxy clusters over 755 square degrees. *Monthly Notices of the Royal Astronomical Society*, 461(1), 248–270.

Simkin, S. (1974). Measurements of velocity dispersions and doppler shifts from digitized optical spectra. *Astronomy and Astrophysics*, 31, 129.

Slipher, V. M. (1913). The radial velocity of the andromeda nebula. *Lowell Observatory Bulletin*, 2, 56–57.

Stott, J. P., Hickox, R. C., Edge, A. C., Collins, C. A., Hilton, M., Harrison, C. D., Romer, A. K., Rooney, P. J., Kay, S. T., Miller, C. J., et al. (2012). The xmm cluster survey: the interplay between the brightest cluster galaxy and the intracluster medium via agn feedback. *Monthly Notices of the Royal Astronomical Society*, 422(3), 2213–2229.

Sunyaev, R. & Zeldovich, Y. B. (1970). The spectrum of primordial radiation, its distortions and their significance. *Comments on Astrophysics and Space Physics*, 2, 66.

Sunyaev, R. & Zeldovich, Y. B. (1972). The observations of relic radiation as a test of the nature of x-ray radiation from the clusters of galaxies. *Comments on Astrophysics and Space Physics*, 4, 173.

Tamura, T., Kaastra, J., Peterson, J., Paerels, F., Mittaz, J., Trudolyubov, S., Stewart, G., Fabian, A., Mushotzky, R., Lumb, D., et al. (2001). X-ray spectroscopy of the cluster of galaxies abell 1795 with xmm-newton. *Astronomy & Astrophysics*, 365(1), L87–L92.

Thomas, R. (2019). Specstack: A simple spectral stacking tool. *Astrophysics Source Code Library*, (pp. ascl–1904).

Tonini, C., Bernyk, M., Croton, D., Maraston, C., & Thomas, D. (2012). The evolution of brightest cluster galaxies in a hierarchical universe. *The Astrophysical Journal*, 759(1), 43.

Tremaine, S. (1990). The origin of central cluster galaxies. In R. Wielen (Ed.), *Dynamics and Interaction of Galaxies* (pp. 394).

Tremblay, G., O'Dea, C., Baum, S., Clarke, T., Sarazin, C., Bregman, J., Combes, F., Donahue, M., Edge, A., Fabian, A., et al. (2012). Residual cooling and persistent star formation amid active galactic nucleus feedback in abell 2597. *Monthly Notices of the Royal Astronomical Society*, 424(2), 1042–1060.

Tremblay, G. R., O'Dea, C. P., Baum, S. A., Mittal, R., McDonald, M., Combes, F., Li, Y., McNamara, B., Bremer, M. N., Clarke, T. E., et al. (2015). Far-ultraviolet morphology of star-forming filaments in cool core brightest cluster galaxies. *Monthly Notices of the Royal Astronomical Society*, 451(4), 3768–3800.

Van der Hulst, J., Terlouw, J., Begeman, K., Zwitser, W., & Roelfsema, P. (1992). The groningen image processing system, gipsy. In *Astronomical Data Analysis Software and Systems I*, volume 25 (pp. 131).

Van Der Marel, R. P. & Franx, M. (1993). A new method for the identification of non-gaussian line profiles in elliptical galaxies. *The Astrophysical Journal*, 407, 525–539.

Varidel, M. R. (2021). *Analysing Gas Kinematics in Star-Forming Galaxies using Disc Modelling*. PhD thesis, University of Sydney.

Vazdekis, A. et al. (2010). Evolutionary stellar population synthesis with miles–i. the base models and a new line index system. *MNRAS*, 404(4), 1639–1671.

Vázquez, J. A., Padilla, L. E., & Matos, T. (2018). Inflationary cosmology: from theory to observations. *arXiv preprint arXiv:1810.09934*.

Vikhlinin, A., Kravtsov, A., Forman, W., Jones, C., Markevitch, M., Murray, S., & Van Speybroeck, L. (2006). Chandra sample of nearby relaxed galaxy clusters: Mass, gas fraction, and mass-temperature relation. *The Astrophysical Journal*, 640(2), 691.

Viljoen, D. N. (2012). *The central stellar populations of brightest cluster galaxies*. PhD thesis, North-West University.

Von Der Linden, A., Best, P. N., Kauffmann, G., & White, S. D. (2007). How special are brightest group and cluster galaxies? *Monthly Notices of the Royal Astronomical Society*, 379(3), 867–893.

Webb, T., Noble, A., DeGroot, A., Wilson, G., Muzzin, A., Bonaventura, N., Cooper, M., Delahaye, A., Foltz, R., Lidman, C., et al. (2015a). An extreme starburst in the core of a rich galaxy cluster at z= 1.7. *The Astrophysical Journal*, 809(2), 173.

Webb, T. M., Lowenthal, J., Yun, M., Noble, A. G., Muzzin, A., Wilson, G., Yee, H., Cybulski, R., Aretxaga, I., & Hughes, D. (2017). Detection of a substantial molecular gas reservoir in a brightest cluster galaxy at z= 1.7. *The Astrophysical Journal Letters*, 844(2), L17.

Webb, T. M., Muzzin, A., Noble, A., Bonaventura, N., Geach, J., Hezevah, Y., Lidman, C., Wilson, G., Yee, H., Surace, J., et al. (2015b). The star formation history of bcgs to z= 1.8 from the sparcs/swire survey: evidence for significant in situ star formation at high redshift. *The Astrophysical Journal*, 814(2), 96.

White, S. D. (1976). Dynamical friction in spherical clusters. *Monthly Notices of the Royal Astronomical Society*, 174(1), 19–28.

Wilkinson, D. M. et al. (2017). Firefly (fitting iteratively for likelihood analysis): a full spectral fitting code. *MNRAS*, 472(4), 4297–4326.

Wilson, S. (2012). *A multi-wavelength study of a sample of galaxy clusters*. PhD thesis, North-West University.

Worthey, G. (1994). Comprehensive stellar population models and the disentanglement of age and metallicity effects. *The Astrophysical Journal Supplement Series*, 95, 107–149.

Worthey, G., Trager, S., & Faber, S. (1995). The galaxian age-metallicity relation. In *Fresh Views of Elliptical Galaxies*, volume 86 (pp. 203).

Yan, R., Chen, Y., Lazarz, D., Bizyaev, D., Maraston, C., Stringfellow, G. S., McCarthy, K., Meneses-Goytia, S., Law, D. R., Thomas, D., et al. (2019). Sdss-iv mastar: A large and comprehensive empirical stellar spectral library—first release. *The Astrophysical Journal*, 883(2), 175.

Zhao, D. (2016). *Evolution of the brightest cluster galaxies*. PhD thesis, University of Nottingham.

Zwicky, F. (1933). The redshift of extragalactic nebulae. *Helvetica physica acta*, 6, 110–127.

Zwicky, F., Herzog, E., Wild, P., Karpowicz, M., & Kowal, C. (1961). Catalogue of galaxies and of clusters of galaxies, vol. i. *Pasadena: California Institute of Technology (CIT*.